THE UNIVERSITY OF QUEENSLAND

AUSTRALIA

Mesoscopic quantum sensors

Bixuan Fan

M.S. (Physics), East China Normal University

A thesis submitted for the degree of Doctor of Philosophy at

The University of Queensland in 2014

School of Mathematics and Physics

Abstract

Detecting an itinerant microwave photon with high efficiency is an outstanding problem in quantum optics at microwave frequencies and in the fundamental quantum mechanics experimental toolbox. This subject has attracted a lot of attention and there are growing number of excellent experimental demonstrations and theoretical proposals towards this aim. However, due to the extremely low energy of microwave quanta, efficiently detecting a propagating microwave photon in a non-absorbing manner is still an unresolved challenge and it is the focus of the major part of this thesis.

Motivated by a recent experiment that shows a superconducting artificial atom (a transmon) in a one-dimensional microwave transmission line exhibits gigantic cross-Kerr nonlinearities, 1000 times larger than in comparable optical systems, I investigate the possibility of detection single microwave photons using a transmon induced cross-Kerr-like interaction between two microwave fields. The photon number in one field is inferred through the measurement of the displacement of the other field. The first project on this subject is to investigate the feasibility of detecting a single microwave photon with signal-to-noise ratio (SNR) greater than unity using a three-level approximation for the transmon in an open transmission line, due to the saturation of transmon response to the probe intensity.

After that, an improved scheme was proposed to overcome the limitations in the preceding work. By using a cavity probe field the signal photon induced probe displacement is strongly enhanced. Further additional transmon-cavity units can be cascaded to further improve the detection efficiency. It is shown that with only two transmons the distinguishability to resolve a single-photon state from the vacuum is up to 90%. One advantage of this photon detection scheme is that it does not rely on the absorption of single microwave photons, which enables repeated measurements and further applications. Moreover, I also show how the measurement diminishes coherence in the photon number basis thereby illustrating a fundamental principle of quantum measurement: the higher the measurement efficiency, the greater is the decoherence.

Apart from the investigation on the single microwave photon detection, this thesis also studies nonlinear dynamics of a hybrid coupled-resonator and opto-mechanical system. It is

shown that the saddle-node bifurcation and the Hopf bifurcation appear in the system, which leads to bistability and limit cycle dynamics of the mechanical position and the output light intensity. More importantly, the opto-mechanical nonlinearity dramatically changes the transparency window of the coupled resonator induced transparency (CRIT) and based on the narrow and bistable CRIT transparency window, the proposed system is shown to be a good platform for the weak impulsive force detection with a good sensitivity.

Declaration by Author

This thesis is composed of my original work, and contains no material previously published or written by another person except where due reference has been made in the text. I have clearly stated the contribution by others to jointly-authored works that I have included in my thesis.

I have clearly stated the contribution of others to my thesis as a whole, including statistical assistance, survey design, data analysis, significant technical procedures, professional editorial advice, and any other original research work used or reported in my thesis. The content of my thesis is the result of work I have carried out since the commencement of my research higher degree candidature and does not include a substantial part of work that has been submitted to qualify for the award of any other degree or diploma in any university or other tertiary institution. I have clearly stated which parts of my thesis, if any, have been submitted to qualify for another award.

I acknowledge that an electronic copy of my thesis must be lodged with the University Library and, subject to the General Award Rules of The University of Queensland, immediately made available for research and study in accordance with the Copyright Act 1968.

I acknowledge that copyright of all material contained in my thesis resides with the copyright holder(s) of that material. Where appropriate I have obtained copyright permission from the copyright holder to reproduce material in this thesis.

Publications during candidature

Bixuan Fan, Anton F. Kockum, Joshua Combes, Göan Johansson, Io-chun Hoi, C. M. Wilson, Per Delsing, G. J. Milburn, and Thomas M. Stace, *Breakdown of the Cross-Kerr Scheme for Photon counting*, Physical Review Letters **110**, 053601 (2013).

Bixuan Fan, Göran Johansson, Joshua Combes, G. J. Milburn, and Thomas M. Stace, *Non-absorbing high-efficiency counter for itinerant microwave photons*, Physical Review B **90**, 035132 (2014).

Zhenglu Duan and **Bixuan Fan**, *Coherently slowing light with a coupled optomechanical crystal array*, Europhysics Letters **99**, 44005 (2013).

Io-Chun Hoi, Anton F. Kockum, Tauno Palomaki, Thomas M. Stace, **Bixuan Fan**, Lars Tornberg, Sankar R. Sathyamoorthy, Göran Johansson, Per Delsing and C. M. Wilson, *Giant Cross-Kerr Effect for Propagating Microwaves Induced by an Artificial Atom Io*, Physical Review Letters **111**, 053601 (2013).

Publications included in this thesis

Bixuan Fan, Anton F. Kockum, Joshua Combes, Göan Johansson, Io-chun Hoi, C. M. Wilson, Per Delsing, G. J. Milburn, and Thomas M. Stace, *Breakdown of the Cross-Kerr Scheme for Photon counting*, Physical Review Letters **110**, 053601 (2013), modified and incorporated as Chapter 3.

Contributor	Statement of contribution
Bixuan Fan (Candidate)	Algorithm (90%) Analytical calculation (80%) Data analysis (80%) Data interpretation (45%) Wrote the paper (70%) Edited the paper (40%)
Anton F. Kockum (Collaborator)	Algorithm (10%) Data analysis (5%) Data interpretation (5%) Edited the paper (5%)
Joshua Combes (Collaborator)	Analytical calculation (20%) Data interpretation (5%) Edited the paper (5%)
Göan Johansson (Collaborator)	Project proposal 10% Data interpretation (5%)
Io-chun Hoi (Collaborator)	Data interpretation (5%)
C. M. Wilson (Collaborator)	Project proposal 10%
Per Delsing (Collaborator)	Project proposal 5%
G. J. Milburn (Supervisor)	Project proposal (15%) Data analysis (10%) Data Interpretation (15%) Wrote the paper (10%) Edited the paper (25%)
Thomas M. Stace (Supervisor)	Project proposal 60% Data analysis (5%) Data interpretation (20%) Wrote the paper (20%) Edited the paper (25%)

Bixuan Fan, Göran Johansson, Joshua Combes, G. J. Milburn, and Thomas M. Stace, *Non-absorbing high-efficiency counter for itinerant microwave photons*, Physical Review B **90**, 035132 (2014), modified and incorporated as Chapter 4.

Contributor	Statement of contribution
Bixuan Fan (Candidate)	Algorithm (100%) Project proposal (30%) Numerical data collection (100%) Numerical data Analysis (70%) Data interpretation (40%) Wrote the paper (70%) Edited the paper (40%)
Göran Johansson (Collaborator)	Project proposal (5%) Data interpretation (10%)
Joshua Combes (Collaborator)	Project proposal (5%) Data interpretation (10%)
G. J. Milburn (Supervisor)	Project proposal (40%) Data interpretation (10%) Wrote the paper (10%) Edited the paper (20%)
Thomas M. Stace (Supervisor)	Project proposal (20%) Numerical data Analysis (30%) Data interpretation (30%) Wrote the paper (20%) Edited the paper (40%)

Contributions by others to the thesis

In Chapter 5, we discuss nonlinear dynamics of a hybrid coupled-resonator and opto-mechanical system and its application to weak impulsive force detection. The initial idea of the project was put forward by Dr Zhenglu Duan and developed by Dr C. A. Holmes, Prof. Gerard Milburn, Dr Tom stace and me. The analytical and numerical calculations were performed by me and the result analysis was done by Zhenglu Duan and me.

Statement of parts of the thesis submitted to qualify for the award of another degree

None

Acknowledgements

I wish to express primary thanks to my supervisors Dr Tom Stace and Prof. Gerard Milburn, without whom I could not finish my PhD research and this thesis. I feel very fortunate and pride to be their student. I really appreciate my principle supervisor Tom for many things. Since the first day I came to UQ and he introduced the first project on superconducting circuits to me, his patient guidance and insightful advice have been with me throughout my PhD time. His enthusiasm and sharp intuition to physics often impressed me and encouraged me, preventing me from losing confidence when I met difficulties in research. I can say that his help was in every step of my improvements. I am also very grateful to my associate supervisor Gerard, who gave me an opportunity to work in such a wonderful research group. I thank him very much for all beautiful explanations to my questions using his vast knowledge and stimulating meetings on many topics. His optimistic attitude towards research makes me believe that in science there is always a way towards the true answer as long as one does not give up. I also thank him for closely following my research despite his extremely busy schedule.

It has been great pleasure to work with a number of amazing people during my PhD. I thank Dr Cathy Holmes, who showed me the beauty of nonlinear dynamics and how to characterize a dynamical system and Dr Josh Combes for his explanations on Fock-state master equation and analytical calculation of the model in my first PhD project. I thank Dr Arkady Fedorov, Matt Wooley, Charles Meaney and Adil Gangat for their helpful and interesting discussions and my collaborators Zhenglu Duan, Anton F. Kockum, Göan Johansson, Io-chun Hoi, C. M. Wilson and Per Delsing for their invaluable contributions to my research. Thanks also to the lecturers of courses I attended: Andrew Doherty, Ben Powell and Tom. I really enjoyed their wonderful lectures and learned a lot from them.

I want to specially thank my dear officemates and good friends Janani, Sahar, Xiaoli and Phien for their sincere friendship, caring and encouragement throughout my PhD. I also enjoyed the great time with other people at physics department: Katya, Uzma, Changqiu, Casey, Andrew Bolt, Juan, Martin, Yarema, Drew, Cyril, Glen Harris, Devin, Kai Liu, Daiqin, Michael Vanner and Matthew Broome and many others.

I also thank Murray Kane, Emma Linnell, Ruth Forest and Eric Pham for their administrative support and their friendship.

Additionally, I want to thank my master thesis's supervisors Prof. Weiping Zhang and Prof. Z. Y. Ou for introducing me to the world of quantum physics and their cautious guidance, which lay the basis for my PhD study and future research.

Most importantly, I am grateful to my family for their sacrifices and supporting my curiosity and pursuit in physics with endless love for so many years, and especially to my dearest husband Zhenglu for his understanding and eternal love, which give me the courage to overcome any difficulties in life with a full heart of happiness.

Finally I would like to acknowledge the finance support of the China Scholarship Council and the EQuS center.

Keywords

quantum superconducting circuit, transmon, quantum trajectory, single photon detection, cross-kerr nonlinearity, cavity opto-mechanics, coupled-resonator induced transparency, bifurcation, limit cycle, weak impulsive force detection

Australian and New Zealand Standard Research Classifications (ANZSRC)

ANZSRC code: 020604 Quantum Optics, 60%

ANZSRC code: 020404 Electronic and Magnetic Properties of Condensed Matter; Superconductivity 20%

ANZSRC code: 020603 Quantum Information, Computation and Communication 20%

Fields of Research (FoR) Classifications

FoR code: 0206, Quantum physics, 100%

Contents

List of Figures

List of Tables

List of Abbreviations

Abbreviation	Meaning
APD	Avalanche photodiode
CRIT	Coupled-resonator induced transparency
CROW	Coupled-resonator optical waveguide
DOS	Density-of-states
EIT	Electromagnetically induced transparency
FME	Fock-state master equation
HEMT	High-electron-mobility transistor
JPA	Josephson parametric amplifier
PMT	photomultiplier tube
POVM	Positive Operator-Valued Measure
QED	Quantum electrodynamics
QND	Quantum non-demolition
RWA	Rotating wave approximation
SME	Stochastic cascaded master equation
SNR	Signal-to-noise
SPM	Self-phase modulation
SQUID	Superconducting-quantum-interference-device
XPM	Cross-phase modulation

Chapter 1

Introduction

Since early 20th century, especially after the realization of isolating and manipulating single quantum systems in 1970s, quantum physics has made dramatic progress in fundamental quantum physics and applications in quantum information processing.

A new class of engineered quantum systems, such as quantum superconducting circuits and quantum micro/nano mechanical systems, have impressed the world with their advantages over natural systems in applications of quantum computing and research of radiation-matter interaction. In particular, quantum superconducting circuits are stable solid-state systems, mature in fabrication techniques, flexible in quantum control and strong in radiation-matter interaction, which makes them a promising platform for quantum computing. To fully realise the quanutm toolbox in solid-state quantum technologies, there are a few key ingredients, such as superconducting qubits, microwave photon sources, microwave photon detectors, quantum gates of qubits and memory units.

To this end, the first topic of thesis is focused on a non-absorbing high-efficiency detector for single microwave photons, which is still a missing piece in microwave photonics and microwave information science.

The second topic of this thesis is the cavity optomechanics, which is an intersection of optical cavities and micro/nano mechanical resonators. The well-developed micro/nano fabrication technologies and cooling techniques enable mechanical resonators show quantum effects. With the merits of optical resonators and mechanical resonators, cavity optomechanical systems become a useful tool in fundamental physics investigation, ultrasensitive sensing and quantum information processing. In this thesis we study nonlinear phenomena of a coupled-resonator system with optomechanical interaction and finally a potential

application of the system for weak impulsive force sense is proposed.

1.1 Outline of the thesis

The present thesis is organized as follows: Chapter 2 starts with an overview of the basics of quantum superconducting circuits, including the quantization of electric circuits, coplanar transmission lines and transmon qubits. These are the building blocks of the models in Chapter 3 and Chapter 4. Then the theories of quantum measurements and quantum trajectories are introduced and an example of a two-level system is used to illustrate the application of quantum trajectories in the measurement of an open quantum system. The last two sections of Chapter 2 introduce two formulations used for treating quantum systems with single-photon or Fock-state inputs.

In Chapter 3, the feasibility of a cross-Kerr-like nonlinearity induced by a three-level transmon in an open transmission line for single photon counting is investigated. A short review on the cross-Kerr effect is given in the beginning, which is followed by the derivation of an effective cross-Kerr model in the dispersive coupling regime. After that, a scheme for single microwave photon counting using the cross-Kerr interaction between two microwave fields mediated by a transmon is presented. By stochastic simulations of the model in the quantum frame with inclusion of spontaneous emissions of the transmon, it is shown that the transmon transition saturates, limiting its efficacy for photon detection. Besides the basic configuration, other configurations like a squeezed probe, N-transmon ensemble, N cascaded transmons and the N-type four-level system are studied for photon counting and the results turn out to agree with that of the basic configuration in the relevant limits..

In Chapter 4 we present an improved scheme to overcome the limitations in the single-photon counting. In this scheme a probe cavity is added to enhance the signal photon induced probe displacement. We show a substantial improvement compared to the performance established in chapter 3. Due to the non-Gaussian property of the statistics, another quantity–the distinguishability between one photon and zero photon is used to evaluate the detection efficiency and in the single transmon case the distinguishability is about 84.0$\%$ with an optimal linear filter and 84.65$\%$ with a nonlinear filter. Second, one more transmon-

cavity system is cascaded through a unidirectional circulator to further improve the detection performance and the distinguishability is improved to 90%. Additionally, the measurement induced pulse distortion and decoherence effect are discussed.

Chapter 5 is concerned with opto-mechanical resonator. It describes various nonlinear dynamics of a coupled-resonator and optomechanical system. The coupled-resonator induced transparency (CRIT) is introduced first, followed by the review of nonlinear dynamics, linearized analysis method and bifurcations. Then, a brief introduction to cavity optomechanics is given. After that, a model with two coupled resonators with one resonator vibrating is studied. It is observed that there are saddle-node and Hopf bifurcations in the system equilibrium diagram and bistability and limit cycles occur due to the two bifurcations. Moreover, the influence of opto-mechanical interacton on the CRIT effect is studied and it is shown that weak impulsive forces can be detected with good sensitivity at the narrow and bistable CRIT window.

Finally, a short summary of the thesis and potential future work are given in Chapter 6.

Chapter 2

Basic concepts and theories

2.1 A single photon and its detection

A photon is the basic excitation and the smallest energy unit of the electromagnetic field. The name of photon was introduced by Lewis in 1926 Lewis (1926). In fact, as early as in 1900 Planck proposed the quantization of harmonic oscillators in a black body which radiates electromagnetic fields to explain the black-body radiation Planck (1900) and in 1905 Einstein for the first time used the concept of the light quanta for interpreting the photoelectric effect Einstein (1905).

Strictly speaking, a single photon can never be exactly monochromatic, instead, its state can be expressed as a superposition of different spectral modes:

$$|1\rangle = \int_{-\infty}^{+\infty} f(\omega)\hat{a}^{\dagger}(\omega)d\omega|0\rangle \tag{2.1}$$

where $\hat{a}^{\dagger}$ is the creation operator of photons with frequency ω and the distribution coefficient $f(\omega)$ satisfies $\int_{-\infty}^{+\infty} |f(\omega)|^2 = 1$, which indicates that the total photon number integrated over all modes is 1. Since its photon number is fixed, its phase (the conjugate variable to the number) is completely random, according to the Heisenburg uncertainty relation.

Single photons have been playing significant roles in testing foundations of quantum mechanics Shadbolt et al. (2014), quantum cryptography Beveratos et al. (2002a) and quantum computation Knill et al. (2001). Since very early days, photons have been used to perform experiments for testing wave-particle duality Taylor (1909) and nonlocality Freedman and Clauser (1972) and many other basic concepts in quantum mechanics. Photons have multi-

ple degrees of freedom (polarization, energy and momentum) which can be used to encode information. They are excellent information carriers between processors and memory devices, often referred as "flying qubit". Another important application of photons is quantum computation, especially the linear optics quantum computation Knill et al. (2001), which is realized by linear optics and measurements of single photons.

Since photons are so crucial to the fundamental physics and a wide range of applications, the production and detection of them is essential. Up to now, there are various ways to produce single photons Eisaman et al. (2011). One mature experimental approach to prepare single photon sources is to generate a pair of photons through the parametric down conversion process Aspect et al. (1981); Kwiat and Chiao (1991) or four-wave mixing process Smith et al. (2009) in nonlinear crystals and atomic systems. This type of photon source is heralded but not on demand. Another promising approach is to use a single microscopic emitter. The emitter can be a quantum dot Chang et al. (2006), a NV center Beveratos et al. (2002b), a trapped ion Keller et al. (2004) and an atom Hijlkema et al. (2007); McKeever et al. (2004). These sources are more controllable and have higher efficiency. Other than these two methods, there are some less frequently used novel schemes, such as converting or truncating a coherent state to a single-photon state Fan et al. (2009); Pegg et al. (1998).

The history of photodetection can date back to mid-20th century. In 1960s, Glauber and Mandel developed quantum theory for photodetection Glauber (1963a); Mandel et al. (1964) and afterwards a variety of photon detection mechanisms and experimental demonstrations appeared. In the visible, near infrared and infrared ranges, there are various commercial photon detectors Eisaman et al. (2011), such as the photomultiplier tube (PMT), the avalanche photodiode (APD) Lacaita et al. (1996); Yuan et al. (2007), the semiconducting quantum dot detector Komiyama et al. (2000), the superconducting single photon detector Rosfjord et al. (2006) and the up-conversion photon detector Albota and Wong (2004). There are also proposals for detecting single photons in the quantum non-demolition fashion Helmer et al. (2009); Munro et al. (2005a); Reiserer et al. (2013). However, in the microwave range and radio frequency range, a practical photon detector is still a missing piece.

One of key objects appearing in the following chapters is the microwave photon. A mi-

crowave photon is a photon in the microwave regime, typically $10^5 \sim 10^6$ times less energy per photon than a visible photon. Its applications ranges from astronomy to nanoscale devices. Especially, in a quantum superconducting circuit, microwave photons are the basic information carriers. As quantum superconducting circuits are looking more and more promising as a stable solid-state platform for quantum computing, the demand for the sources and detectors of microwave photons become more and more urgent. Single microwave photons can generated from emission of a single superconducting qubit inside a cavity Bozyigit et al. (2011); Houck et al. (2007), but most of the recent experiments at the single quantum level in quantum superconducting circuit systems use faint coherent microwave fields as approximate single microwave photon sources. Single microwave photons and faint coherent microwave fields are either confined as standing waves in a superconducting resonator or traveling along a transmission line, in order to be efficiently coupled with superconducting qubits.

Due to their extremely low energy, the detection of single microwave photons is very challenging. Despite this, single photon schemes have attracted lots of attention and there are a number of excellent pioneering theoretical proposals and experimental demonstrations Chen et al. (2011); Guerlin et al. (2007); Johnson et al. (2010); Peaudecerf et al. (2014); Peropadre et al. (2011); Romero et al. (2009a,b); Sathyamoorthy et al. (2014). The proposals and experiments on single microwave photon detection can be roughly summarized in terms of a few types. The first type is absorptive detection and it usually happens in a Lambda-type three-level system Chen et al. (2011); Peropadre et al. (2011); Romero et al. (2009a,b). A single microwave photon excites the system to the excited state and the excited state then rapidly decays to a metastable level or continuum, which is macroscopically detectable Guerlin et al. (2007); Johnson et al. (2010); Peaudecerf et al. (2014). The second type of detection method stores a single microwave photon in a high-Q cavity and, during the life time of the photon, the probe mode coupled to the single photon can be measured many times. Another type of detection method non-destructively measures a propagating microwave photon using the nonlinear response of a three-level transmon Sathyamoorthy et al. (2014). An alternative way to measure microwave field is intensity measurements by signal amplification using a High-electron-mobility transistor (HEMT) Mimura (2002) or a Josephson parametric amplifier (JPA) Yurke (1987). All these schemes are making impor-

tant steps towards a practical single microwave photon detector from both theoretical and experimental aspect.

2.2 Quantum superconducting circuits and transmon qubits

2.2.1 Quantum circuits

Conventionally, electrical circuits are described by classical laws, such as Kirchhoff's voltage and current laws. The key circuit elements are capacitors and inductors and the circuit dynamics are characterized by classical variables. Since quantum properties of various systems, such as atomic ensembles, large molecules and micro-mirrors, have been explored and demonstrated, it is natural to investigate the quantumness of electric circuits.

Being a large and complex system, there are inevitable sources of noises and decoherence in an electrical circuit. Therefore, there are a few requirements for an electrical circuit to behave quantum mechanically Devoret (1995). Firstly, thermal noises have to be significantly suppressed, i.e., the energy of thermal fluctuations K_BT should be much lower than the typical energy of the circuit $\hbar\omega_0$. For instance, at the temperature of $1K$, $K_BT/\hbar \approx 20\mathrm{GHz}$, it is impossible to resolve the dynamics of a qubit with transition frequency at a few GHz. Therefore, cooling of eletrical circuits is an inevitable step. Currently, the typical operation temperature of quantum circuit experiments is a few tens of mK. Secondly, large dissipation of electrical circuits should be avoided in order to obtain long coherence time. Fortunately, the discovery of superconductivity makes this condition be easily satisfied. The existing of the superconducting energy gap makes superconducting electrons (Cooper pairs) in a superconductor free from dissipative scattering, leading to a long-range coherence of a superconductor. Therefore, metallic parts of quantum circuits are made of superconducting materials such as aluminum and niobium.

Besides, the inclusion of Josephson junctions makes electrical circuits exhibit nonlinearities and therefore energy levels suitable for artificial atoms are prepared. These superconducting artificial atoms interacting with microwave resonators implement a new type of cavity

quantum electrodynamics (QED), the so-called circuit QED Blais et al. (2004); Schoelkopf and Girvin (2008).

The field of quantum circuits has made impressive advances in the last decade. From the fundamental physics side, quantum circuits have been used to demonstrate the dynamical Casimir effect Wilson et al. (2011), to mimic the behavior of natural atoms You and Nori (2011), to test the violation of a Bell inequality Ansmann et al. (2009) and so on. In terms of applications in quantum information, quantum circuit technology is a very promising candidate for on-chip quantum computation Plantenberg et al. (2007); Yamamoto et al. (2003), thanks to system stability, mature techniques of fabrication and integration, long coherence of superconducting qubits Rigetti et al. (2012), the ability to interface with variety of systems Xiang et al. (2013), and strong coupling between qubits and field Niemczyk et al. (2010); Wallraff et al. (2004). Especially, hybrid systems of quantum circuits with atomic systems Deng et al. (2010); Verdú et al. (2009), spins Kubo et al. (2011); Zhu et al. (2011), quantum dots Childress et al. (2004) and other systems have shown their great promise in connecting optical and microwave frequency, information transfer between solid-state devices to flying qubits and forming more controllable quantum systems.

2.2.2 Quantization of electrical circuits

In this section I will give a brief review of the quantization of electrical circuits and more systematic theories can be found in Devoret (1995).

I first consider the simplest electrical circuit, the L-C circuit, shown in Fig. 2.1(b). The dynamics of a L-C circuit is the same as a harmonic oscillator (Fig. 2.1(a)) Feynman (1965). The flux Φ and the charge Q of a circuit play the roles of the position X and the momentum P in a harmonic oscillator. The analogy between these two models is presented in Table 1.1.

Following a similar procedure to that used in the quantization of a harmonic oscillator, clas-

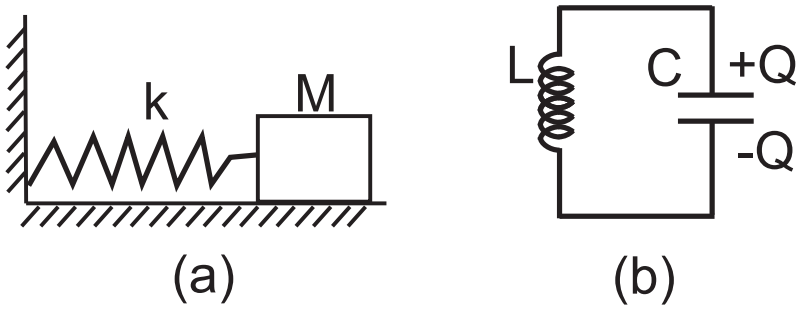

Figure 2.1 – (a) a harmonic oscillator system; (b) a L-C circuit.

sic variables Φ and Q are replaced by quantum operators $\hat{\Phi}$ and $\hat{Q}$:

$$\begin{aligned} Q &\rightarrow \hat{Q} \\ \Phi &\rightarrow \hat{\Phi} \end{aligned} \tag{2.2}$$

and we have the commutation relation $[\hat{\Phi}, \hat{Q}] = i\hbar$, where $\hat{Q} = i\hbar\frac{\partial}{\partial\Phi}$ and $\hat{\Phi} = -i\hbar\frac{\partial}{\partial\hat{Q}}$. The Hamiltonian of the L-C circuit is given by

$$\begin{aligned} \hat{H} &= \frac{\hat{Q}^2}{2C} + \frac{\hat{\Phi}^2}{2L} \\ &= \hbar\omega_0(\hat{a}^\dagger\hat{a} + \frac{1}{2}) \end{aligned} \tag{2.3}$$

here $\omega_0 = 1/\sqrt{LC}$ is the frequency of the L-C resonator and the operator

$$\hat{a} = \frac{\hat{\Phi}}{\Phi_0} + i\frac{\hat{Q}}{Q_0} \tag{2.4}$$

with $\Phi_0 = \sqrt{2\hbar Z_0}$, $Q_0 = \sqrt{2\hbar/Z_0}$ and $Z_0 = \sqrt{L/C}$. Z_0 is the characterization impendence,

Spring-Mass system	L-C circuit
$H(X,P) = \frac{kX^2}{2} + \frac{P^2}{2M}$	$H(\Phi,Q) = \frac{\Phi^2}{2L} + \frac{Q^2}{2C}$
Position X	Flux Φ
Momentum P	Charge Q
Spring stiffness k	Capacitance $1/L$
Mass M	Inverse of inductance C

Table 2.1 – The analogy between a harmonic oscillator and a L-C circuit.

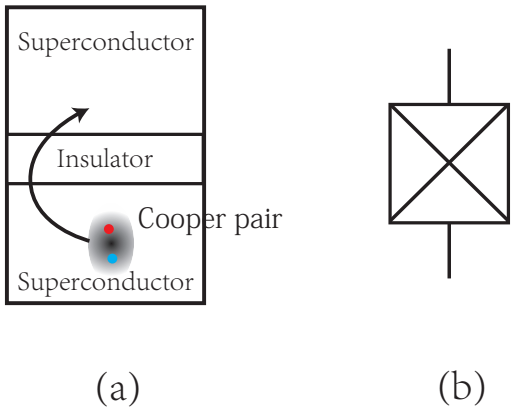

Figure 2.2 – (a). A Josephson junction consists of two superconducting electrodes connected via a thin insulator. (b). Circuit representation of a Josephson junction–a boxed cross.

a typical value for it in quantum circuit systems is 50 Ohm.

Circuits consisting of linear elements like capacitors and inductors are harmonic oscillators, thus their energy levels are evenly-spaced. To have atom-like unevenly-spaced energy levels, or anharmonicity, nonlinear elements are required. In available quantum circuit systems, the key nonlinear ingredient is the Josephson junction, which offers the nonlinearity for superconducing qubits Clarke and Wilhelm (2008), Josephson parametric amplifiers Yurke (1987), superconducting-quantum-interference-devices (SQUID) Clarke and Braginski (2004) and other important components of quantum circuits. A Josephson junction is a junction with two superconducting electrodes sandwiching a thin insulating layer (see Fig. 2.2 (a)), behaving as a dissipationless nonlinear inductor in a electric circuit and providing the anharmonicity for forming an artificial superconducting atom.

Superconducting circuit experiments operate at very low temperature, i.e., a few tens of mK. Electrons in such circuits are correlated in pairs (Cooper pairs), which form superconductors in two nodes of Josephson junctions. As stated in the celebrated Josephson effect Josephson (1962)Tinkham (2012), Cooper pairs are able to tunnel across the insulating barrier and there is a relation between the current of Cooper pairs and the phase difference of two superconductors:

$$I = I_c \sin(\delta) \tag{2.5}$$

where I_c is the critical current and $\delta = 2\pi\Phi/\Phi_0$ is the dimensionless phase difference of two superconductors in a Josephson junction with $\Phi_0 = h/2e$ the superconducting flux quantum. The tunneling energy is

$$\begin{aligned} \mathcal{E}_J &= \int_{-\infty}^{t} I(\tau)V(\tau)d\tau \\ &= \frac{\hbar I_c}{2e}\int_{\infty}^{t}\sin(\delta(\tau))\dot{\delta}(\tau)\mathrm{d}\tau \\ &= -E_J\cos(\delta(t)) \end{aligned} \tag{2.6}$$

where $E_J = \hbar I_c/2e$. In 2.7, the relation $V = \dot{\phi_J} = \hbar\dot{\delta}/2e$ was used. δ is the dimensionless phase difference between two superconductors of a junction. Eqs. (2.5) and (2.7) shows nonlinear dependence of the current and the tunnelling energy on the phase difference.

One can describe properties of a Josephson junction in terms of the charge number passing the junction or in terms of the phase difference. Quantum mechanically, the number of Cooper pairs passing the junction should be described by an operator,

$$\hat{n} = \sum_n n|n\rangle\langle n| \tag{2.7}$$

The conjugate operator to the number operator $\hat{n}$ is the phase operator $\hat{\delta}$, which is defined as:

$$e^{i\hat{\delta}} = \sum_{-\infty}^{+\infty}|n\rangle\langle n+1| \tag{2.8}$$

and it is easily to calculate that $e^{i\hat{\delta}}|n+1\rangle = |n\rangle$ and $[\hat{\delta},\hat{n}] = i$. Thus one can write the phase in the charge number basis by a Fourier transformation:

$$|\delta\rangle = \sum_n \mathrm{e}^{in\delta}|n\rangle \tag{2.9}$$

Similarly, the charge number can be written in the phase basis:

$$|n\rangle = \frac{1}{2\pi}\int_0^{2\pi} d\delta \mathrm{e}^{-in\delta}|\delta\rangle \tag{2.10}$$

where the periodic property of the phase was considered.

Based on these, the Josephson tunneling Hamiltonian in a charge basis can be obtained:

$$\begin{aligned}
\hat{H}_J &= -E_J\cos(\hat{\delta}) \\
&= -\frac{E_J}{2}\frac{1}{2\pi}\int_0^{2\pi} d\delta(\mathrm{e}^{i\delta}+\mathrm{e}^{-i\delta})|\delta\rangle\langle\delta| \\
&= -\frac{E_J}{2}\frac{1}{2\pi}\int_0^{2\pi} d\delta(\mathrm{e}^{i\delta}+\mathrm{e}^{-i\delta})\sum_n\sum_{n'}\mathrm{e}^{in\delta}|n\rangle\langle n'|\,\mathrm{e}^{-in'\delta} \\
&= -\frac{E_J}{2}\frac{1}{2\pi}\int_0^{2\pi} d\delta\sum_n\sum_{n'}(\mathrm{e}^{i\delta(n+1-n')}+\mathrm{e}^{-i\delta(n'+1-n)})|n\rangle\langle n'| \\
&= -\frac{E_J}{2}\sum_n\sum_{n'}(\delta_D(n+1-n')+\delta_D(n'+1-n))|n\rangle\langle n'| \\
&= -\frac{E_J}{2}\sum_n(|n\rangle\langle n+1|+|n+1\rangle\langle n|)
\end{aligned} \tag{2.11}$$

where δ_D denotes the Dirac delta function and the completeness condition $\frac{1}{2\pi}\int_0^{2\pi} d\delta|\delta\rangle\langle\delta| = 1$ was introduced.

In addition, the Josephson tunneling Hamiltonian can be also written in the phase basis:

$$\begin{aligned}
\hat{H}_J &= -E_J\cos(\hat{\delta}) \\
&= -\frac{E_J}{2\pi}\int_0^{2\pi} d\delta|\delta\rangle\cos(\delta)\langle\delta|\,.
\end{aligned} \tag{2.12}$$

It is worthy to mention that in a junction made of two normal conductors and an insulating barrier single electron tunneling occurs. However, this type of process is dissipative since single electrons are subject to normal resistive scattering processes. Therefore, Josephson junctions are extremely important components for providing dissipationless nonlinearities.

2.2.3 Coplanar transmission lines and microwave resonators

In superconducting circuits, the role of a transmission line is like a waveguide in optical systems, supporting the propagation of traveling microwave fields. The transmission line

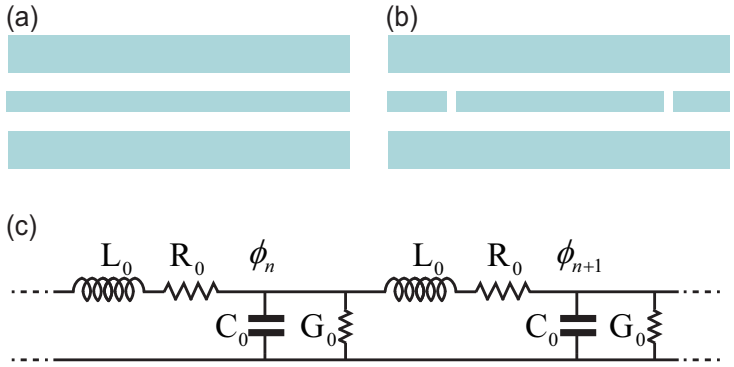

Figure 2.3 – (a). Sketch of a coplanar transmission line. (b). Sketch of a coplanar transmission line resonator. (c).The circuit representation of a coplanar transmission line. L0, C0, R0 and G0 are the inductance, capacitor, resistance and conductance of unit length of the circuit.

we would like to discuss here is the coplanar transmission line, which is consisted of a central conductor and two lateral ground plane in the same plane, see Figure 1.3 (a). The central conductor is used for propagating microwave signals and the lateral ground planes are used as the reference potential. Figure 1.3 (c) is the circuit representation of a coplanar transmission line and it can be taken as an infinitely-long chain of L-C oscillators for small conductance (G_0) and small resistance (R_0).

The Lagrangian is

$$\mathcal{L}(\phi_1, \dot{\phi}_1, ...\phi_N, \dot{\phi}_N) = \sum_{n=1}^{N}(\frac{C_0\dot{\phi}_n^2}{2} - \frac{(\phi_n - \phi_{n-1})^2}{2L_0}) \tag{2.13}$$

In the limit of $N \to \infty$, Eq. 1.10 can be transformed to the frequency domain as

$$\mathcal{L}(\Phi_1, \dot{\Phi}_1, ...) = \sum_{n}^{\infty}(\frac{C_n\dot{\Phi}_n}{2} - \frac{\Phi_n^2}{2L_n}) \tag{2.14}$$

where $C_n = C_0 d/2$, $L_n = 2dL_0/(n^2\pi^2)$ and d is the length of the transmission line. After quantization using the same procedure as in the quantization of the L-C circuit, the quantized Hamiltonian for a coplanar transmission line is

$$\hat{H} = \hbar\sum_{n}\omega_n(\hat{a}_n^\dagger\hat{a}_n + \frac{1}{2}) \tag{2.15}$$

with $\omega_n = n\pi/(\sqrt{C_0L_0}d)$. There are plenty of microwave field modes co-propagate in a

transmission line.

If two gap capacitors are made on the center conductor of a coplanar transmission line, a transmission line resonator forms, which is also called the coplanar waveguide resonator Göppl et al. (2008) (Figure 1.3 (b)). The two capacitors act like reflective mirrors in conventional optical cavities and they are used to coupled to input and output transmission lines. The typical frequency of a coplanar waveguide resonator ranges from 2 GHz to 10 GHz and the typical quality factor $\mathcal{Q}$ is about $10^5 - 10^6$ thanks to the low loss rate. Besides, since very small resonator volume, microwave fields in the resonators can be very intense and therefore very strong field-atom interaction can be achieved in transmission line resonators.

2.2.4 Superconducting qubit and transmon

As discussed in section 2.2.2, Josephson junctions provides dissipationless nonlinearities needed for building artificial atoms in quantum circuits. Up to now, researchers have already developed various types of superconducting qubits, classified as the charge qubit Bouchiat et al. (1998); Nakamura et al. (1999), the flux qubit Friedman et al. (2000); Van der Wal et al. (2000) and the phase qubit Martinis et al. (2002) according to the different ratio of the charge energy over the josephson tunneling energy. There are also superconducting qubits in the intermediate regimes of the three categories, such as the transmon Koch et al. (2007a) and fluxonium Manucharyan et al. (2009). The one involved in my PhD projects is the transmon.

The transmission-line shunted plasma oscillation qubit, in short, transmon Koch et al. (2007a), is one of the most promising superconducting qubits. It was developed in 2007 as a charge insensitive superconducting qubit Koch et al. (2007a). As shown in Fig. 2.4, it is a loop containing two Josephson junctions and shunted with a large capacitor. This capacitor largely reduces the ratio of E_c/E_J and the charge dispersion decreases as the ratio increases exponentially while the aharmonicity of energy levels decreases in a power law. This makes transmons insensitive to the change fluctuations with only little anharmonicity sacrificed Cottet (2002); Koch et al. (2007a).

Transmons have been involved in many important milestones of quantum circuits, such as

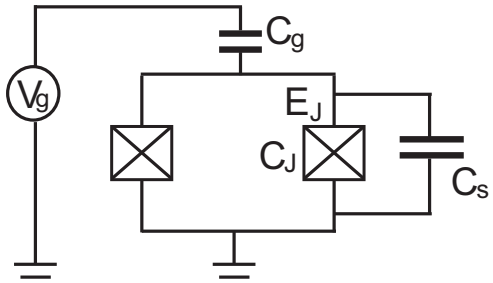

Figure 2.4 – The circuit representation of a transmon: a SQUID loop shunted by an external large capacitor C_s. The shunt capacitor decreases the charge energy E_c and leads to a large ratio E_J/E_c.

implementation of Toffoli gate Fedorov et al. (2011), giant cross-Kerr effect Hoi et al. (2013), vacuum Rabi splitting Bishop et al. (2009) in quantum circuits. Recently, three-dimensional transmon qubits have been demonstrated, exhibiting longer coherence times, up to tens of μs Rigetti et al. (2012), much longer than that of a transmon in the coplanar structure.

The transmon has the same mathematical description as the Cooper pair box. In the following the Hamiltonian for a Cooper pair box/transmon will be derived. The charge energy is analogous to the kinetic energy as

$$T = \frac{C_\Sigma}{2}\dot{\phi}_J^2 = \frac{(Q_j - C_g V_g)^2}{2C_\Sigma} \tag{2.16}$$

and the Josephson coupling energy is analogous to the potential energy as

$$U = -E_J \cos(\delta) - \mathrm{V_g C_g}\dot{\phi}_\mathrm{J} \tag{2.17}$$

where E_J is the Josephson tunneling energy. The Lagrangian is

$$\begin{aligned} \mathcal{L} &= T - U \\ &= \frac{C_\sigma}{2}\dot{\phi}_J^2 + E_J \cos(\delta) + \mathrm{V_g C_g}\dot{\phi}_\mathrm{J} \end{aligned} \tag{2.18}$$

The canonical momentum (here the charge variable) is

$$Q_J = \frac{\partial \mathcal{L}}{\partial \dot{\phi}_J} = C_\Sigma \dot{\phi}_J + V_g C_g \tag{2.19}$$

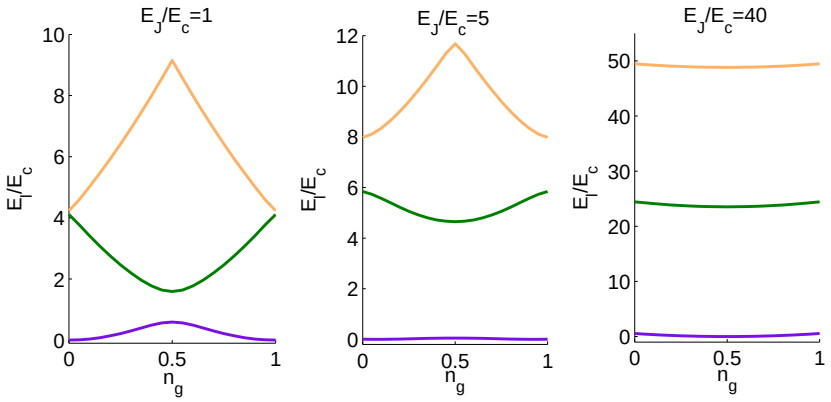

Figure 2.5 – The lowest three energy levels of a Cooper pair box/transmon versus the gate charge n_g at three different ratios of E_J/E_C.

and the Hamiltonian is

$$\begin{aligned} \mathcal{H} &= Q_J\dot{\phi}_J - \mathcal{L} = \frac{C_\Sigma}{2}\dot{\phi}_J^2 - E_J\cos(\delta) \\ &= \frac{(Q_J - C_gV_g)^2}{2C_\Sigma} - E_j\cos(\delta) \\ &= 4E_C(n-n_g)^2 - E_J\cos\delta \end{aligned} \tag{2.20}$$

where $n_g = C_\Sigma V_g/(2e)$ and $E_C = e^2/(2C_\Sigma)$ is the charge energy.

Using the number and phase operators defined before, the quantized Hamiltonian of a single Cooper-pair box or a transmon in a charge number basis is given by

$$\hat{H} = 4E_C\sum_{n=0}^{\infty}(n-n_g)^2\left|n\right\rangle\left\langle n\right| - \frac{E_J}{2}\sum_n(\left|n\right\rangle\left\langle n+1\right| + \left|n+1\right\rangle\left\langle n\right|) \tag{2.21}$$

The eigenenergies can be calculated by diagonalizating the Hamiltonian 2.21 in a truncated number basis. Fig. 2.5 presents the dependence of energy levels on the off-set gate charge n_g (the charge dispersion) at three different values of E_J/E_C. The influence of the ratio E_J/E_C on the energy structure has two aspects. On one hand, from Fig. 2.5 one can see that the charge dispersion is largely reduced as the ratio E_J/E_c rises. The larger the ratio E_J/E_C, the flatter the energy levels, which indicates better immunity ability from charge noises. This is consistent with the conclusion in Koch et al. (2007a): charge dispersion values of energy levels exponentially decays with $\sqrt{8E_J/E_C}$.

On the other hand, the charge insensitivity is at the price of the reduction of anharmonicity. As discussed in Koch et al. (2007a), the anharmonicity changes from positive to negative values around $E_J/E_C = 9$ at the charge degenerate point and in the regime $E_J/E_C \gg 1$ there is an approximate solution for the n_{th} transition energy $\sqrt{8E_JE_C} - n_{th}E_C$ and the relative anharmonicity is

$$|\mathcal{A}| = \frac{|E_{21} - E_{10}|}{E_{1,0}} \approx \sqrt{E_C/(8E_J)} \tag{2.22}$$

It is clear that the anharmonicity $\mathcal{A}$ reduces with the increase of E_J/E_C. However, compared to the exponentially decaying dependence of the charge dispersions on E_J/E_C, the anharmonicity decreases algebraically and slowly as E_J/E_C increases. Therefore, transmons operates at the ratio $E_J/E_C \gg 1$, typically $10 \sim 100$ Koch et al. (2007a). For instance, for a transmon with $7\mathrm{GHz}$ first transition frequency and the ratio $E_J/E_C = 50$, the anharmonicity $\mathcal{A} \approx 364\mathrm{MHz}$.

Since energy levels of transmons are well distinguished, different transitions can be addressed individually by applying suitable coupling fields. In Eq. 2.21, if we select the lowest transition, the Hamiltonian can be presented in the spin representation:

$$\hat{H} = 4E_C(1 - n_g)^2\hat{\sigma}_z - \frac{E_J}{2}\hat{\sigma}_x \tag{2.23}$$

where $\hat{\sigma}_z$ and $\hat{\sigma}_x = \hat{\sigma}_- + \hat{\sigma}_+$ are the Pauli matrices. It is easy to transform Eq. 2.23 to a diagonal basis by a basis rotating:

$$\hat{H} = \hbar\omega_{01}\hat{\sigma}'_z \tag{2.24}$$

where $\omega_{01} = \sqrt{4E_C^2(1 - n_g)^2 + E_J^2}$.

There are two important parameters of superconducting qubits worthy to mention, T_1 and T_2, which characterize their coherence properties. T_1 is defined as $T_1 = 1/\gamma$, with γ the decay rate of the excited state population and T_2 is defined as $T_2 = 1/(\gamma/2 + \gamma_{dp})$, with γ_{dp} the decay rate of the qubit polarization. For the first transition of a transmon, the dephasing is usually negligibly small, $T_2 \approx 2T_1$.

2.2.5 Circuit QED

As a cavity QED system in electrical circuits, circuit QED studies quantum interaction between electromagnetic fields and “atom". Here “atoms" are superconducting artificial atoms and fields are microwaves in resonators. As an example, the system under consideration is a transmon qubit interacting with a single-mode microwave field in a one-dimensional transmission line resonator. The transmon-field coupling is the dipole coupling. From Eq. 2.24, a transmon can be modeled as a two-level system and a resonator is modeled as a quantum harmonic oscillator. The Hamiltonian describing the transmon-resonator system is given by ($\hbar = 1$)

$$\hat{H} = \omega_r \hat{a}^\dagger \hat{a} + \omega_0 \hat{\sigma}_z + g(\hat{a} + \hat{a}^\dagger)(\hat{\sigma}_- + \hat{\sigma}_+) \tag{2.25}$$

At the regime of the transition frequency much larger than the coupling, $\omega_0 \gg g$, the Hamiltonian 2.25 can be rewritten by the rotating wave approximation (RWA):

$$\hat{H} = \omega_r \hat{a}^\dagger \hat{a} + \omega_0 \hat{\sigma}_z + g(\hat{a}^\dagger \hat{\sigma}_- + \hat{a}\hat{\sigma}_+) \tag{2.26}$$

For the resonator frequency ω_r resonate with the qubit transition frequency ω_0, we have the interaction Hamiltonian:

$$\hat{H}_I = g(\hat{a}^\dagger \hat{\sigma}_- + \hat{a}\hat{\sigma}_+) \tag{2.27}$$

This Hamiltonian only interacts with states $\mu|g, n\rangle + \nu|e, n-1\rangle$. Acting the Hamiltonian 2.27 on states $\mu|g, n\rangle + \nu|e, n-1\rangle$, we have

$$\hat{H}_I(\mu|g, n\rangle + \nu|e, n-1\rangle) = g(\nu|g, n\rangle + \mu|e, n-1\rangle) \tag{2.28}$$

To satisfy the eigenstate property, we have $\mu = \pm\nu$; and for a normalized state $\mu^2 + \nu^2 = 1$. Thus we have $\mu = \nu = \pm 1/\sqrt{2}$ and the system eigenstates are

$$|\psi_\pm\rangle = (|g, n\rangle \pm |e, n-1\rangle)/\sqrt{2} \tag{2.29}$$

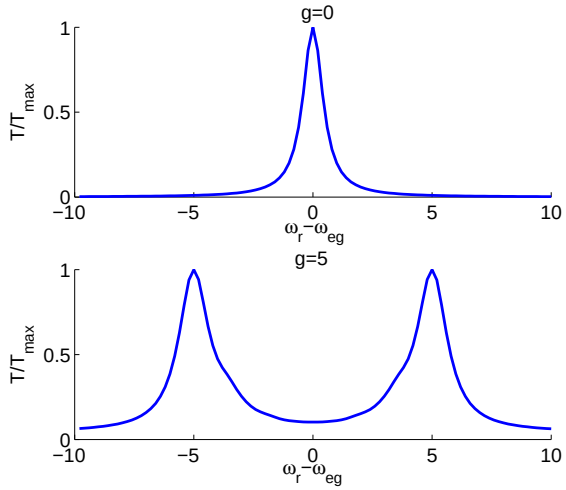

Figure 2.6 – The vacuum Rabi splitting in the transmission spectrum of a transmon-resonator system (T is the transmission rate). The system parameters are: $\gamma = \kappa = 1$ and $\varepsilon = 0.4$.

with eigenenergies $\pm\sqrt{n}g$. This is the mode splitting of a resonator induced by the interaction with a qubit, which is a signature of strong atom-field coupling, i.e. $g \gg \gamma, \kappa$. When $n = 0$, the mode splitting is referred as the vacuum Rabi splitting. In Fig. 2.6, the vacuum Rabi splitting in a transmon-field system is plotted and it is seen that the splitting distance of two modes is determined by the coupling strength. In superconducting circuits, vacuum Rabi splitting effects have been observed in a single Cooper-pair box Wallraff et al. (2004) and in a transmon Fink et al. (2008).

2.3 Quantum measurement and quantum trajectories

2.3.1 From a closed system to an open system

A closed system is a system which is isolated from the environment and other systems. The quantum dynamics of a closed system is described by the Schrödinger equation

$$d|\psi(t)\rangle/dt = -i\hat{H}|\psi(t)\rangle \tag{2.30}$$

The time evolution of the closed system is unitary. In fact, a closed system is an idealisation. No system is really isolated, instead, every system is surrounded by an environment and

exchanges information and energy with the environment. This kind of system is called the open system Breuer and Petruccione (2002). The interaction with the environment (or reservoir, bath) leads to energy dissipation and fluctuations of the system variables. There are a number of ways to model the dynamics of an open system and among them one widely-used theory is the quantum master equation in Lindblad form, i.e.,

$$\frac{d\rho_S}{dt} = -i[\hat{H}_s, \rho_S] + \sum_k \gamma_k(\hat{c}_k \rho_S \hat{c}_k^\dagger - \frac{1}{2}\hat{c}_k^\dagger \hat{c}_k \rho_S - \frac{1}{2}\rho_S \hat{c}_k^\dagger \hat{c}_k) \tag{2.31}$$

where $\hat{c}_k$ are the system operators coupled to the environment. The linear master equation 2.31 is the unconditional master equation, which describes the average result over an ensemble. The deterministic solutions of Eq. 2.31 can not describe the stochastic results from realistic quantum measurements. To further investigate the properties of an open system, stochastic Schrödinger equations or quantum trajectories Wiseman (1996); Wiseman and Milburn (2010) are needed.

2.3.2 Quantum measurement

Quantum measurement occupies an important position in quantum mechanics and its applications. It enables us to access quantum systems and characterize quantum phenomena through reading out classical variables. Also, quantum measurement is a way of engineering quantum systems, for instance, in a quantum feedback control process, the future dynamics of a quantum system can be altered by measurement records Wiseman (1996).

In quantum mechanics, a conventional way of describing quantum measurement is the projective measurement theory Nielsen and Chuang (2010)Wiseman and Milburn (2010), which is a special class of quantum measurements. Consider an observable $\hat{A}$ and it is decomposition as

$$\hat{A} = \sum_\lambda \lambda \hat{\Pi}_\lambda \tag{2.32}$$

where $\hat{\Pi}$ is the projector onto the eigenspace of observable $\hat{A}$ with a real eigenvalue λ. The measurement outcome is one of the eigenvalues of the observable. The probability of

outcome λ occurring is

$$p_\lambda = \langle\psi|\,\hat{\Pi}_\lambda|\psi\rangle \tag{2.33}$$

and the system state after the measurement with outcome λ is

$$|\psi\rangle' = \frac{\hat{\Pi}_\lambda|\psi\rangle}{\sqrt{p_\lambda}} \tag{2.34}$$

The projective quantum measurement theory fails in describing realistic quantum measurements. For example, due to noise added during a measurement process, a measurement result may not be an eigenvalue of a hermitian operator on the measured system. Another example is the heterodyne measurement, in which non-orthogonal phase and amplitude can be measured simultaneously.

To discuss more general and realistic quantum measurement, the “Positive Operator-Valued Measure" (POVM) Nielsen and Chuang (2010) will be introduced below. Before that, I would like to discuss about measurement operators first. In a quantum measurement, in general the system is not measured directly, instead, the radiated field from the system or the bath coupled to the system is directly measured and the measured result of the field or the bath infers the “measurement result" of the system. The bath is called a meter or an apparatus of the measurement. The measurement operator $\hat{M}$ for the system associated with a measurement result m of the bath was derived in Chapter one of Wiseman and Milburn (2010):

$$\hat{M}_m = \langle m|\,\hat{U}(t)|\theta\rangle \tag{2.35}$$

where $|\theta\rangle$ is the initial state of the bath and $\hat{U}$ is the evolution operator for the system-bath or system-meter interaction, which is given by Gardiner and Zoller (2004)

$$\hat{U}(t+dt,t) = \exp[\hat{\mathrm{c}}\mathrm{d}\hat{\mathrm{B}}_\mathrm{t}^\dagger - \hat{\mathrm{c}}^\dagger\mathrm{d}\hat{\mathrm{B}}_\mathrm{t} - \mathrm{i}\hat{\mathrm{H}}\mathrm{dt}] \tag{2.36}$$

Here $\hat{c}$ is the operator of the system under measurement coupled to the bath. Suppose that $\hat{b}(t)$ is the annihilation operator for the bath, the noise increment is defined as $d\hat{B}_t =$

$\int_t^{t+dt} \hat{b}(t)dt$, which satisfies $d\hat{B}_t d\hat{B}_t^\dagger = dt$ for a vacuum bath.

Now we move to the POVM. A POVM is a set of non-negative operators $\hat{E}_m = \hat{M}_m^\dagger \hat{M}_m$ which add up to identity $\sum_m \hat{E}_m = \hat{1}$. The set of operators can be orthogonal or non-orthogonal and when they are orthogonal the number of $\hat{E}_m$ is the same with the system Hilbert space dimension. Each operator $\hat{E}_m$ corresponds to one measurement output, with the probability

$$P_m = \mathrm{Tr}[\hat{\mathrm{E}}_\mathrm{m}\rho] = \mathrm{Tr}[\hat{\mathrm{M}}_\mathrm{m}\rho\hat{\mathrm{M}}_\mathrm{m}^\dagger]. \tag{2.37}$$

where the measurement result m can be an integer, fraction or even complex number. More importantly, the measurement result is not one of eigenvalues of an Hermitian operator corresponding to an observable but simply a measurement effect.

2.3.3 Quantum trajectories

A quantum trajectory is a time-evolution path of a conditional quantum state conditioned on measurement records Milburn (1996). It can be used for formulating a quantum measurement process and simulating and interpreting the behaviour of a quantum system suffered in a noisy environment. In the classic sense, a trajectory is usually continuous. Due to the nature of quantum mechanics, quantum trajectories can be discrete or continuous. When a system experiences discrete quantum jumps, quantum trajectories are discontinuous and for diffusion processes, quantum trajectories are continuous. These two types of trajectories are two different unravelings of quantum master equations. Different unraveling of one master equation is associated with different types of quantum measurements. For instance, quantum-jump-like unraveling corresponds to direct counting of photon number in a field while the unraveling with continuous trajectories corresponds to the Homodyne or Heterodyne measurement of quadrature(s) of a field. Later in this chapter, an example of a two-level atom using both jump-type and continuous quantum trajectories will be given.

2.3.3.1 Jump-type quantum trajectories

A quantum jump is a discontinuous change in a system state and it was first observed in a trapped ion system ITANO et al. (1987). Before that, due to the lack of techniques of isolating and trapping single quantum systems, average effect over ensembles makes it difficult to resolve quantum jumps. Here quantum jumps are discussed in the context of quantum trajectories, in which a quantum jump reflects a sudden change in the observer's knowledge when measurements are performed on a quantum system.

In terms of realization in experiments, jump-type quantum trajectories are associated with direct detection of photon number in a system under consideration. This type of quantum trajectories will be reviewed here following Chapter four of Wiseman and Milburn (2010).

For photon detection of a cavity output field, $\hat{c} = \sqrt{\kappa}\hat{a}$ with κ cavity decay rate and $\hat{a}$ cavity field operator. We assume that the initial state of the bath is the vacuum. If there is no click on the detector, the state of the meter is still vacuum and the measurement operator with no-detection is

$$\begin{aligned} \hat{M}_0 &= \langle 0|_B \hat{U}(t+dt,t)|0\rangle_B \\ &= \langle 0|_B (1 + \hat{c}d\hat{B}^\dagger - \hat{c}^\dagger d\hat{B} - i\hat{H}dt + \frac{1}{2}\hat{c}^\dagger\hat{c}d\hat{B}d\hat{B}^\dagger)|0\rangle_B \\ &\approx 1 + \frac{1}{2}\hat{c}^\dagger\hat{c}dt - i\hat{H}dt \end{aligned} \tag{2.38}$$

where the evolution operator was defined in Eq. 2.36. If there is a click on the detector, the state of the meter is $|1\rangle = d\hat{B}^\dagger|0\rangle/\sqrt{dt}$ and the measurement operator with detection is

$$\begin{aligned} \hat{M}_1 &= \langle 1|_B \, dU(t+\hat{dt},t)|0\rangle_B = \langle 0|_B \, d\hat{B}\hat{U}(t+dt,t)|0\rangle_B/\sqrt{dt} \\ &\approx \sqrt{dt}\hat{c} \end{aligned} \tag{2.39}$$

It is easy to verify that the completeness condition $\hat{M}_0^\dagger\hat{M}_0 + \hat{M}_1^\dagger\hat{M}_1 = 1$ is satisfied.

We define $N(t)$ as the number of counts up to time t and $dN(t)$ is the increment in the time

interval $[t, t+dt)$. As a point process, $dN(t) = N(t+dt) - N(t)$ is either 0 or 1 and

$$\begin{aligned} E[dN(t)] &= \left\langle \hat{M}_1^\dagger \hat{M}_1 \right\rangle = dt \left\langle \hat{c}^\dagger \hat{c} \right\rangle \\ dN^2(t) &= dN(t) \end{aligned} \tag{2.40}$$

$E[dN(t)]$ is the probability of $dN(t) = 1$, which is infinitesimally small. Therefore, for most of time no detection happens ($dN(t) = 0$) and the system evolves via the operator $\hat{M}_0$ as

$$\begin{aligned} |\psi_0(t+dt)\rangle &= \frac{\hat{M}_0(dt)|\psi(t)\rangle}{\sqrt{\left\langle \hat{M}_0^\dagger(dt)\hat{M}_0(dt) \right\rangle (t)}} \\ &= [\hat{1} - dt(i\hat{H} + \frac{1}{2}\hat{c}^\dagger\hat{c} - \frac{1}{2}\left\langle \hat{c}^\dagger\hat{c} \right\rangle (t))]|\psi(t)\rangle \end{aligned} \tag{2.41}$$

$|\psi_0(t+dt)\rangle$ is called the system state conditioned on “no detection".

Once the detection happens, $dN(t) = 1$, the system experiences a finite change by the measurement operator $\hat{M}_1$ and the system state condition of “$dN(t) = 1$" is given by

$$\begin{aligned} |\psi_1(t+dt)\rangle &= \frac{\hat{M}_1(dt)|\psi(t)\rangle}{\sqrt{\left\langle \hat{M}_1^\dagger(dt)\hat{M}_1(dt) \right\rangle (t)}} \\ &= \frac{\hat{c}|\psi(t)\rangle}{\sqrt{\langle \hat{c}^\dagger\hat{c} \rangle (t)}} \end{aligned} \tag{2.42}$$

This sudden change of the system state is called a quantum jump.

Combining the two situations conditioned on "no detection" and "have a detection" with their weights or probabilities $dN(t)$ and $1 - dN(t)$, the system evolution can be described by the stochastic Schrödinger equation:

$$\begin{aligned} d|\psi(t)\rangle &= [dN(t)\frac{\hat{c}}{\sqrt{\hat{c}^\dagger\hat{c}}} + (1 - dN(t))[1 - dt(-\frac{\left\langle \hat{c}^\dagger\hat{c} \right\rangle}{2} + \frac{\hat{c}^\dagger\hat{c}}{2} + iH)]]|\psi(t)\rangle \\ &= [dN(t)(\frac{\hat{c}}{\sqrt{\hat{c}^\dagger\hat{c}}} - 1) + dt(\frac{\left\langle \hat{c}^\dagger\hat{c} \right\rangle}{2} - \frac{\hat{c}^\dagger\hat{c}}{2} - iH)]|\psi(t)\rangle \end{aligned} \tag{2.43}$$

where I used $dN(t)dt = o(dt)$. The solutions to Eq. 2.43 are quantum trajectories of

the system under measurement. The conditional dynamics of a system observable can be obtained from the solutions $\psi(t)$. Due to the stochastic property of this equation, the conditional result from each single trajectory differs from that in other trajectories but these conditional results from all trajectories fluctuate around the unconditional result, which is obtained from the unconditional master equation 2.31. Eq. 2.43 is called one stochastic wave function unraveling of the stochastic master equation and it is not unique as mentioned before. It has advantage in saving computing resources but it can not handle with inefficient detection since in that case the system state is not a pure state.

The unconditional master equation in the Lindblad form can be derived from Eq. (2.43) by averaging over the ensemble $\rho = \mathrm{E}(|\psi\rangle \langle\psi|)$:

$$\dot{\rho} = i[\hat{H}, \rho] + \mathcal{D}[\hat{c}]\rho \tag{2.44}$$

Here the superoperator $\mathcal{D}$ is defined as

$$\mathcal{D}[\hat{r}]\rho = \frac{1}{2}(\hat{r}^\dagger \hat{r}\rho + \rho \hat{r}^\dagger \hat{r} - 2\hat{r}\rho\hat{r}^\dagger) \tag{2.45}$$

The first two terms are associated with the non-Hermitian evolution of the system and the third term is associated with the jump process induced by the measurement.

2.3.3.2 Diffusive quantum trajectories

The second type of quantum trajectory is the diffusive quantum trajectoryWiseman and Milburn (2010)Wiseman and Milburn (1993), which is the continuous limit of the jump-type quantum trajectory. This type of quantum trajectory corresponds to the homodyne detection or the heterodyne detection of a quantum system.

In a homodyne detection a radiated signal from the measured system is mixed with a strong local coherent field through a beam splitter (for optical signal) or a IQ mixer (for microwave signal) before reaching the detector. The strong local field is called the local oscillator, which is usually from the same source with the probe in the system.

The signal after mixing with the local oscillator through a beam splitter can be expressed by

the transformation of $\hat{c} \to \hat{c} + \varepsilon$ and $\hat{H} \to \hat{H} - i\frac{1}{2}(\varepsilon^* \hat{c} - \varepsilon \hat{c}^\dagger)$ (ε is the amplitude of the local oscillator.). Under this transformation, the unconditional master equation (3.26) is invariant. The stochastic Schrödinger equation (2.43) will be transformed to

$$\begin{aligned} d|\psi(t)\rangle &= (-i\hat{H} - \frac{1}{2}(\hat{c}^\dagger \hat{c} + \varepsilon \hat{x} - \left\langle \hat{c}^\dagger \hat{c} \right\rangle - \varepsilon \left\langle \hat{x} \right\rangle)|\psi(t)\rangle dt \\ &+ (\frac{\hat{c} + \varepsilon}{\sqrt{\langle (\hat{c}^\dagger + \varepsilon)(\hat{c} + \varepsilon) \rangle}} - 1)|\psi(t)\rangle dN(t) \end{aligned} \tag{2.46}$$

where $\hat{x} = \hat{c} + \hat{c}^\dagger$. The average rate of photodetection in this case is

$$E[dN(t)] = \mathrm{Tr}[(\varepsilon^2 + \varepsilon \hat{\mathrm{x}} + \hat{\mathrm{c}}^\dagger \hat{\mathrm{c}})\rho(\mathrm{t})]\mathrm{dt} \tag{2.47}$$

where the first term is a constant, only giving an offset to the measurement results. When $\varepsilon \gg \left\langle \hat{c}^\dagger \hat{c} \right\rangle$, the third term is ignorable. Thus the only effective term left is the second term, which indicates that the photon number detection has been converted to field quadrature measurement after adding the local oscillator in the continuum limit. This type detection is called general dyne detection, usually including homodyne detection and heterodyne detection.

In the limit of $\varepsilon \to \infty$, the Poissonian distribution turns to a Gaussian distribution and the rate of photodetection becomes

$$dN(t) = \varepsilon^2 dt[1 + \left\langle \hat{x}(t) \right\rangle / \varepsilon] + \varepsilon dW(t) \tag{2.48}$$

where dW is the white noise increment satisfying $E[dW] = 0, E[d^2W] = dt$.

The stochastic Schrödinger equation (2.46) in this continuum limit becomes

$$\begin{aligned} d\psi(t) &= (-i\hat{H} - \frac{1}{2}(\hat{c}^\dagger \hat{c} - \left\langle \hat{c}^\dagger \hat{c} \right\rangle + \left\langle x \right\rangle^2 / 4)\psi(t)dt \\ &+ (\hat{c} - \left\langle \hat{x} \right\rangle / 2)\psi(t) \end{aligned} \tag{2.49}$$

where I have used

$$\frac{1}{(1 \pm x)^m} = 1 \mp mx + \frac{m(m+1)}{2!}x^2 + ..., |x| \ll 1 \tag{2.50}$$

By using $\rho = |\psi\rangle\langle\psi|$, the normalized stochastic master equation for quantum state diffusion can be derived Wiseman and Milburn (2010)

$$d\rho(t) = -i[\hat{H}, \rho(t)]dt + dt\mathcal{D}[\hat{c}]\rho(t) + dW(t)\mathcal{H}[\hat{c}]\rho(t) \tag{2.51}$$

where ρ is the reduced density matrix of the system after tracing over the environment. The superoperator $\mathcal{H}$ is defined as

$$\mathcal{H}[\hat{r}]\rho = \hat{r}\rho + \rho\hat{r}^{\dagger} - \mathrm{Tr}[\hat{r}\rho + \rho\hat{r}^{\dagger}]\rho \tag{2.52}$$

The homodyne current is

$$J(t) = \langle\hat{x}(t)\rangle + \xi \tag{2.53}$$

where $\langle\hat{x}\rangle = \left\langle\hat{c} + \hat{c}^{\dagger}\right\rangle$ is the conditional mean of the measured quadrature of the system operator $\hat{c}$. $\xi = dW/dt$ is the Wiener process variable.

Practically in a homodyne detection, for a coherently-driven system the signal is the stationary homodyne current and for pulse-driven system the signal is an integrated homodyne current over the measurement time. In the process of signal measurement, a filter is always adopted and the filter can be linear or nonlinear. The filtered homodyne signal with a linear filter is given by

$$S = \int_0^{\infty} f(t)J(t)dt \tag{2.54}$$

where f is the response function of the filter. More linear and nonlinear protocols of the signal filtering have been discussed in Gambetta et al. (2007).

The autocorrelation of the output homodyne detection is Wiseman and Milburn (2010)

$$F^{(1)}_{hom}(t, t+\tau) = E[J(t+\tau)J(t)] = \mathrm{Tr}[\hat{\mathrm{x}}\mathrm{e}^{\mathcal{L}\tau}(\hat{\mathrm{c}}\rho + \rho\hat{\mathrm{c}}^{\dagger})] + \delta(\tau) \tag{2.55}$$

The auto-correlation function is the amplitude-amplitude correlation. It is useful in calculat-

ing the spectrum of a system and also it is an alternative way of evaluating the noise of the detected signal. Now I will give the detail derivation of how the signal variance is calculated using the first-order correlation function Eq. 2.55. Suppose that the filter is a top-hat filter, i.e., for i_{th} measurement, the signal is $S_i = \int_0^T J_i(t)dt$ and the mean value of the signal is the average over N trajectories:

$$\bar{S} = \frac{1}{N}\sum_{i=1}^{N} S_i = \frac{1}{N}\sum_{i=1}^{N}\int_0^T x_i(t)dt = \int_0^T x_{uc}(t)dt \tag{2.56}$$

here we have used $E[\xi] = 0$ and $x_{uc} = E[x]$ is the unconditional result. The variance of the signal is

$$\begin{aligned}
(\Delta S)^2 &= \frac{1}{N}\sum_{i=1}^{N}\left(S_i - \bar{S}\right)^2 \\
&= \frac{1}{N}\sum_{i=1}^{N}\left(S_i^2 - 2S_i\bar{S} + \bar{S}^2\right) \\
&= \frac{1}{N}\sum_{i=1}^{N} S_i^2 - \bar{S}^2 \\
&= \frac{1}{N}\sum_{i=1}^{N}\left(\int_0^T J_i(t)dt\right)\left(\int_0^T J_i(t')dt'\right) - \bar{S}^2 \\
&= \int_0^T dt\int_0^T dt' E[J(t)J(t')] - \bar{S}^2
\end{aligned} \tag{2.57}$$

Substituting Eq. 2.55 the first term above, we have the variance of the homodyne signal:

$$\begin{aligned}
(\Delta S)^2 &= \int_0^T dt\int_0^T dt'(u(t-t')(\mathrm{Tr}[\hat{\mathrm{x}}\exp(\mathcal{L}(\mathrm{t}-\mathrm{t}'))(\hat{\mathrm{c}}\rho(\mathrm{t}') + \rho(\mathrm{t}')\hat{\mathrm{c}}^\dagger)] \\
&+ u(t'-t)(\mathrm{Tr}[\hat{\mathrm{x}}\exp(\mathcal{L}(\mathrm{t}'-\mathrm{t}))(\hat{\mathrm{c}}\rho(\mathrm{t}) + \rho(\mathrm{t})\hat{\mathrm{c}}^\dagger)] + \delta(\mathrm{t}'-\mathrm{t})) - \bar{\mathrm{S}}^2
\end{aligned} \tag{2.58}$$

where $u(t)$ is the step function. Using the SNR definition $\mathrm{SNR} = \bar{S}/(\sqrt{(\Delta S)^2})$, the SNR can be calculated without running the stochastic simulations.

The second-order correlation or the intensity/number correlation is Wiseman and Milburn

(2010)

$$F^{(2)}(t,t+\tau) = \mathrm{Tr}[\hat{\mathrm{c}}^\dagger \hat{\mathrm{c}} \mathrm{e}^{\mathcal{L}\tau} \hat{\mathrm{c}} \rho \hat{\mathrm{c}}^\dagger] + \mathrm{Tr}[\hat{\mathrm{c}}^\dagger \hat{\mathrm{c}} \rho]\delta(\tau) \tag{2.59}$$

which is very useful to calculate $g^{(2)}$ for a field in the system.

Heterodyne detection is quite similar to homodyne detection except for a frequency offset between the local oscillator and the signal under measurement. In Heterodyne measurement two quadratures of the signal are measured simultaneously. As stated in the Heisenberg relation, one cannot measure a pair of conjugate variables simultaneously with arbitrary precision. Here, both quadratures will be measured with error probabilities. In fact, the noise of the Heterodyne detection is $\sqrt{2}$ times that in the Homodyne detection, such as the difference between the Husumi distribution and Wigner distribution in the phase space.

The stochastic master equation for Heterodyne detection is derived in Wiseman and Milburn (2010) as

$$d\rho(t) = -i[\hat{H}_s, \rho]dt + \mathcal{D}[\hat{c}]\rho dt + \sqrt{1/2}(dW_x(t)\mathcal{H}[\hat{c}] + dW_y(t)\mathcal{H}[-i\hat{c}])\rho(t) \tag{2.60}$$

There are two Heterodyne currents:

$$J_x(t) = \langle \hat{x} \rangle (t) + \sqrt{2}\xi_x(t) \tag{2.61}$$

$$J_y(t) = \langle \hat{y} \rangle (t) + \sqrt{2}\xi_y(t) \tag{2.62}$$

In Chap. 2 we will use the continuous quantum trajectory and in Chap. 3 both jump-type and continuous-type unraveling will be used for different situations. Specially, Chap. 2 will give details about calculating variance or signal-to-noise ratio (SNR) using the auto-correlation function of Homodyne currents. The examples of my PhD projects in later chapters will show that a quantum trajectory is not only a method of numerical calculation of an open system, but also corresponds to the conditional state of a system conditioned on the stochastic measurement record.

2.3.3.3 Quantum trajectory with squeezed noise

In this section, I discuss a system with a correlated noise or a system in a squeezed environment. The general form for the stochastic master equation with squeezed noise is given by Wiseman and Milburn (2010)

$$\begin{aligned} d\rho(t) &= -i[\hat{H}_s,\rho]dt + dt((\bar{n}+1)\mathcal{D}[\hat{c}]\rho + \bar{n}\mathcal{D}[\hat{a}^\dagger]\rho + \frac{\bar{m}^*}{2}[\hat{c},[\hat{c},\rho]] \\ &+ \frac{\bar{m}}{2}[\hat{c}^\dagger,[\hat{c}^\dagger,\rho]]) + dW\mathcal{H}[\frac{(\bar{n}+\bar{m}^*+1)\hat{c}-(\bar{n}+\bar{m})\hat{c}^\dagger}{\sqrt{L}}]\rho \end{aligned} \tag{2.63}$$

This formula is very useful but it is not very easy to see the physics of the terms in the equation. Here my aim is to rewrite Eq. (2.63) in a simpler and more symmetric form.

From the relation for a pure field state,

$$|\bar{m}|^2 = \bar{n}(\bar{n}+1) \tag{2.64}$$

we have

$$\begin{aligned} \frac{(\bar{n}+\bar{m}^*+1)(\bar{n}+\bar{m}^*)}{L} &= \bar{m}^* \\ \frac{(\bar{n}+\bar{m}+1)(\bar{n}+\bar{m})}{L} &= \bar{m} \\ \frac{(\bar{n}+\bar{m})(\bar{n}+\bar{m}^*)}{L} &= \bar{n} \\ \frac{(\bar{n}+\bar{m}+1)(\bar{n}+\bar{m}^*+1)}{L} &= \bar{n}+1 \end{aligned} \tag{2.65}$$

and then we can derive

$$\begin{aligned} \mathcal{D}[\frac{(\bar{n}+\bar{m}^*+1)\hat{c}-(\bar{n}+\bar{m})\hat{c}^\dagger}{\sqrt{L}}]\rho &= (\bar{n}+1)\mathcal{D}[\hat{c}]\rho + \bar{n}\mathcal{D}[\hat{a}^\dagger]\rho + \frac{\bar{m}^*}{2}[\hat{c},[\hat{c},\rho]] \\ &+ \frac{\bar{m}}{2}[\hat{c}^\dagger,[\hat{c}^\dagger,\rho]] \end{aligned} \tag{2.66}$$

Therefore we have a more symmetric and simpler form for Eq. (2.63) as:

$$d\rho(t) = -i[\hat{H}_s,\rho]dt + \mathcal{D}[\hat{c}_M]\rho dt + dW\mathcal{H}[\hat{c}_M]\rho \tag{2.67}$$

where

$$\hat{c}_M = \frac{(\bar{n} + \bar{m}^* + 1)\hat{c} - (\bar{n} + \bar{m})\hat{c}^\dagger}{\sqrt{L}} \tag{2.68}$$

The Eq. (2.67) has exactly the same mathematic form as the stochastic master equation with a vacuum noise (4.2) except the transformation $\hat{c} \to \hat{c}_M$. It indicates that no matter with a vacuum or squeezed vacuum, the relaxation of the system and the measurement on the system always act on the same system operator. Also, the transformation $\hat{c} \to \hat{c}_M$ makes the pure relaxation term $\mathcal{D}[\hat{c}]\rho$ become a term with both quadrature diffusion and relaxation $\mathcal{D}[\hat{c}_M]\rho = \frac{\bar{n}+\bar{m}}{\sqrt{L}}\mathcal{D}[\hat{c} - \hat{c}^\dagger]\rho + \frac{1}{\sqrt{L}}\mathcal{D}[\hat{c}]\rho$ (for $\bar{m} = \bar{m}^*$ case). The measurement variable in the measurement term $\mathcal{H}[\hat{c}_M]\rho$ has a certain rotating over the original one in $\mathcal{H}[\hat{c}]\rho$.

2.3.3.4 Two-level atom as example

In this subsection, we take an example of a two-level atom with relaxation for interpretation of two types of quantum trajectories discussed above. As mentioned, different unravelings of the master equation correspond to different assumptions of possible measurement setups.

A coherently driven two-level atom with the Rabi frequency Ω and the relaxation rate γ is under consideration. The lower and upper levels are respectively labeled as $|g\rangle$ and $|e\rangle$. The system Hamiltonian is given by

$$\hat{H}_s = \delta\hat{\sigma}_{ee} + \frac{\Omega}{2}(\hat{\sigma}_{ge} + \hat{\sigma}_{eg}) \tag{2.69}$$

where $\Delta = \omega_a - \omega_f$ is the detuning between the atomic transition and the driving field. The master equation governing the system is

$$\dot{\rho} = -i[\hat{H}_s, \rho] + \gamma\mathcal{D}[\hat{\sigma}_{ge}]\rho \tag{2.70}$$

Firstly, we unravel this system using a quantum jump process, in which case a direct photon counter is assumed to be utilized. The total evolution is divided into quantum jumps and

the non-Hermitian evolution between jumps. At each time step, a random number p is generated to compare with the detection rate $P_d = dt\gamma \langle \hat{\sigma}_{ee} \rangle$. If $p > P_d$, the unnormalized system state evolves as

$$d|\bar{\psi}\rangle = -i(\hat{H}_s - i\gamma/2\hat{\sigma}_{ee})\bar{\psi} \tag{2.71}$$

else, the quantum jump happens and the system state collapses to the ground state

$$|\bar{\psi}\rangle = |g\rangle. \tag{2.72}$$

The normalized wave function is $|\psi(t)\rangle = |\bar{\psi}(t)\rangle / \langle \bar{\psi}(t)|\bar{\psi(t)}\rangle$.

Secondly, we unravel this system in the quantum-state diffusion way, in which case a Homodyne detection setup is assumed for detecting the quadrature of the atomic emission. The stochastic Schrödinger equation is given by

$$d|\bar{\psi}\rangle = -i\hat{H}_s|\bar{\psi}\rangle dt - \frac{i\gamma}{2}\hat{\sigma}_{ee}dt + dW(t)\sqrt{\gamma}\hat{\sigma}_{ge}|\bar{\psi}\rangle \tag{2.73}$$

The last term is the weak continuous measurement term and $dW(t)$ is the increment of the Wiener process. Again, the normalization is required: $|\psi\rangle = |\bar{\psi}\rangle / \langle \bar{\psi}|\bar{\psi}\rangle$.

In Fig. (2.7), the simulation results for the time evolution of the excited state population from the unconditional master equation (3.26) and the quantum-jump unraveling are presented for comparison. Fig. (2.8) shows the comparison for the time evolution of the atomic polarization $\langle \hat{\sigma}_y \rangle$ using the unconditional master equation (3.26) and the quantum-state diffusion unraveling.

Now I summarize the advantages and disadvantages of these three ways in treating an open system. In terms of computational resources, the two types of stochastic wave-function unravelings are better, but they usually need averaging over many trajectories to obtain relatively accurate expectation values of system variables. The unconditional master equation gives accurate average dynamics of the open system, but with quantum noise part not included.

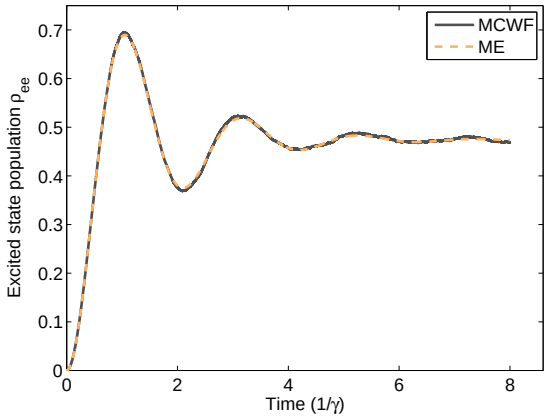

Figure 2.7 – Comparison of the time evolution of the excited state population $\langle\hat{\sigma}_{ee}\rangle$ using the master equation (dashed curve) and the Monte Carlo Wave function (solid curve) methods.

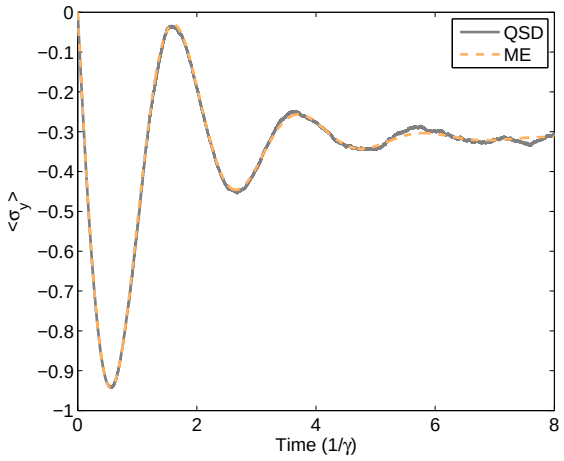

Figure 2.8 – Comparison of the time evolutions of the atomic polarization $\langle\hat{\sigma}_y\rangle$ using the master equation (dashed curve) and the quantum-state diffusion (solid curve) methods.

It is worth to note that the quantum master equation and stochastic Schrödinger/master equations are derived under two approximations, the rotating wave approximation and the Born-Markov approximation. The validity conditions for these two approximations are well known. The rotating wave approximation requires the frequency width is much smaller than the field carrier frequency or the coupling strength is smaller than the carrier frequency. The Born-Markov approximation is also called the white noise, which requires short memory and weak coupling between the system and the bath, in which case the approximate commutation relation $[\hat{b}(t), \hat{b}^{\dagger}(t')] = \delta(t - t')$ is satisfied.

2.4 Quantum non-demolition measurement

During a measurement process, according to the Heisenberg uncertainty relation, for two non-commutating operators $\hat{A}$ and $\hat{B}$, the product of the uncertainties satisfy $\Delta\hat{A}\Delta\hat{B} \geq \frac{1}{2}|\hat{A}\hat{B} - \hat{B}\hat{A}|$. Performing a precise measurement to $\hat{A}$ will lead to a large uncertainty in $\hat{B}$, which will give a back-action to $\hat{A}$ due to their coupling.

To solve this problem, the quantum non-demolition (QND) measurement Braginsky and Braginskiĭ; Braginsky and Khalili (1996) is introduced. QND measurements especially QND number measurements have been frequently applied to different applications of quantum optics Bocko and Onofrio (1996).

Suppose that there is a system observable $\hat{B}$ and one wants to perform QND measurement on $\hat{B}$ by coupling it to a meter system. To keep the variable unaffected by the interaction with the meter, a sufficient condition is

$$[\hat{B}, \hat{H}] = 0 \tag{2.74}$$

where $\hat{H}$ is the total Hamiltonian for the coupled object-meter system, including the free energy Hamiltonian of the system under detection and the meter system and the interaction between them. When the observable is conserved in absence of the interaction with the meter system, the condition (2.74) will be reduced to

$$[\hat{B}, \hat{H}_I] = 0 \tag{2.75}$$

where $\hat{H}_I$ is the interaction Hamiltonian between the system and the meter. This condition is also called the back-action evasion condition.

For the photon number or qubit-state QND measurement, two common examples are the cross Kerr nonlinearity

$$\hat{H}_I = \chi\hat{a}^\dagger\hat{a}\hat{b}^\dagger\hat{b} \tag{2.76}$$

and the dispersive field-qubit interaction

$$\hat{H}_I = \chi \hat{a}^\dagger \hat{a} (\hat{b}^\dagger + \hat{b}) \tag{2.77}$$

with $\chi = g^2/\Delta$.

In optical regime, the cross-Kerr effect has been suggested to the QND measurement of the photon number Munro et al. (2005a). Typically, with an interaction between probe and signal in a Kerr medium, $\hat{H}_I = \hbar\chi \hat{a}_s^\dagger \hat{a}_s \hat{a}_p^\dagger \hat{a}_p$, ($s$ for signal and p for probe), the probe undergoes a phase shift, which is dependent on the signal photon number.

In later chapters of this thesis, the cross-Kerr-like mechanism will be used to count single microwave photons. In the quantum circuit architecture, there is no such small scale nonlinear natural crystals or photonic crystals suitable for the GHz microwave field. Instead, a ladder-type three-level transmon simultaneously coupling with two microwaves, a probe and a signal, is used to generate strong cross-Kerr nonlinearity between the fields. In Hoi et al. (2013), it has been demonstrated experimentally that 20^o phase shift in a microwave field was induced by one average microwave photon via a transmon provided cross-Kerr nonlinearity.

2.5 Quantum theory with single-photon pulse

A system interacting with a multi-mode photon pulse is difficult to describe by analytic calculations or even numerically In the following, two approaches used in literature for dealing with single-photon pulse or Fock-state pulse will be discussed, the cascaded master equation method Gardiner and Zoller (2004) and the Fock-state master equation method Baragiola et al. (2012). Of course, there are also other methods applicable for similar circumstances, such as the formulism developed by Shanhui Fan's group Shen and Fan (2005).

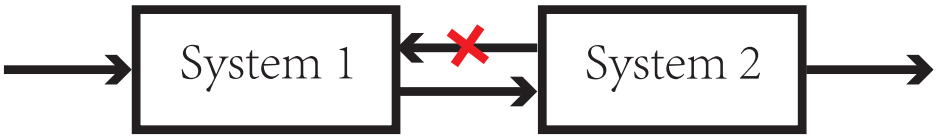

Figure 2.9 – Cascaded two quantum systems.

2.5.1 Cascaded master equation

The cascaded master equation method is usually used in the situation with irreversible coupling. More specifically, for a cascaded system with two subsystems, the output of the system 1 feeds forward to system 2 but the reverse process is not allowed. It was independently developed by Carmichael Carmichael (1993b) and Gardiner Gardiner and Zoller (2004); Gardiner (1993b). The irreversibility is realized by employing circulators and isolators, in which Farady effect plays the key role.

Following the procedure in Gardiner (1993b), I briefly reproduce the cascaded master equation. Suppose that there are two cascaded subsystems 1 and 2 and the total Hamiltonian is

$$\hat{H}_s = \hat{H}_{s1} + \hat{H}_{s2} \tag{2.78}$$

The Langevin equation for system operators are given by

$$\begin{aligned} \dot{a}_1 &= -\frac{i}{\hbar}[\hat{a}_1, \hat{H}_s] - [\hat{a}_1, \hat{c}_1^\dagger](\frac{\gamma_1}{2}\hat{c}_1 + \sqrt{\gamma_1}\hat{b}_{in}(1,t)) + (\frac{\gamma_1}{2}\hat{c}_1^\dagger + \sqrt{\gamma_1}\hat{b}_{in}^\dagger(1,t))[\hat{a}_1, \hat{c}_1] \\ \dot{a}_2 &= -\frac{i}{\hbar}[\hat{a}_2, \hat{H}_s] - [\hat{a}_2, \hat{c}_2^\dagger](\frac{\gamma_2}{2}\hat{c}_2 + \sqrt{\gamma_2}\hat{b}_{in}(2,t)) + (\frac{\gamma_2}{2}\hat{c}_2^\dagger + \sqrt{\gamma_2}\hat{b}_{in}^\dagger(2,t))[\hat{a}_2, \hat{c}_2] \end{aligned} \tag{2.79}$$

with the input-output relations:

$$\begin{aligned} \hat{b}_{out}(1,t) &= \hat{b}_{\rm in}(1,t) + \sqrt{\gamma_1}\hat{c}_1(t) \\ \hat{b}_{in}(2,t) &= \hat{b}_{\rm out}(1,t-\tau) \\ \hat{b}_{out}(2,t) &= \hat{b}_{\rm in}(2,t) + \sqrt{\gamma_2}\hat{c}_2 \end{aligned} \tag{2.80}$$

where $\hat{b}_{\rm in}(t) = \frac{1}{\sqrt{2\pi}}\int d\omega e^{-i\omega(t-t_{\rm in})}\hat{b}_{\rm in}(\omega)$ and $\hat{b}_{\rm out}(t) = \frac{1}{\sqrt{2\pi}}\int d\omega e^{-i\omega(t-t_{\rm out})}\hat{b}_{\rm out}(\omega)$.

In most experiments, the delay of light/microwave fields between the two cascaded systems is ignorably small, so that τ can be taken as 0. The total motion equation for an arbitrary system operator $\hat{a}$ is given by

$$\begin{aligned}\dot{a} &= -\frac{i}{\hbar}[\hat{a},\hat{H}_s] - [\hat{a},\hat{c}_1^\dagger](\frac{\gamma_1}{2}\hat{c}_1 + \sqrt{\gamma_1}\hat{b}_{in}(t)) + (\frac{\gamma_1}{2}\hat{c}_1^\dagger + \sqrt{\gamma}_1\hat{b}_{in}^\dagger(t))[\hat{a},\hat{c}_1] \\ &- [\hat{a},\hat{c}_2^\dagger](\frac{\gamma_1}{2}\hat{c}_1 + \sqrt{\gamma_1}\hat{b}_{in}(t)) + (\frac{\gamma_1}{2}\hat{c}_1^\dagger + \sqrt{\gamma}_1\hat{b}_{in}^\dagger(t))[\hat{a},\hat{c}_1] - [\hat{a},\hat{c}_2^\dagger]\sqrt{\gamma_1\gamma_2}\hat{c}_1 + \sqrt{\gamma_1\gamma_2}\hat{a}_1^\dagger[\hat{a},\hat{c}_2]\end{aligned} \tag{2.81}$$

Using the relation $\langle d\hat{a}(t)\rho\rangle = \langle d\hat{a}\rho(t)\rangle$, the quantum master equation for a cascaded system is given by

$$\begin{aligned}\dot{\rho} &= i[\rho,\hat{H}_s] + \gamma_1\mathcal{D}[\hat{c}_1]\rho + \gamma_2\mathcal{D}[\hat{c}_2]\rho - \sqrt{\gamma_1\gamma_2}([\hat{c}_2^\dagger,\hat{c}_1\rho] + [\rho\hat{c}_1^\dagger,\hat{c}_2]) \\ &+ \frac{\bar{n}}{2}[[\sqrt{\gamma_1}\hat{c}_1 + \sqrt{\gamma_2}\hat{c}_2,\rho],\sqrt{\gamma_1}\hat{c}_1^\dagger + \sqrt{\gamma_2}\hat{c}_2^\dagger] + \frac{\bar{n}}{2}[[\sqrt{\gamma_1}\hat{c}_1^\dagger + \sqrt{\gamma_2}\hat{c}_2^\dagger,\rho],\sqrt{\gamma_1}\hat{c}_1 + \sqrt{\gamma_2}\hat{c}_2] \\ &- [E_{in}(t)(\sqrt{\gamma_1}\hat{c}_1^\dagger + \sqrt{\gamma_2}\hat{c}_2^\dagger) - E_{in}^*(t)(\sqrt{\gamma_1}\hat{c}_1 + \sqrt{\gamma_2}\hat{c}_2),\rho]\end{aligned} \tag{2.82}$$

In the derivation I have used

$$\hat{b}_{in}(t)dt = d\hat{B}(t) + E_{in}(t)dt \tag{2.83}$$

where $E_{in}(t)$ is the coherent part of the input field to the first system and $d\hat{B}(t)$ is the quantum noise increment as defined in early this chapter.

At zero temperature and no driving case, Eq. (2.82) can be reduced to

$$\dot{\rho} = i[\hat{H}_s,\rho] + \gamma_1\mathcal{D}[\hat{c}_1]\rho + \gamma_2\mathcal{D}[\hat{c}_2]\rho - \sqrt{\gamma_1\gamma_2}([\hat{c}_2^\dagger,\hat{c}_1\rho] + [\rho\hat{c}_1^\dagger,\hat{c}_2]) \tag{2.84}$$

and it is equivalent to the another form for cascaded quantum systems derived in Carmichael (1993b):

$$\begin{aligned}\dot{\rho} &= -i[\hat{H}_s + \hat{H}_{\rm cas},\rho] + \mathcal{D}[\hat{J}]\rho \\ \hat{H}_{\rm cas} &= -i\sqrt{\gamma_1\gamma_2}/2(\hat{c}_1\hat{c}_2^\dagger - \hat{c}_1^\dagger\hat{c}_2) \\ \hat{J} &= \sqrt{\gamma_1}\hat{c}_1 + \sqrt{\gamma_2}\hat{c}_2\end{aligned} \tag{2.85}$$

This cascaded master equation (2.85) can be unraveled by using the non-Hermitian Schrödinger equation and quantum jumps. The non-Hermitian effective Hamiltonian is given by

$$\hat{H}_{\text{eff}} = \hat{H}_s + \hat{H}_{\text{eff}} - i\hat{J}^{\dagger}\hat{J}/2 \tag{2.86}$$

The unnormalized non-Hermitian Schrödinger equation between jumps is

$$d\bar{\psi}(t) = -i\hat{H}_{\text{eff}}\bar{\psi}(t)dt \tag{2.87}$$

here the zero-temperature reservoir was assumed, $\bar{N} = 0$. When there is a quantum jump,

$$\bar{\psi}(t) = \hat{J}\bar{\psi}(t) \tag{2.88}$$

For situation of cascading more than two subsystems, the general form can be presented using a general jump operator:

$$\hat{J} = \sqrt{\gamma_1}\hat{c}_1 + \sqrt{\gamma_2}\hat{c}_2 + ...\sqrt{\gamma_n}\hat{c}_n \tag{2.89}$$

The general cascaded master equation is given by

$$\frac{d\rho}{dt} = -i[\hat{H}_s + \hat{H}_{cas}, \rho] + \mathcal{D}[\hat{J}]\rho \tag{2.90}$$

with

$$\hat{H}_{\text{cas}} = -i\sum_{i,j=i+1,...n}^{n}(\sqrt{\gamma_i\gamma_j}\hat{c}_i\hat{c}_j^{\dagger} - H.c.) \tag{2.91}$$

The application of the cascaded master equation to a system with the single photon pulse is a special case, in which the first subsystem is a source cavity with a decay rate κ and with an initial state $|1\rangle$. Basically, this method is used for exponentially-decayed single photon pulses, i.e., single-photon pulse leaking from a source cavity. For Gaussion-distributed single photon source or sources with other profiles, the engineering on the source cavity decay rate might be needed, i.e., make the decay rate specially time-dependent. Fortu-

nately, single photons generated from single emitters trapped in a cavity all belong to this type and they are very promising on-demand single-photon sources for quantum information processing applications.

2.5.2 Fock-state master equation

This approach was developed in 2012 by Combes and his colleagues Baragiola et al. (2012); Gough et al. (2012). It is very powerful in treating arbitrary systems interacting multimode Fock-state photon pulses. The basic idea is to convert the situation of solving the total system master equation to the situation of solving a system using a few "reduced master equations" in the subsystem dimension without the Fock state. The number of the equations is $(N+1)^2$, where N is the Fock-state photon number. The nice thing is that the equations are not coupled with each other in a complicated way, instead, one can feed the solution of a lower level to its next upper level and solve them from the lower level to the highest level in order.

The conditions of applying this formulism are the frequency bandwidth $\delta\omega$ is much smaller than the photon pulse carrier frequency ω_c and the conditions for the rotating-wave approximation and the Born-Markov approximation. In fact, for optical photon pulses and microwave photon pulse in current experimental conditions, the first condition is usually satisfied.

Now I will give a brief review about the formulism, following Baragiola et al. (2012). Generally, a continuous-mode Fock state can be represented as

$$|N_\xi\rangle = 1/\sqrt{N}\int d\omega(\xi(\omega)\hat{a}^\dagger(\omega))^N|0\rangle \tag{2.92}$$

where ξ is the envelope function representing the shape of the Fock-state pulse. When the pulse width in the frequency domain is much narrower than the carrier frequency, the relative slow varying profile ξ can be approximately taken as independent to the carrier frequency, that is, $\xi(\omega) \approx \xi(\omega)e^{-i\omega_c t}$.

Based on this single frequency mode approximation and the Ito calculus rules, the master

equations for a system interacting with Fock states can be derived as:

$$\begin{aligned}\frac{d\rho_{m,n}}{dt} &= -i[\hat{H},\rho_{m,n}] + \mathcal{L}[\hat{L}]\rho_{m,n} + \sqrt{m}\xi(t)[\hat{S}\rho_{m-1,n},\hat{L}^\dagger] \\ &+ \sqrt{n}\xi^*(t)[\hat{L},\rho_{m,n-1}\hat{S}^\dagger] + \sqrt{mn}|\xi(t)|^2(\hat{S}\rho_{m-1,n-1}\hat{S}^\dagger - \rho_{m-1,n-1})\end{aligned} \tag{2.93}$$

with the initial conditions

$$\begin{aligned}\rho_{n,n}(0) &= \rho_{sys}(0) \\ \rho_{m,n}(0) &= \hat{0}\end{aligned} \tag{2.94}$$

where $\rho_{m,n}$ is the reduced density matrix for the system of interest in a particular Fock state basis m,n. $\hat{L}$ is a system operator linearly coupled to the Fock-state field and $\hat{S}$ is a system operator quadratically coupled to the Fock-state field. The initial condition of the off-diagonal density matrix is vacuum state, since they are not physical states.

In this formulism, the expressions for output field quantities are quite straight forward. The quadrature of the output field is given by

$$\hat{Z}_t = e^{i\phi}\hat{B}_t + e^{-i\phi}\hat{B}_t^\dagger \tag{2.95}$$

and the motion equation for the field quadrature is

$$\begin{aligned}d\hat{Z}_t^{out} &= e^{i\phi}d\hat{B}_t^{out} + e^{-i\phi}d\hat{B}_t^{\dagger out} \\ &= e^{i\phi}(\hat{L}dt + \hat{S}d\hat{B}_t) + e^{-i\phi}(\hat{L}^\dagger dt + \hat{S}^\dagger d\hat{B}_t^\dagger)\end{aligned} \tag{2.96}$$

The corresponding expectation of the motion equation is

$$\frac{dE_{m,n}[\hat{Z}]}{dt} = E_{m,n}[e^{i\phi}\hat{L} + e^{-i\phi}\hat{L}^\dagger] + e^{i\phi}\sqrt{n}\xi(t)E_{m,n-1}[\hat{S}] + e^{-i\phi}\sqrt{m}\xi^*(t)E_{m-1,n}[\hat{S}^\dagger] \tag{2.97}$$

If the single photon pulse under description is an exponentially-decayed pulse with $\xi(t) = \sqrt{\kappa}e^{-\kappa t/2}$, the Fock-state master equation is equivalent to the cascaded master equation discussed in the last subsection.

For a superposition state of different Fock states as an input field, $|\psi\rangle_{in} = c_m|m\rangle + c_n|n\rangle$ (m, n are integer), the expectation value of a system observable $\hat{A}$ needs to be averaged over a combined density matrix

$$\rho_{tot} = |c_m|^2\rho_{m,m} + c_m c_n^*\rho_{m,n} + c_m^* c_n\rho_{n,m} + |c_n|^2\rho_{n,n} \tag{2.98}$$

and

$$\left\langle \hat{A} \right\rangle = \mathrm{Tr}(\hat{\mathrm{A}}\rho_{\mathrm{tot}}) \tag{2.99}$$

For instance, for an input state $|\psi\rangle = 1/\sqrt{2}(|0\rangle + |1\rangle)$, the effective density matrix is

$$\rho_{tot} = (\rho_{0,0} + \rho_{0,1} + \rho_{1,0} + \rho_{1,1})/2; \tag{2.100}$$

One advantage of this method is that modifications are very easy to include on the input photon state, such as some time delay and arbitrary profiles, which makes it very compilable with most engineerable systems. For cascaded master equation method, if one want to change the photon wave packet distribution, some complicated engineering on a time-dependent decay rate of the source cavity will be required.

In terms of system dimension, this formulism is the same as the cascaded method. Suppose we have a Fock-state $|n\rangle$ coupled to a system with dimension $N \times N$. In the cascaded master equation, the total Hilbert space of the whole system in the cascaded master equation is $(N \times N) \times (n \times n)$ and in Fock-state ME, there are n^2 number of motion equations with dimension $N \times N$. However, as mentioned before, since the equations can be solved level by level, i.e., from $\rho_{0,0}$ to $\rho_{0,1}$ and then to $\rho_{1,1}$, the computational resource can be reduced and for not too large system, such as Fan et al. (2013), analytical solutions can be obtained.

Chapter 3

Breakdown of the cross-Kerr effect in single photon counting schemes

In the last chapter, we mentioned that QND photon number detection could be realized using a cross-Kerr nonlinearity. This chapter describes how a three-level transmon behaves like a cross-Kerr medium and how the “atomic" saturation limits the efficiency of photon detection based on the cross-Kerr nonlinearity.

3.1 Cross-Kerr nonlinearity and transmon as a cross-Kerr medium

3.1.1 Cross-Kerr nonlinearity

When an optical field is applied to a dielectric medium, an dipole moment of the medium will be induced by the electric component of the field $\vec{E}(\vec{r},t)$. This induced dipole moment is usually described by the quantity of the polarization $\vec{P}(\vec{r},t)$ (the dipole moment per unit volume). In conventional optics, the polarization is linear to the incident field amplitude $\vec{E}(\vec{r},t)$, i.e., $\vec{P}^{(1)}(\vec{r},t)=\varepsilon_0\chi^{(1)}\vec{E}(\vec{r},t)$, where $\chi^{(1)}$ is the linear susceptibility of the medium. In 1960 the invention of the laser Maiman (1960) opened a new era of nonlinear optics, in which both a linear and nonlinear response of the polarization of media will be induced by incident fields. The polarization in this case can be presented as Boyd (2003):

$$\begin{aligned}\vec{P}(\vec{r},t) &= \vec{P}^{(1)}(\vec{r},t)+\vec{P}^{(2)}(\vec{r},t)+\vec{P}^{(3)}(\vec{r},t)+... \\ &= \varepsilon_0(\chi^{(1)}\vec{E}_1(\vec{r},t)+\chi^{(2)}\vec{E}_1\vec{E}_2(\vec{r},t)+\chi^{(3)}\vec{E}_1\vec{E}_2\vec{E}_3(\vec{r},t)+...)\end{aligned} \tag{3.1}$$

where $\vec{E}_j(j = 1, 2, 3...)$ can be the same incident field or different incident fields. $\chi^{(2)}(\chi^{(3)})$ are the second-order (third-order) nonlinear susceptibility tensors. In natural materials, higher-order susceptibilities are usually much smaller than lower-order susceptibilities, i.e. $\chi^{(1)} \gg \chi^{(2)} \gg \chi^{(3)}$. It is well established that the second-order nonlinear susceptibility $\chi^{(2)}$ vanishes in centrosymmetric materials Boyd (2003) therefore the third-order polarization $\vec{P}^{(3)}$ is the dominant nonlinear response from most materials. From the microscopic point of view, i.e., consider a nonlinear medium made of two-level or three-level atoms, the cubic nonlinear polarization model is valid in the dispersive coupling regime Drummond and Walls (1980)Drummond and Walls (1981).

The cross-Kerr effect arises from the third-order nonlinear response of a medium to applied fields. It is a phenomenon that the phase of one field is changed proportional to the intensity of another field. Therefore, the cross-Kerr effect is also called the cross-phase modulation (XPM), in contrast to the self-Kerr effect or self-phase modulation (SPM).

Quantum mechanically, the cross-Kerr nonlinearity can be modeled by the interaction Hamiltonian Drummond and Walls (1980)

$$\hat{H}_{\mathrm{cK}} = \hbar\chi\hat{a}_p^\dagger\hat{a}_p\hat{a}_s^\dagger\hat{a}_s = \hbar\chi\hat{n}_p\hat{n}_s \tag{3.2}$$

where $\hat{a}_p$ ($\hat{a}_s$) are the annihilation operators for the probe (signal) fields and $\hat{n}_p$ ($\hat{n}_s$) are the corresponding number operators. The nonlinear coefficient χ is proportional to the third-order nonlinear susceptibility. Suppose that the input state is $|\Psi\rangle_{in} = |n_s\rangle|\alpha_p\rangle$, the output state after the interaction can be obtained Munro et al. (2005a)

$$|\Psi\rangle_{out} = \hat{U}|\Psi\rangle_{in} = e^{-i\chi t\hat{n}_p\hat{n}_s}|\Psi\rangle_{in} = |n_s\rangle|\alpha_p e^{-in_s\chi t}\rangle \tag{3.3}$$

where $\hat{U} = e^{-i\chi t\hat{n}_p\hat{n}_s}$ is the evolution operator. After the interaction, the Fock state (the signal field) remains the same as the input, while the probe experiences a phase shift, which is proportional to the nonlinear coefficient χ, the photon number in the signal field and the interaction time. That is why in conventional cross-Kerr nonlinearity measurements a very strong field is applied and (or) a very long cross-Kerr medium is used. The relation between cross-Kerr phase shift and the properties of fields based on Eq. 3.3 is illustrated in Figure

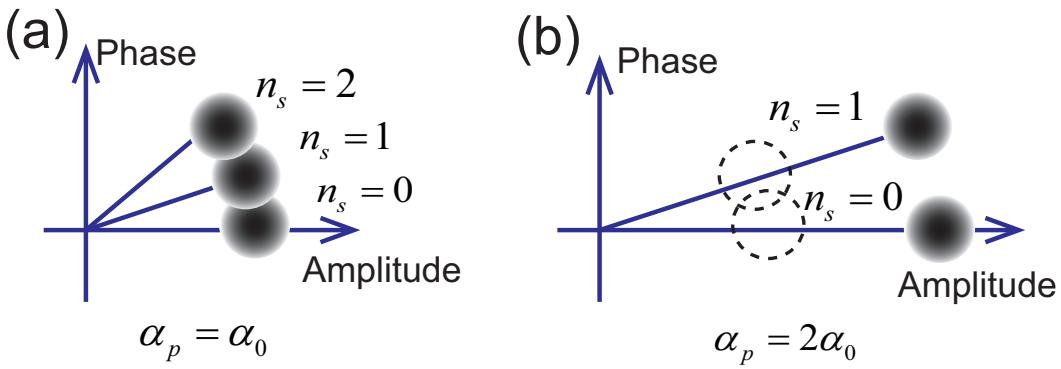

Figure 3.1 – A cartoon illustration of the cross-Kerr phase shift of a probe field induced by a signal field using the effective cross-Kerr Hamiltonian Eq.3.2. (a) The dependence of the probe phase displacement on the signal photon number; (b) The dependence of the probe phase displacement on the probe amplitude.

3.1. In Figure 3.1 (a), the dependence of the phase shift angle on the signal photon number is shown and clearly the angle increases as the signal photon number increases. Figure 3.1 (b) shows that for a certain phase shift angle and the phase displacement is linear to the probe amplitude. These conclusions from the effective Hamiltonian Eq.3.2 seem quite reasonable but in reality all nonlinear media are made of atoms and there are more issues like saturation, response times and dissipation in the interaction of fields and Kerr medium from the microscopic point of view. Later in this section, we will show that a saturation effect appears in the cross-Kerr phase shift under more realistic consideration.

In natural materials, like in optical fibers and bulk crystals, the cross-Kerr effect is very weak and difficult to observe. In recent years, it has been demonstrated that large cross-Kerr nonlinearities can be realized by preparing atomic coherences in a three-level system, four-level system Schmidt and Imamoglu (1996); Sinclair and Korolkova (2008) and five-level system Wang et al. (2006b). Moreover, the cross-Kerr phase shift at the single quantum level has been observed in the optical fiber Matsuda et al. (2009), the atomic ensemble Wang et al. (2006a) and very recently in the superconducting circuit system Hoi et al. (2013).

The cross-Kerr nonlinearity has been proposed for a variety of applications, including QND photon number measurements Imoto et al. (1985); Munro et al. (2005a), entangled state preparation Jin et al. (2007); Silberhorn et al. (2001), teleportation Vitali et al. (2000) and quantum gate Lin and Li (2009); Milburn (1989); Munro et al. (2005b); Wang et al. (2012).

Due to these important applications, the investigation of the cross-Kerr nonlinearity has been attracting more and more attention and here in this thesis I focus on its application to QND photon number detection.

3.1.2 Transmon as a cross-Kerr medium

As discussed in the last section, a three-level atomic system can be used as a cross-Kerr nonlinear medium Hoi et al. (2013); Perrella et al. (2013); Venkataraman et al. (2013). In the following I will show that, under proper conditions, a system of two fields interacting with a three-level atom can be reduced to an effective cross-Kerr interaction model of the two fields by eliminating the atomic degrees of freedom. The Hamiltonian for a three-level system coupling with two single-mode fields is given by

$$\hat{H} = \omega_2\hat{\sigma}_{22} + \omega_1\hat{\sigma}_{11} + \omega_a\hat{a}^\dagger\hat{a} + \omega_b\hat{b}^\dagger\hat{b} + g_1(\hat{a}\hat{\sigma}_{10} + \hat{a}^\dagger\hat{\sigma}_{01}) + g_2(\hat{b}\hat{\sigma}_{21} + \hat{b}^\dagger\hat{\sigma}_{12}) \tag{3.4}$$

where $\hat{a}$ and $\hat{b}$ are the annihilation operators for the fields and the energy levels of the atom is labeled as $|0\rangle$, $|1\rangle$ and $|2\rangle$. In Eq. 3.4 we have assumed $|\omega_a - \omega_{10}| \ll |\omega_a - \omega_{21}|$ and $|\omega b - \omega_{21}| \ll |\omega_b - \omega_{10}|$ and so that the coupling between the field $\hat{a}$ and the transition $1 \to 2$ and the coupling between the field $\hat{b}$ and the transition $0 \to 1$ have been neglecting as fast oscillating terms.

Since for optical and microwave fields, field frequencies is far larger than matter-field coupling coefficients, it is valid to transform the Hamiltonian 3.4 to a rotating frame as

$$\hat{H} = (\Delta_2 + \Delta_1)\hat{\sigma}_{22} + \Delta_1\hat{\sigma}_{11} + g_1(\hat{a}\hat{\sigma}_{10} + \hat{a}^\dagger\hat{\sigma}_{01}) + g_2(\hat{b}\hat{\sigma}_{21} + \hat{b}^\dagger\hat{\sigma}_{12}) \tag{3.5}$$

where $\Delta_2 = \omega_{21} - \omega_b$ and $\Delta_1 = \omega_{10} - \omega_a$. The motion equations for the system operators are

$$\frac{d\hat{a}}{dt} = -ig_1\hat{\sigma}_{01} - \frac{\kappa_1}{2}\hat{a} \tag{3.6}$$

$$\frac{d\hat{b}}{dt} = -ig_2\hat{\sigma}_{12} - \frac{\kappa_2}{2}\hat{b} \tag{3.7}$$

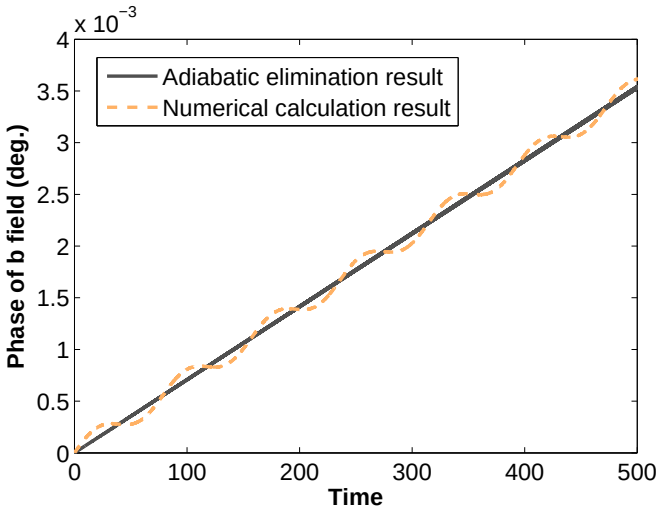

Figure 3.2 – The comparison of adiabatical elimination result and exact numerical simulation. The parameters are: $g_1 = 1$, $g_2 = 4$, $\Delta_1 = 30$ and $\Delta_2 = 200$.

$$\frac{d\hat{\sigma}_{01}}{dt} = -i\Delta_1\hat{\sigma}_{01} - ig_1\hat{a}(\hat{\sigma}_{00} - \hat{\sigma}_{11}) - ig_2\hat{b}^\dagger\hat{\sigma}_{02} \tag{3.8}$$

$$\frac{d\hat{\sigma}_{12}}{dt} = -i\Delta_2\hat{\sigma}_{12} - ig_2\hat{b}(\hat{\sigma}_{11} - \hat{\sigma}_{22}) + ig_1\hat{a}^\dagger\hat{\sigma}_{02} \tag{3.9}$$

$$\frac{d\hat{\sigma}_{02}}{dt} = -i(\Delta_1 + \Delta_2)\hat{\sigma}_{02} + ig_1\hat{a}\hat{\sigma}_{12} - ig_2\hat{b}\hat{\sigma}_{01} \tag{3.10}$$

here we have phenomenologically introduced the cavity decay rates κ_1 and κ_2.

In the dispersive regime, $\Delta_2 \gg \Delta_1, g_2$ and $\Delta_1 \gg g_1$, the atomic operators can be adiabatically eliminated by setting the time derivatives to zeros:

$$\hat{H}_{\text{eff}} = -\frac{g_1^2}{\Delta_1}\hat{a}^\dagger\hat{a} + \frac{g_1^2 g_2^2}{\Delta_1^2(\Delta_1 + \Delta_2)}\hat{b}^\dagger\hat{b}\hat{a}^\dagger\hat{a} \tag{3.11}$$

Now an effective cross-Kerr interaction between the two input fields is obtained. The test of validity of the adiabatic elimination result 3.11 is done through comparing to the exact numerical simulation of 3.4, as shown in Fig. 3.2. One can see from the figure that they well agrees with each other except fast and small-amplitude oscillations eliminated in the adiabatic elimination. This effective model is derived in the dispersive regime and under the condition of small or negligible dissipation rates of the fields and the atom. In the following I will study the model of a three-level transmon interacting with two weak coherent fields beyond the dispersive regime and show the dependence of probe displacement on the

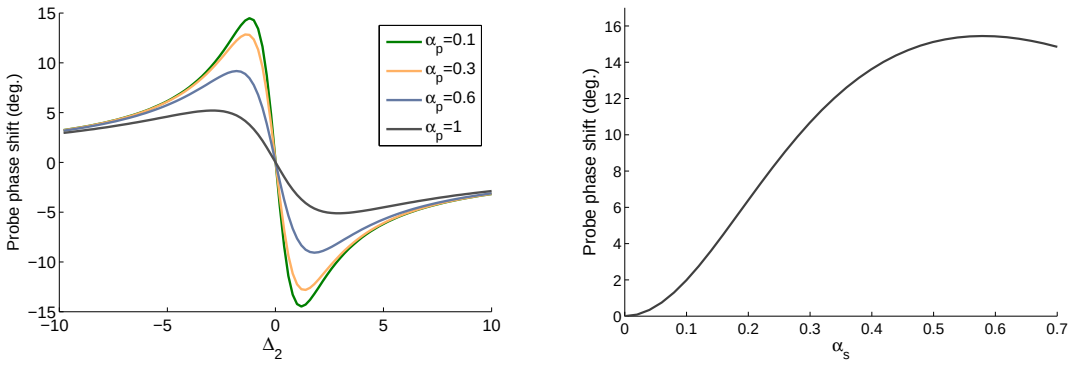

Figure 3.3 – Left:The cross-Kerr phase shift of the probe field induced by the signal field as the detuning Δ_2 is varied; Right: The cross-Kerr phase shift of the probe field induced by the signal field as the signal amplitude α_s is varied. The system parameters are: $\gamma_{01} = 1$, $\gamma_{12} = 2$, $\delta_1 = -0.01$ and $\alpha_s = 1/\sqrt{2\pi}$ for the left figure and $\alpha_p = 0.1$ and $\delta_2 = -0.8$ for the right figure.

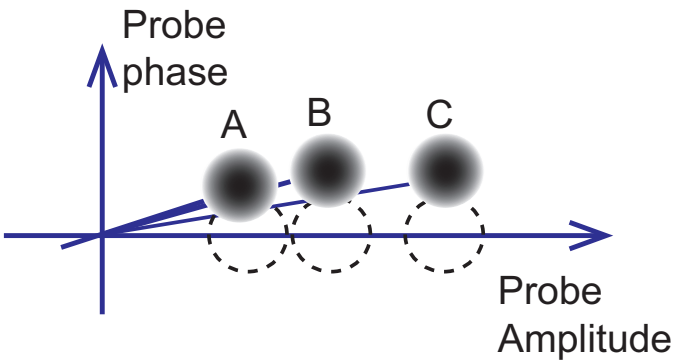

Figure 3.4 – A cartoon illustration of the saturation effect of the probe cross-Kerr phase shift induced by a fixed-amplitude signal field.

signal photon in this more realistic situation.

The system under consideration is as follows: a three-level transmon is embedded in a coplanar transmission line, with the energy levels labeled as $|0\rangle$, $|1\rangle$ and $|2\rangle$. Two weak coherent fields (probe and signal fields) are coupled to the upper and lower transitions of the transmon. This modeled has been studied experimentally in Hoi et al. (2013). The Hamiltonian for the system is given by

$$\hat{H}_s = \omega_1\hat{\sigma}_{11} + \omega_2\hat{\sigma}_{22} + g_2(\alpha_p^* e^{i\omega_p t}\hat{\sigma}_{12} + \alpha_p e^{-i\omega_p t}\hat{\sigma}_{21}) + g_1(\alpha_c^* e^{i\omega_c t}\hat{\sigma}_{01} + \alpha_c e^{-i\omega_c t}\hat{\sigma}_{10}) \quad (3.12)$$

where the coupling coefficients $g_1 = \sqrt{\gamma_{01}/2\pi}$ and $g_2 = \sqrt{\gamma_{12}/2\pi}$, with γ_{01} and γ_{12} being

the relaxation rates of the 0-1 and 1-2 transitions of the transmon, respectively. This relation between the coupling coefficient and the “atomic" relaxation rate comes from the Markovian approximation (see details in the appendix A.2).

Moving to an interaction picture at the frequencies of the driving fields and assuming that the input fields are real, the Hamiltonian becomes

$$\hat{H}_s = \Delta_1\hat{\sigma}_{11} + (\Delta_1 + \Delta_2)\hat{\sigma}_{22} + g_2\alpha_p(\hat{\sigma}_{12} + \hat{\sigma}_{21}) + g_1\alpha_c(\hat{\sigma}_{01} + \hat{\sigma}_{10}) \tag{3.13}$$

where $\Delta_1 = \omega_{10} - \omega_c$, $\Delta_2 = \omega_{21} - \omega_p$. The unconditional quantum master equation is given by

$$\dot{\rho} = -i[\hat{H}_s, \rho] + \gamma_{01}\mathcal{D}[\hat{\sigma}_{01}]\rho + \gamma_{12}\mathcal{D}[\hat{\sigma}_{12}]\rho \tag{3.14}$$

Figure 3.3 presents the phase shift of the probe induced by the signal field via the transmon provided nonlinearity. The left part of Figure 3.3 shows the probe phase shift versus the probe frequency at different probe amplitudes. There is a saturation effect of cross-Kerr effect as the probe amplitude is increased. This is because that for a certain amplitude signal field, the maximal phase displacement in the probe is limited due to the limitation in the induced “atomic" polarization. When a phase displacement is saturated, the increase in the amplitude will lead to a decrease in the phase shift angle (which is equal to the displacement over the amplitude), as illustrated in Figure 3.4. The saturation effect will be discussed more in the next section. The right part of Figure 3.3 shows that, for a low signal amplitude, there is an approximate linear relation between the phase shift and the signal amplitude. In the regime $0 < \alpha_s < 0.3$, the phase shift linearly increases as α_s increases and it can be used as a power detector of weak microwave fields.

At resonance, the analytical steady-state solution of the model above can be obtained. In

this case, the equations of motion for the expectation of the atomic operators are given by

$$\frac{d}{dt}\langle\hat{\sigma}_{00}\rangle = i\alpha_s\sqrt{\gamma_{01}}(\langle\hat{\sigma}_{01}\rangle - \langle\hat{\sigma}_{10}\rangle) + \langle\hat{\sigma}_{11}\rangle\gamma_{01} \tag{3.15}$$

$$\frac{d}{dt}\langle\hat{\sigma}_{01}\rangle = \frac{-\gamma_{01}\langle\hat{\sigma}_{01}\rangle}{2} + i\sqrt{\gamma_{01}}\alpha_s(\langle\hat{\sigma}_{00}\rangle - \langle\hat{\sigma}_{11}\rangle) + i\sqrt{\gamma_{12}}\alpha_p\langle\hat{\sigma}_{02}\rangle \tag{3.16}$$

$$\frac{d}{dt}\langle\hat{\sigma}_{02}\rangle = \frac{-\gamma_{12}}{2}\langle\hat{\sigma}_{02}\rangle - i\alpha_s\sqrt{\gamma_{01}}\langle\hat{\sigma}_{12}\rangle + i\sqrt{\gamma_{12}}\alpha_p\langle\hat{\sigma}_{01}\rangle \tag{3.17}$$

$$\frac{d}{dt}\langle\hat{\sigma}_{12}\rangle = \frac{-(\gamma_{01}+\gamma_{12})}{2}\langle\hat{\sigma}_{12}\rangle - i\sqrt{\gamma_{01}}\alpha_s\langle\hat{\sigma}_{02}\rangle + i\sqrt{\gamma_{12}}\alpha_p(\langle\hat{\sigma}_{11}\rangle - \langle\hat{\sigma}_{22}\rangle) \tag{3.18}$$

$$\frac{d}{dt}\langle\hat{\sigma}_{22}\rangle = -i\alpha_p\sqrt{\gamma_{12}}(\langle\hat{\sigma}_{12}\rangle - \langle\hat{\sigma}_{21}\rangle) - \langle\hat{\sigma}_{22}\rangle\gamma_{12} \tag{3.19}$$

For real input fields, the cross-Kerr phase displacement can be represented by $\Delta Q = -i\sqrt{\gamma_{12}}(\langle\hat{\sigma}_{12}\rangle - \langle\hat{\sigma}_{21}\rangle)$. The steady state solution for the transmon polarization $\langle\hat{\sigma}_{12}\rangle$ in the signal turn-on case is:

$$\langle\hat{\sigma}_{12}\rangle^{on} = \frac{i\alpha_s^2\sqrt{\gamma_{12}}\alpha_p\,(1+\gamma_{01}/\gamma_{12})}{\left[\left(\frac{\gamma_{01}}{2}+4\alpha_s^2\right)+2\alpha_p^2\right]\left[\left(\Gamma+2\alpha_p^2\right)/2+\alpha_s^2\gamma_{01}/\gamma_{12}\right]} \tag{3.20}$$

where $\Gamma = (\gamma_{01}+\gamma_{12})/2$. When the signal field is off, the transmon is transparent to the probe field. Thus the phase difference between the signal-on and signal-off is

$$\Delta Q \sim |\langle\hat{\sigma}_{12}\rangle^{on} - 0| \simeq \frac{\alpha_s^2\sqrt{\gamma_{12}}\alpha_p\,(1+\gamma_{01}/\gamma_{12})}{\left[\left(\frac{\gamma_{01}}{2}+4\alpha_s^2\right)+2\alpha_p^2\right]\left[\left(\Gamma+2\alpha_p^2\right)/2+\alpha_s^2\gamma_{01}/\gamma_{12}\right]} \tag{3.21}$$

At high probe intensity $\alpha \gg \xi, \gamma_2, \gamma_1$,

$$\Delta Q \sim \frac{\alpha_s^2\sqrt{\gamma_{12}}\,(1+\gamma_{01}/\gamma_{12})}{2\alpha_p^3} \tag{3.22}$$

The phase displacement is inversely proportional to cubic of the probe amplitude.

The calculations above give a picture of how a transmon acts as a cross-Kerr medium for two microwave fields. The analysis is based on assuming weak coherent fields as input fields and in the next section the cross-Kerr phase shift induced by a single microwave photon and the breakdown of cross-Kerr nonlinearity in photon counting will be discussed.

3.2 Break down of cross-Kerr effect on single photon detection

Although the cross-Kerr nonlinearity has been frequently proposed for single-photon detection and quantum computation, doubts regarding the utility of the Kerr effect in single photon applications have been raised before. Shapiro group Shapiro (2006); Shapiro and Razavi (2007) considered the multimode nature of the single photon pulse and found that there is extra phase noise compared to simple single mode calculations, leading to constraints on the achievable phase shifts. Gea-Banacloche Gea-Banacloche (2010) pointed out that it is impossible to obtain large phase shifts via the Kerr effect with single photon wave-packets. Last year, Shapiro and his colleagues suggested one could cascade many weak cross-Kerr system to achieve a large phase shift and in the same time the high state fidelity is still guaranteed. They estimated that a π phase shift can be realized by utilizing 10^6 number of units Chudzicki et al. (2013). The required large number of cascaded subsystems makes the proposal less practical. Also, none of these schemes has taken the microscopic energy structures of the cross-Kerr medium into consideration. Here we investigate a superconducting artificial three-level atom induced cross-Kerr phase shift with the inclusion of spontaneous emission and quantum noise.

Recently, superconducting circuits have become important test-beds for microwave quantum optics, demonstrating quantised fields, artificial “atoms" (i.e. with well-resolved energy levels), and strong “atom"-field interactions. The transmon is a promising superconducting artificial atom due to its insensitivity to $1/f$ noise, strong anharmonicity, and large dipole moment. Indeed, the typical size of the transmon is comparable to the dielectric gap in an on-chip microwave waveguide, and so the dipole moment is within an order of magnitude of the maximum that it can possibly be, given the geometrical constraints of the dielectric gap Devoret et al. (2007). This fact leads to very large cross-Kerr nonlinearities, where the transmon provides the non-linear polarisability. Recent experiments using a superconducting transmon in a 1D microwave transmission line have demonstrated gigantic cross-Kerr nonlinearities: a control field with on average 1 photon induces a phase shift in the probe field of 20 degrees Hoi et al. (2013). Importantly, in this experiment, the microwave fields

were freely propagating; no cavity was involved.

This large cross-Kerr phase shift immediately suggests the possibility of constructing a broadband, number-resolving, microwave-photon counter, as long as the cross-Kerr induced displacement of the probe exceeds the intrinsic quantum noise in the probe. Indeed, broadband microwave photon counting is a crucial missing piece of the experimental quantum microwave toolbox, although there are several proposals for detecting microwave photons.

In fact, the cross-Kerr interaction is strictly an effective interaction based on weak field–dipole coupling approximations. Ultimately it is mediated by the strong nonlinearities inherent in an anharmonic oscillator (e.g. an atom), so it must eventually break down. The microscopic dynamics become important in the limit of very strong coupling, which was achieved in Hoi et al. (2013). In the following the coupled field-transmon dynamics will be investigated in this limit, using proposals for microwave–photon counting as a technical objective to evaluate the validity of the cross-Kerr approximation.

3.2.1 Model

The model under consideration is as follows: two fields, a probe and a control, incident on a transmon, which is treated as a three-level, Ξ-type system in a one-dimensional transmission line. Such three-level systems are prototypes for analysing cross-Kerr nonlinearities Grangier et al. (1998). The transmon dynamics is treated exactly, including quantum noise in the incident fields. The probe is assumed to be a coherent field (or possibly squeezed), while the control field is in a Fock state, whose photon number, n, is the measurement target. Here the photon number of the Fock state is restricted to $n = 0$ or $n = 1$.

It is shown that in spite of the very large cross-Kerr nonlinearity, the induced probe displacement (i.e. the signal) in the presence of a single control photon is limited by saturation of the transmon, and is always less than the probe's own quantum noise. That is, the signal-to-noise ratio (SNR) is always below unity. Moreover, this conclusion also extends to the N-type four-level atomic level configuration, with which cross-Kerr media are often modeled Chen et al. (2006); Hu et al. (2011); Kang and Zhu (2003). These conclusions have

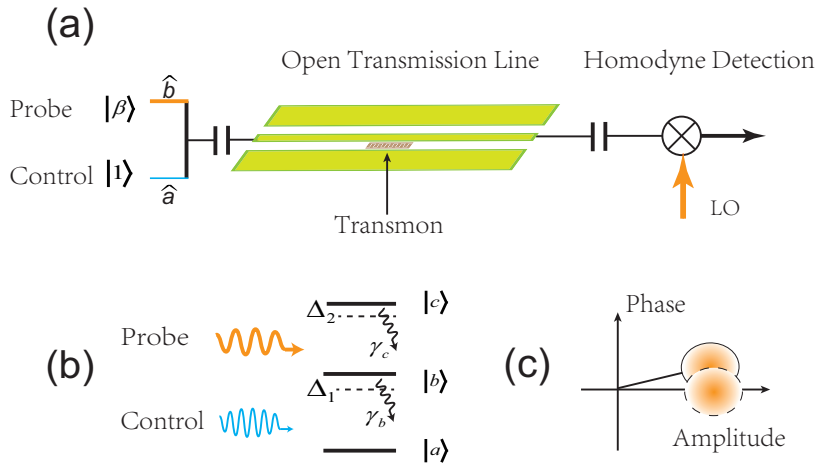

Figure 3.5 – (a) Illustrative experimental arrangement. A photon source emits a Fock state microwave photon into a 1D planar transmission line with a Ξ-type three-level transmon embedded in it. (b) Transmon level structure. The coherent probe couples $|b\rangle \leftrightarrow |c\rangle$, and the control couples $|a\rangle \leftrightarrow |b\rangle$. The interaction induced a displacement in the probe field is detected by homodyne detection. (c) Cartoon of the Kerr-induced probe displacement.

profound implications for the quantum applications of cross-Kerr phenomena.

The transmon levels are $\{|a\rangle, |b\rangle, |c\rangle\}$, with corresponding energy levels, ω_i, and decay rates, γ_i, as shown in Fig. 3.5. Relaxation between transmon energy levels is fast compared to dephasing rates, which we neglect. The probe field, $\hat{b}$, is in a coherent state $|\beta\rangle$, and is nearly resonant with the $|b\rangle \leftrightarrow |c\rangle$ transition, whilst the control field is in a Fock state of $n = 0$ or 1 photons, at a frequency ω_{con} close to the $|a\rangle \leftrightarrow |b\rangle$ transition. Qualitatively, the control field induces a transient population transfer into the state $|b\rangle$, and the probe field induces transmon polarisation, σ_{bc}, between states $|b\rangle$ and $|c\rangle$. This polarisation couples back to the probe field, so that the probe field is modified from its input state according to the standard input-output relation

$$\hat{b}_{\text{out}} = \hat{b}_{in} + \sqrt{\gamma_c}\hat{\sigma}_{bc}. \tag{3.23}$$

where $\hat{b}$ is the annihilation operator of the probe field. The homodyne detector monitoring the output probe field yields a photocurrent given by

$$J_n^{hom}(t) = \langle \hat{y}(t) \rangle + \xi(t). \tag{3.24}$$

where $\hat{y} = -i\sqrt{\gamma_c}(\hat{\sigma}_{bc} - \hat{\sigma}_{cb})$ is the transmon polarisation, $\hat{\sigma}_{ij} = |i\rangle\langle j|$ and $\xi dt = dW(t)$ is a Weiner process satisfying $E[dW] = 0$, $E[dW^2] = dt$. Here $E[X]$ represents the classical expectation value of the variable X. Finally, the useful signal is the weighted integral of the homodyne current over the lifetime, T, of the photon wave packet

$$S_n = \int_0^\infty dt\, J_n^{hom}(t) w(t) \tag{3.25}$$

where $w(t)$ is a weight function. To be more specific, $f(t)$ is chosen to be “top-hat" function, $w(t) = 1$ for $0 < t < T$, $w(t) = 0$ otherwise. I have tried other weight functions and they do not substantially change the SNR. If $n = 0$ the transmon dynamics are trivial, and $E[S_0] = 0$. For $n = 1$, $E[S_1] \neq 0$, and so S_1 represents the useful signal associated with a single photon in the control field. However, in any given measurement, the homodyne current includes quantum noise, characterised by the variance $(\sigma_{S_n})^2 = E[S_n^2] - E[S_n]^2$. To a good approximation, σ_{S_n} is independent of the photon number, n, so the signal-to-noise ratio is defined as $\mathrm{SNR} = E[S_1]/(\sqrt{2}\sigma_S)$. Note that the homodyne current will also include technical noise sources, which are ignored here and so that SNR represents the quantum limit for this scheme.

3.2.2 Cascaded master equation and Fock-state master equation methods

To study quantitatively the system consisting of a transmon interacting with propagating microwave fields, two different (but consistent) formulations are adopted, yielding both numerical and analytic results.

In the first formulation the control photon is assumed to be generated by a fictitious cavity which is initially in a Fock state. The field in the cavity decays into the 1D waveguide, and propagates to the transmon, which mediates the interaction between the control and the probe. Here the cavity is included simply as a model photon source and the transmon is outside the source cavity. To analyse this system, a stochastic cascaded master equation (SME) Gardiner and Zoller (2004) is used.

The SME describing the conditional dynamics of the cascaded cavity field–transmon density matrix, ρ, is given by

$$\begin{aligned} d\rho &= (-i[\hat{H}_s,\rho] + \gamma_{\rm con}\mathcal{D}[\hat{a}_{\rm con}]\rho + \mathcal{D}[\hat{L}_b]\rho + \mathcal{D}[\hat{L}_c]\rho)dt \\ &\quad + \sqrt{\gamma_{\rm con}}([\hat{L}_b, \rho\hat{a}^\dagger_{\rm con}] + [\hat{a}_{\rm con}\rho, \hat{L}^\dagger_b])dt + \mathcal{H}[\hat{L}_c e^{-i\pi/2}]\rho\, dW \end{aligned} \tag{3.26}$$

where $\hat{L}_b = \sqrt{\gamma_b}\hat{\sigma}_{ab}$, $\hat{L}_c = \sqrt{\gamma_c}\hat{\sigma}_{bc}$ and

$$\hat{H}_s = \Delta_c\hat{\sigma}_{cc} + \Delta_b\hat{\sigma}_{bb} + \Omega_p(\hat{\sigma}_{bc} + \hat{\sigma}_{cb}), \tag{3.27}$$

$\Delta_b = \omega_{ba} - \omega_{con}$, $\Delta_c = \Delta_p + \Delta_b$ ($\Delta_p = \omega_{bc} - \omega_p$) $\Omega_p = \sqrt{\gamma_c}\beta$, β is the amplitude of the coherent probe field, $\hat{a}_{\rm con}(\hat{a}^\dagger_{\rm con})$ are the annihilation (creation) operators for the control field and $\gamma_{\rm con}$ is the control photon linewidth. Line 2 of Eq. (3.26) describes the unidirectional evolution between the photon source and the transmon. We solve Eq. (3.26) for the conditional state of the field–transmon system, from which we compute the conditional homodyne photocurrent, using Eq. (3.24). This approach allows us to generate a simulated measurement record for ensembles of events in which $n = 0$ or 1, from which we obtain a histogram of homodyne currents to estimate the SNR.

The second formulation uses the Fock state master equation (FME) Baragiola et al. (2012), in which the propagating photon wave packet drives the transmon directly, i.e. no photon source is invoked. The transmon density matrix, $\rho_{m,n}$, acquires indices representing coherences between the transmon and photon Fock subspaces m and n. The FME is then

$$\begin{aligned} \dot{\rho}_{m,n}(t) &= -i[\hat{H}_s,\rho_{m,n}] + \mathcal{D}[\hat{L}_b]\rho_{m,n} + \mathcal{D}[\hat{L}_c]\rho_{m,n} \\ &\quad + \sqrt{n}f^*(t)[\hat{L}_b, \rho_{m,n-1}] + \sqrt{m}f(t)[\rho_{m-1,n}, \hat{L}^\dagger_b] \end{aligned} \tag{3.28}$$

where $f(t)$ is a complex valued probability amplitude that determines the photon counting rate, $|f(t)|^2$. We first solve the dynamics for $\rho_{0,0}(t)$, which drives $\rho_{0,1}(t)$ and $\rho_{1,0}(t)$, which in turn drives $\rho_{1,1}(t)$. Then, using the quantum regression theorem Lax (1963), we calculate the SNR analytically (details see the appendix A.1).

To test the consistence of these two formulations, in Fig. 3.6, the results for $\langle\hat{y}(t)\rangle$ from

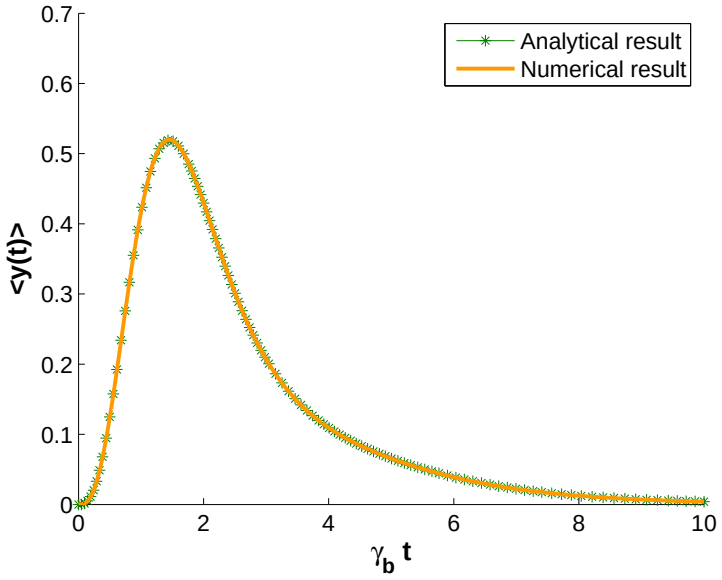

Figure 3.6 – The time evolution of the transmon polarisation: comparison between analytical and numerical results. The parameters are: $\gamma_c = 2\gamma_b, \gamma_{\rm con} = \gamma_b, \Delta_c = \Delta_b = 0, \beta = \gamma_b$.

solutions of them are presented for comparison. The green curve represents the result from the analytical solution of the Fock-state master equation and the orange curve represents the result from the numerical solution for the cascaded master equation. It is clear that there is a perfect agreement between these two methods.

Now we turn to investigate the system dynamics with different pulse shapes. If the photon is derived from exponential (E) decay of a cavity mode, then $f(t) = \sqrt{\gamma_{\rm con}}\exp(-\gamma_{\rm con}t/2)$. Further, this method can handle arbitrary photon wave packets, and we include Gaussian (G) and rectangular (R), shown in Fig. 3.7(top), where $T = 1/\gamma_{\rm con}$ is the pulse's temporal width. The photon induces a polarisation, $\langle\hat{y}(t)\rangle$, in the transmon, shown in Fig. 3.7(bottom). Different pulse shapes yield modest differences in $\langle\hat{y}(t)\rangle$.

Fig. 3.8 shows the SNR as a function of the probe amplitude with detunings and $\gamma_{\rm con}$ optimised. The points represents 5000 trajectories of the SME, whilst the solid line is computed from the FME, showing good agreement. The inset shows histograms of stochastic calculations of the integrated homodyne current with $n = 0$ and $n = 1$ (using parameters that optimises the SNR). Figure 3.9 shows SNR versus the detunings Δ_b and Δ_c. Clearly, the optimal SNR is located at $\Delta_b = \Delta_c = 0$. Moreover, the effect of varying the ratio γ_c/γ_b has

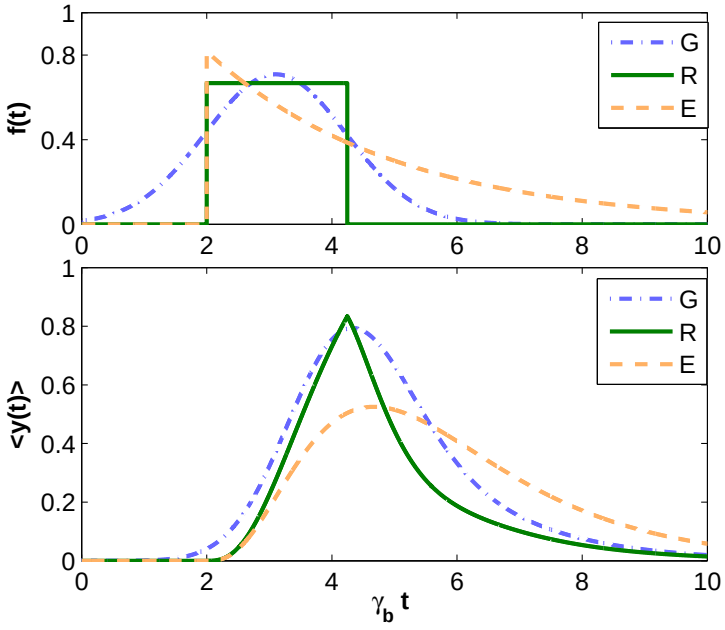

Figure 3.7 – The transmon responses for different control field wave packets. (top) blue dot-dashed curve: Gaussian pulse (G); Green solid curve: rectangular pulse (R); Orange dashed curve: Exponentially-decayed pulse (E); and (bottom) the corresponding polarisation response of the transmon. The parameters are: $\Delta_c = \Delta_b = 0, \gamma_{\rm con} = 0.6672\gamma_b, \gamma_c = 2\gamma_b, \beta = 0.4\gamma_b(E); 0.47\gamma_b(R); 0.59\gamma_b(G)$.

.

also been studied, as plotted in Fig. 3.10. It is shown that the SNR saturates from $\gamma_c/\gamma_b = 2$ and the SNR is below unity for $1 < \gamma_c/\gamma_b < 20$.

Regardless of parameter settings the SNR is less than unity, so we conclude it is impossible to reliably distinguish between $n = 0$ and 1 in a single shot. This is borne out by the large overlap of the histograms.

The fact that SNR< 1 can be understood in the following way: a single control photon induces a variation in the transmon polarisation $\hat{y}$, which manifests as a fluctuation in the homodyne current according to Eq. (3.24). However the polarisation of the transmon is a bounded operator: $||\hat{y}|| \leq \sqrt{\gamma}_b$. The optimal photon wave packet width is $T \sim \gamma_b^{-1}$ (any shorter and the transmon cannot respond to the field; any longer and vacuum noise in the homodyne signal grows), so the expected signal is bounded by $|E[S_1]| \leq \int_0^T dt\, ||\hat{y}|| \leq \gamma_b^{-1/2}$. Quantum noise in Eq. (3.24) gives $\sigma_S^2 \geq \mathrm{var}[\int_0^T dt\, \xi] = \gamma_b^{-1}$ so we see that $\mathrm{SNR} = |E[S_1]|/\sigma_S \leq 1$. Fig. 3.8 bears out this analysis: for small probe field amplitudes, the SNR

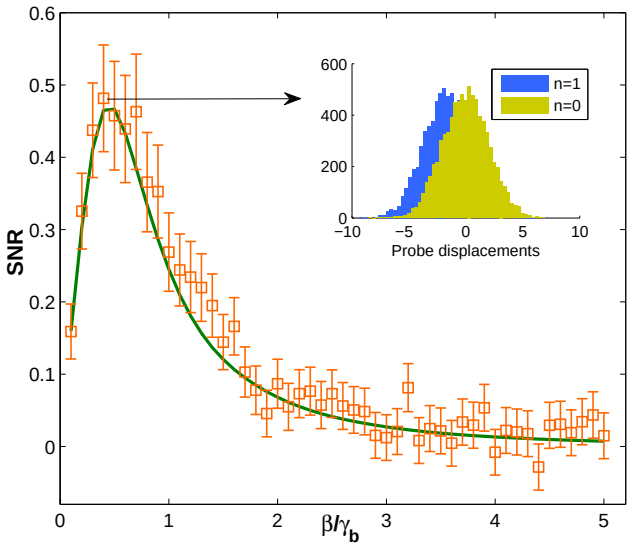

Figure 3.8 – The SNR as a function of the probe amplitude β at optimal parameter setting. The orange square represents the numerical SNR from the SME and the green curve represents the analytical SNR from the FME. The inset is a histogram of measurement outcomes, with parameters chosen to maximize the SNR.

increases, however the transmon dynamics eventually saturates at large amplitudes.

This argument suggests that the fundamental problem is the saturation of the transmon transition. It may be thought that this can addressed by increasing the number of transmons. We therefore briefly consider a system of N transmons, arranged such that the spacing between adjacent transmons is much smaller than the wavelength, the transmons are described by the collective atomic spin operators

$$\hat{S}_{ij} = \frac{1}{\sqrt{N}} \sum_k \sigma_{ij}^k \tag{3.29}$$

The stochastic master equation describing the N-transmon system is given by

$$\begin{aligned} d\rho &= -i[\hat{H}_s, \rho]dt + \gamma_{\text{con}}\mathcal{D}[\hat{a}_{\text{con}}]\rho dt + N\gamma_b\mathcal{D}[\hat{S}_{ab}]\rho dt + N\gamma_c\mathcal{D}[\hat{S}_{bc}]\rho dt \\ &- \sqrt{N\gamma_{\text{con}}\gamma_b}([\hat{S}_{ba}, \hat{a}_c\rho] + [\rho\hat{a}_c^\dagger, \hat{S}_{ab}])dt + \sqrt{N\gamma_c}\mathcal{H}[\hat{S}_{bc}e^{-i\pi/2}]\rho dW \end{aligned} \tag{3.30}$$

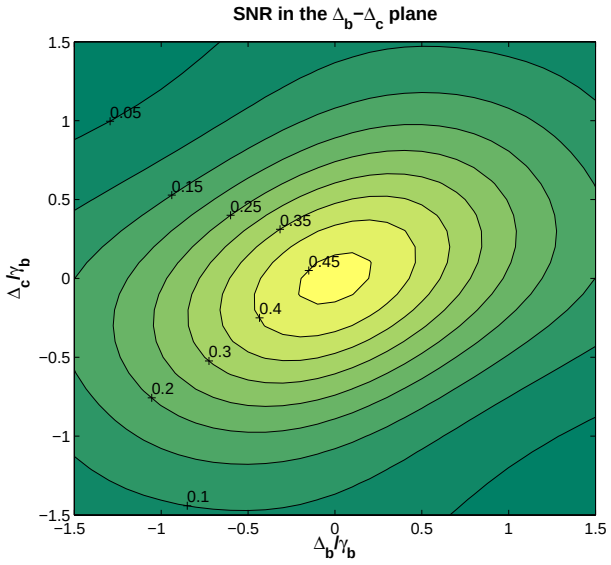

Figure 3.9 – The SNR of the probe field as functions of detunings Δ_b and Δ_c. The other parameters are: $\gamma_c = 2\gamma_b$, $\gamma_{\rm con} = 0.6772\gamma_b$, $\beta = 0.4\gamma_b$.

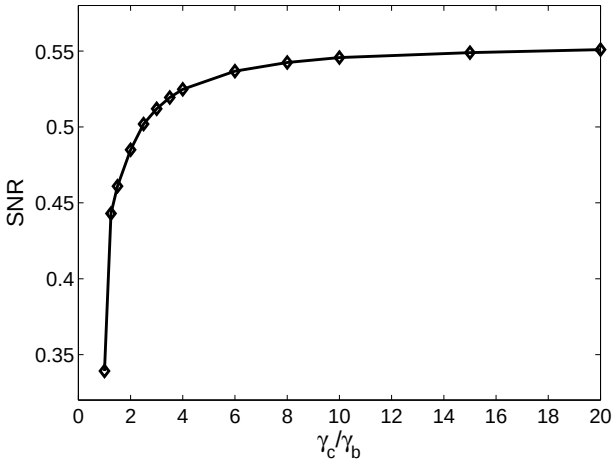

Figure 3.10 – The SNR as a function of the ratio γ_c/γ_b. The parameters are: $\gamma_{\rm con} = 0.6672\gamma_b, \beta = 0.4\gamma_b, \Delta_c = \Delta_b = 0$.

where

$$\hat{H}_s = N(\Delta_c \hat{S}_{cc} + \Delta_b \hat{S}_b) + \sqrt{N\gamma_c}\beta(\hat{S}_{bc} + \hat{S}_{cb}) \tag{3.31}$$

It is seen that the ensemble master equation (3.31) is the same form as the single-transmon master equation, albeit with decay rates and energies scaled by an N-dependent factor, leading to faster dynamics. This merely rescales the parameters in the problem, so cannot increase the SNR above the optimised single transmon case.

It is worth commenting on a number of other avenues that have been explored, but which yield similar negative results. In the following subsections, they will be discussed one by one.

3.2.3 Detection with a squeezed noise

Squeezing has been extensively used to suppress quantum vacuum noise in quantum metrology. Nevertheless, limited by the Heisenberg uncertainty relation, one can not achieve extremely good performances even using very high degree of squeezing, as discussed in Yonezawa et al. (2012). Even though, it can yet be regarded as a good tool in reducing the noise of detected quadrature when a suitable degree of squeezing is chosen.

Squeezing the probe field in an appropriate quadrature reduces the Homodyne noise, and may improve the SNR. Since we are monitoring the phase displacement of the probe field, we should squeeze in this quadrature. However this enhances noise in the conjugate, amplitude quadrature. The additional noise in the probe amplitude adds noise to the transmon dynamics arising from fluctuations in Ω_p, which ultimately feed through to the output field. We find numerically that these tradeoffs yield no net improvement in the SNR.

The stochastic master equation in a squeezed vacuum is given by

$$\begin{aligned} d\rho &= (-i[H_s, \rho] + \gamma_{\rm con}\mathcal{D}[\hat{a}_{\rm con}]\rho + \mathcal{D}[\hat{b}]\rho - \sqrt{\gamma_{\rm con}}([\hat{L}_b^\dagger, \hat{a}_{\rm con}\rho] + [\rho\hat{a}_{\rm con}^\dagger, \hat{L}_b]) \\ &+ \mathcal{D}[\hat{c}_m] + \mathcal{H}[\hat{c}_m]\rho dW \end{aligned} \tag{3.32}$$

where

$$\begin{aligned} H_s &= \Delta_c \hat{\sigma}_{cc} + \Delta_b \hat{\sigma}_{bb} + \sqrt{\gamma_c} \int d\nu \beta_\nu (\hat{\sigma}_{bc} + \hat{\sigma}_{cb}) \\ \hat{c}_m &= (-i(\bar{n} + \bar{m} + 1)\hat{L}_c + i(\bar{n} + \bar{m}^*)\hat{L}_c^\dagger)/\sqrt{L} \end{aligned} \tag{3.33}$$

with $\bar{n} = \sinh(r)\cosh(r)e^{i\theta}$, $\bar{n} = \sinh^2(r)$ and $L = 1 + 2\bar{n} + \bar{m} + \bar{m}^*$. The instantaneous photocurrent is

$$I_c^{hom}(t) = \langle \hat{y} \rangle_c (t) + \sqrt{L}\xi(t) \tag{3.34}$$

This equation indicates that the noise term ξ is multiplied by a factor of $\sqrt{L}$. Notice that when θ is chosen as zero, $L = e^{-2r}$ and the noise is reduced while when $\theta = \pi$, the noise is amplified.

The left part of Fig. 3.11 shows the histograms of the integrated Homodyne signals for the situation of 2 dB squeezed vacuum environment. A clear but not significant improvement is seen compared to the histograms in the inset of Fig. 3.8. In the right part of Fig. 3.11, the SNR varies as the squeezing in the phase quadrature increases and there is optimal squeezing as expected. According to uncertainty relation the phase squeezing indicates an amplification of the amplitude noise, which results in larger dynamical noise in the atomic response.

3.2.4 Cascaded multiple transmons

Secondly, if the control photon interacts sequentially with M transmons in series, each with independent probes, the overall SNR would be increased by a factor of $M^{1/2}$. However, the Kramers-Kronig relations require that a large phase shift implies a large reflection probability, so that there is a tradeoff between the phase shift versus reflection probability at each transmon. Again, the numerics shows that the tradeoff yields no net improvement in SNR.

To determine the maximal number of transmons one can cascade, firstly the transmission rate of the signal field after passing one transmon will be evaluated. As is known that in low dimensional systems photons will be reflected completely by qubits on resonance Shen

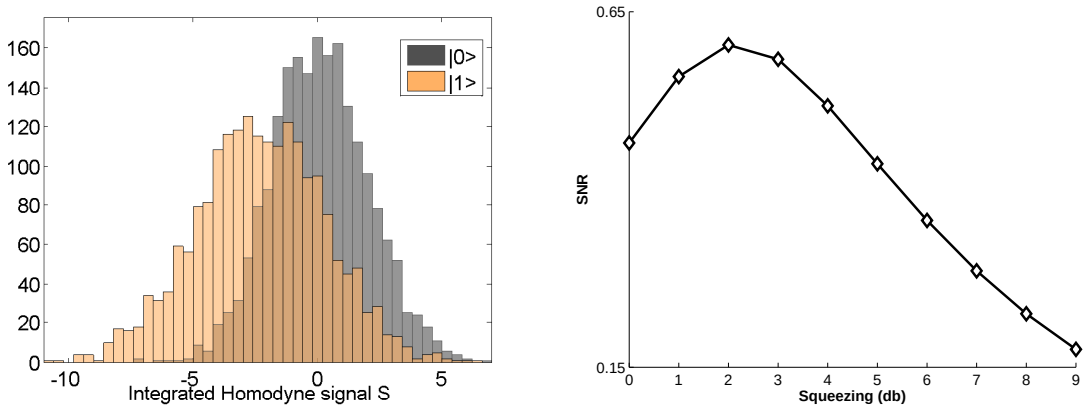

Figure 3.11 – Left: The histograms of the Homodyne signal in the presence/absence of the single photon with $2\mathrm{dB}$ squeezed vacuum environment. Right: The SNR as a function of the squeezing degree (dB); The parameters are: $\gamma_c = 2\gamma_b, \gamma_{\mathrm{con}} = 0.6672\gamma_b, \beta = 0.4\gamma_b, \Delta_c = \Delta_b = 0$.

and Fan (2005). On the other hand, EIT-like effects appear when there are more energy levels Shen and Fan (2009). In this three-level structure, two-pathway interference forms and the familiar EIT-like transparency window appears, shown in Fig. 3.12. However, how wide is the window and whether the parameters for this transparency window is consistent with those at best SNR are questions. The calculation of the transmission rate by the similar procedure in Shen and Fan (2005) will be shown in the following.

The cascaded system is equivalent to the model of transmons interacting with a single photon pulse centered at ω_c and a coherent field in the transmission line directly. After linearizing the dispersion in the vicinity of ω_c and formally adding the non-Hermitian damping terms (which come from the Markovian approximation by tracing out the bath operators), the Hamiltonian in the real space can be written as

$$\begin{aligned} H &= \int dx[\hat{a}_R^\dagger(x)(\omega_c - iv_g\frac{\partial}{\partial x})\hat{a}_R(x) \\ &+ \hat{a}_L^\dagger(x)(\omega_c + iv_g\frac{\partial}{\partial x})\hat{a}_L(x)] + (\omega_c - \omega_p - i\gamma_c/2)\hat{\sigma}_{cc} \\ &+ (\omega_b - i\gamma_b/2)\hat{\sigma}_{bb} + \int dx\sqrt{\gamma_b}\delta(x)[\hat{a}_R^\dagger\hat{\sigma}_{ab} + \hat{\sigma}_{ba}\hat{a}_R \\ &+ \hat{a}_L^\dagger\hat{\sigma}_{ab} + \hat{\sigma}_{ba}\hat{a}_L] + \sqrt{\gamma_c}\alpha(\hat{\sigma}_{bc} + \hat{\sigma}_{cb}) \end{aligned} \tag{3.35}$$

where v_g is the group velocity of the signal photon, which depends on the geometry and

material of the waveguide. For a typical coplanar waveguide of quantum circuit system, $v_g = \frac{1}{\sqrt{C'L'}} = \frac{1}{C'Z_0} = c/\sqrt{\epsilon_{\text{eff}}}$ with the effective permittivity ϵ_{eff} around 5.9. The time-independent eigen-equation is

$$H\left|E_k\right\rangle = E_k\left|E_k\right\rangle \tag{3.36}$$

with $E_k = \omega = \omega_c + v_g k_R$ and

$$\begin{aligned} \left|E_k\right\rangle &= \int dx\phi_R\hat{a}_R^\dagger(x)\left|0_R, 0_L, a\right\rangle + \int dx\phi_L\hat{a}_L^\dagger\left|0_R, 0_L, a\right\rangle \\ &+ c_1\left|0_R, 0_L, b\right\rangle + c_2\left|0_R, 0_L, c\right\rangle \end{aligned} \tag{3.37}$$

Then the equations for the coefficients can be obtained:

$$\begin{aligned} (\omega_{con} - iv_g)\frac{\partial}{\partial x}\phi_R + g_1\delta(x)c_1 &= \omega\phi_R \\ (\omega_{con} + iv_g)\frac{\partial}{\partial x}\phi_L + \alpha\delta(x)c_1 &= \omega\phi_L \\ (\omega_b - i\gamma_c/2)c_1 + \sqrt{\gamma_b}(\phi_R(0) + \phi_L(0)) + \sqrt{\gamma_c}c_2\alpha &= \omega c_1 \\ (\omega_c - i\gamma_c/2 - \omega_p)c_2 + \sqrt{\gamma_c}c_1\alpha &= \omega c_2 \end{aligned} \tag{3.38}$$

where

$$\begin{aligned} \phi_R &= \exp(ikx)\theta(-x) + t\exp(ikx)\theta(x) \\ \phi_L &= r\exp(-ikx)\theta(-x) \end{aligned} \tag{3.39}$$

with $\theta(x)$ being the Heaviside step function.

By solving the equations above, the transmission amplitude can be obtained;

$$t = \frac{(\Delta_b' + i\sqrt{\gamma_c}/2)(\Delta_c' + i\gamma_c/2) - \gamma_c\alpha^2}{(\Delta_b' + i\gamma_c/2 + i\gamma_b/vg)(\Delta_c' + i\gamma_c/2) - \gamma_c\alpha^2} \tag{3.40}$$

where $\Delta_b' = \omega_b - \omega$ and $\Delta_c' = \omega_c - \omega_p - \omega$. Here the frequency width of the signal photon

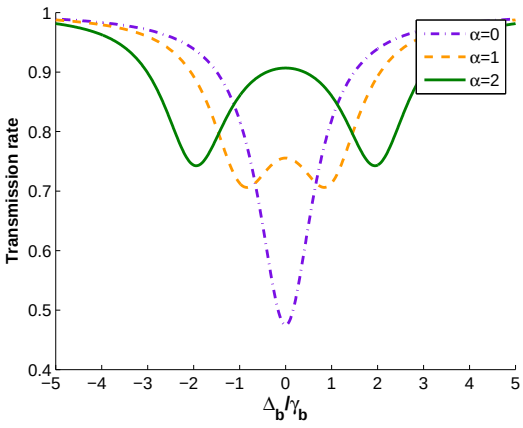

Figure 3.12 – Electromagnetic induced transparency in a three-level transmon for different field amplitudes.

is much smaller than its central frequency, that is to say, it is a relatively narrow pulse, therefore in the the following we use Δ_b and Δ_c to replace Δ_b' and Δ_c'.

From Fig. 3.12, an induced transparency window appears as expected, which is caused by the two-channel interference between transmon transitions. The width of window is twice of the coupling $\sqrt{\gamma_c}\alpha$. One can find that to achieve a high transmission rate, either large α or large Δ_b is required. This indicates that a large transmission rate corresponds a low SNR.

Now a system with cascaded n transmons with separate probes and detectors is considered, as shown in the left part of Fig. 3.13. Ideally it is equivalent to average over n trajectories. However, after including the reflection, the effective SNR_n becomes (high order terms $o(R)$ are omitted here):

$$\mathrm{SNR}_n = \mathrm{SNR}_1(\sqrt{n}\mathcal{T}^{n-1} + \sum_{j=1}^{n-1} j/\sqrt{n}\mathcal{T}^{j-1}\mathcal{R}) \tag{3.41}$$

where $\mathcal{T} = |t|^2$ and $\mathcal{R} = 1 - \mathcal{T}$ are the transmission and reflection rates of the photon, respectively. SNR_1 is the SNR in one transmon and one probe case. After optimizing parameters, the SNR as a function of probe number is plotted in the right part of Fig. 3.13. Obviously, the signal can not win the noise by cascading multiple transmons.

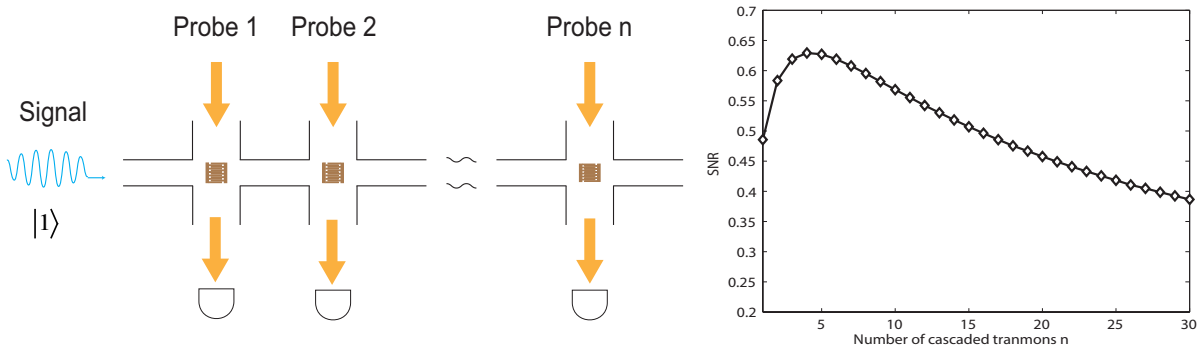

Figure 3.13 – Left: The schematic for microwave photon counting using cascaded n transmons; Right: The SNR as a function of the transmon number n.

3.2.5 Conversion from N-type Four-level structure to ladder-type three-level structure

Thirdly, some schemes for inducing cross-Kerr nonlinearities in optical systems use an N-type four-level system Schmidt and Imamoglu (1996); Sinclair and Korolkova (2008), with a strong classical field addressing the intermediate transition. In the limit of strong driving, this maps onto the same three-level structure we consider in this work, so the conclusions we have reached here also apply to such N-type systems The N-type four-level structure has been suggested to be a promising candidate for implementing cross-Kerr nonlinearity. This subsection will show that a N-type four-level system can be approximately mapped to a three-level ladder system.

The Hamiltonian for a four-level system coupling with a signal field β at transition 0-1, a control field β at transition 1-2 and a probe α at transition 2-3 in a rotating frame is given by

$$\begin{aligned} H &= (\Delta_{10}-\Delta_{12})\hat{\sigma}_{00}+\Delta_{12}\hat{\sigma}_{11}+\Delta_{32}\hat{\sigma}_{33} \\ &+ \sqrt{\gamma_{01}}\beta(\hat{\sigma}_{10}+\hat{\sigma}_{01})+\frac{\Omega}{2}(\hat{\sigma}_{12}+\hat{\sigma}_{21})+\sqrt{\gamma}_{32}\alpha(\hat{\sigma}_{23}+\hat{\sigma}_{32}) \end{aligned} \tag{3.42}$$

When the transition 1-2 is strongly driven by Ω, the subsystem of the transition 1-2 and the control field can be diagonalized independently. Defining a unitary transformation U as

$$\begin{pmatrix} \cos\theta & -\sin\theta \\ \sin\theta & \cos\theta \end{pmatrix}, \tag{3.43}$$

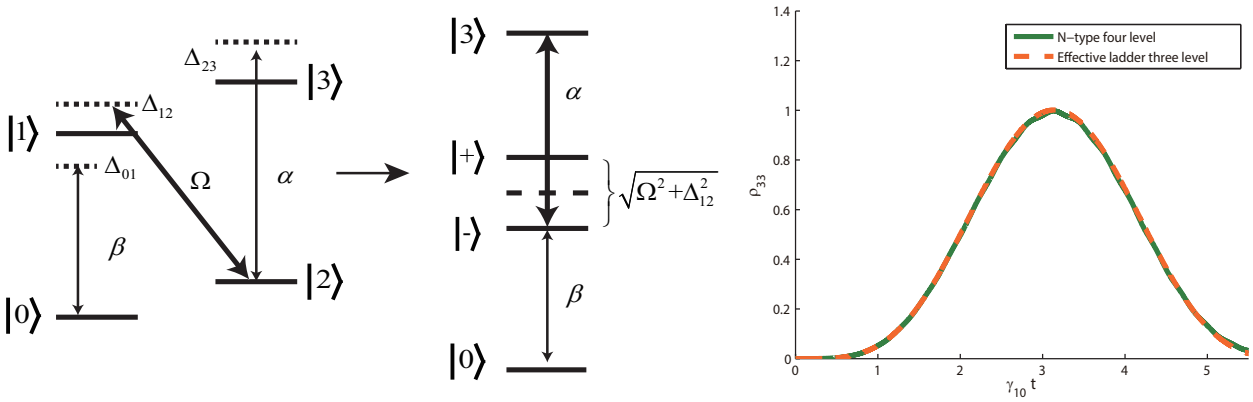

Figure 3.14 – Left: Illustration of the conversion from an N-type four-level system to a ladder-type three-level system; Right: The comparison of the population of the excited state $|3\rangle$ in the two configurations. The parameters are $\Delta_{12} = 0$, $\Delta_{10} = \Delta_{32} = \lambda_-$, $\Omega = 10\gamma_{10}$, and $\alpha = \beta = \gamma_{12} = \gamma_{32} = \gamma_{10}$

The system Hamiltonian of the 1-2 transition and the field $H_{12} = \Delta_{12}\hat{\sigma}_{11} + \frac{\Omega}{2}(\hat{\sigma}_{12} + \hat{\sigma}_{21})$ can be diagonalized by performing the transformation Ω,$U^\dagger H_{12} U$ and θ can be solved as:

$$\theta = \frac{1}{2}\arctan(\Omega/\Delta_{12}) \tag{3.44}$$

and the states $|1\rangle$, $|2\rangle$ can be represented in the dressed states $|-\rangle$ and $|+\rangle$Cohen-Tannoudji and Reynaud (1977):

$$\begin{aligned} |1\rangle &= \cos\theta\,|-\rangle - \sin\theta\,|+\rangle \\ |2\rangle &= \cos\theta\,|+\rangle + \sin\theta\,|-\rangle \end{aligned} \tag{3.45}$$

Then the Hamiltonian can be rewritten as

$$\begin{aligned} H &= -\Delta_{10}\hat{\sigma}_{00} + \Delta_{32}\hat{\sigma}_{33} + \lambda_+\hat{\sigma}_{++} + \lambda_-\hat{\sigma}_{--} \\ &+ \sqrt{\gamma_{01}}\beta(\cos\theta(\hat{\sigma}_{-0} + \hat{\sigma}_{0-}) - \sin\theta(\hat{\sigma}_{+0} + \hat{\sigma}_{0+})) \\ &+ \sqrt{\gamma}_{32}\alpha(\cos\theta(\hat{\sigma}_{+3} + \hat{\sigma}_{3+}) + \sin\theta(\hat{\sigma}_{-3} + \hat{\sigma}_{3-})) \end{aligned} \tag{3.46}$$

where $\lambda_\pm = \frac{1}{2}\Delta_{12} \pm \frac{1}{2}\sqrt{\Delta_{12}^2 + \Omega^2}$.

It is assumed that the signal field and probe field are tuned to be resonant with the state $|-\rangle$, that is, $\Delta_{10} = \lambda_-$ and $\Delta_{32} = \lambda_-$. We perform a rotating and ignore the fast-varying

terms like $e^{i\sqrt{\Delta_{12}^2+\Omega^2}t}$, then an approximate three-level system is obtained:

$$\hat{H} = \cos\theta\sqrt{\gamma_{01}}\beta(\hat{\sigma}_{-0} + \hat{\sigma}_{0-}) + \sin\theta\sqrt{\gamma_{32}}\alpha(\hat{\sigma}_{-3} + \hat{\sigma}_{3-}) \tag{3.47}$$

As shown in Fig. 3.14, it is a good approximation when there is a strong driving ($\Omega \gg \gamma_{01}, \alpha, \beta$) at the dressed transition.

3.3 Conclusion

A number of proposals suggest using weak Kerr media to build controlled phase and C-NOT gates with fewer resources than linear optical schemes Munro et al. (2005b); Nemoto and Munro (2004). In these schemes the cross-Kerr phase shift per photon is much less than π, so a strong coherent bus compensates for the weak nonlinearity, such that the small cross-Kerr phase shift manifests as a large displacement of the strong coherent field. However the saturation of the cross-Kerr effect described above indicates that once the displacement of the strong coherent field approaches its own quantum noise, saturation effects lead to the breakdown of the effective cross-Kerr description, rendering such protocols ineffective.

This chapter focused on the investigation of the feasibility of microwave photon-counting based on an induced cross-Kerr nonlinearity arising from coupling to a large anharmonic dipole. The conclusion is that the saturation of the transmon transition limits the SNR to less than unity. As such, it is not possible to use strong, atom-induced cross-Kerr nonlinearities to perform single photon detection. This conclusion applies to a number of extensions of the basic model, including multiple transmons, cascaded transmons and N-type, four-level system. Further, it limits the applicability of any proposal that requires a cross-Kerr nonlinearity to produce a displacement of a coherent field by an amount greater than the intrinsic quantum noise in the coherent field: it is precisely this condition where the effective cross-Kerr description breaks down, and saturation effects become dominant.

Chapter 4

Non-absorbing high-efficiency detector for single microwave photons

The last chapter has shown that it is impossible to efficiently detect single microwave photons using the nonlinearity provided by a three-level transmon in an open transmission line, due to the saturation of transmon responses to the probe amplitude. In this chapter, an improved scheme is proposed to overcome the difficulty in the preceding work and a high-efficiency non-absorbing microwave photon counter is presented. Moreover, the measurement induced back-action including pulse distortion and decoherence will be also discussed in details.

4.1 Single microwave photon detection using one transmon

Since the early theoretical work on photodetection Glauber (1963a); Mandel et al. (1964) both theory and technology have advanced dramatically. Conventional photon detectors, such as avalanche photodiodes (APDs) and photomultiplier tubes (PMTs), are widely used in practice. However, they destroy the signal photon during detection. There are a number of schemes for quantum non-demolition (QND) optical photon detection Helmer et al. (2009); Munro et al. (2005a); Reiserer et al. (2013) but typically they require a high-Q cavity for storing the signal mode containing the photon(s) to be detected, and a leaky cavity for manipulating and detecting the probe mode via weak nonlinear interaction with the signal cavity. Thus, during one lifetime of a signal photon, the probe mode undergoes many cycles to accumulate information about the signal. This type of detection requires multiple

measurements and the high-Q cavity limits the photodetection bandwidth. In the microwave regime the detection of single photons Chen et al. (2011); Gleyzes et al. (2007); Govia et al. (2012); Johnson et al. (2010); Peaudecerf et al. (2014); Peropadre et al. (2011); Poudel et al. (2012); Romero et al. (2009a,b); Sathyamoorthy et al. (2014) is more challenging, especially non-destructive detection Gleyzes et al. (2007); Johnson et al. (2010); Peaudecerf et al. (2014); Sathyamoorthy et al. (2014). Here we propose a scheme for non-absorbing, high-efficiency detection of single itinerant microwave photons via the nonlinearity provided by an artificial superconducting atom, a transmon Koch et al. (2007b).

Previously Fan et al. (2013), we considered schemes where the signal photon wave packet propagates freely in a open transmission line Hoi et al. (2013); Peropadre et al. (2011), and encounters the lowest transition of a transmon. The cw-probe field couples the first and second excited states of the transmon and is monitored via continuous homodyne detection. Displacements in the homodyne current, due to the large transmon-induced cross-Kerr non-linearity Hoi et al. (2013), indicate the presence of a photon. We showed that, in spite of the exceptionally large cross-Kerr nonlinearity it exhibits Hoi et al. (2013), a single transmon in an open transmission line is insufficient for reliable microwave photon detection, due to saturation of the transmon response to the probe field Fan et al. (2013). More recently, Sathyamoorthy et al. (2014), we showed that multiple cascaded transmons could achieve reliable microwave photon counting in principle, though the number of transmons and circulators required in this scheme presents serious experimental challenges.

Inspired by the references above, a scheme that achieves reliable photon counting with as few as a single transmon is proposed here. The key insight is to use a cavity resonant with the probe field to enhance the probe displacements, which depends on the signal photon number. The measurement efficiency is quantified in two ways: firstly, the signal-to-noise ratio (SNR), and secondly the distinguishability, i.e. the probability to correctly infer the photon number. For a single transmon, a SNR of 1.2 is achieved, corresponding to a distinguishability of $F = 84\%$ between 0 and 1 photons in the signal (i.e. the probability of correctly discriminating these two states). This can be improved using more transmons Sathyamoorthy et al. (2014) and it is shown that with two cascaded transmons the distinguishably increases to $F = 90\%$. An important feature of the proposal is that the signal

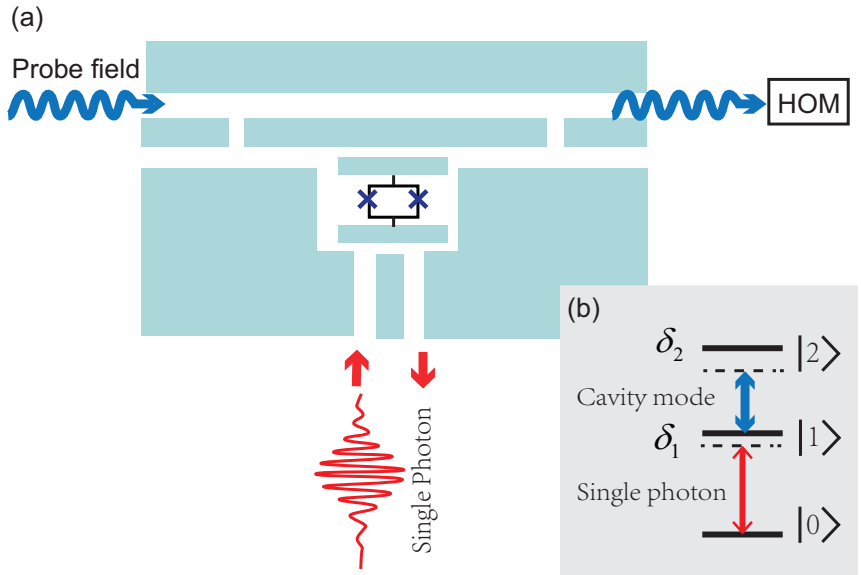

Figure 4.1 – The schematic of single microwave photon counting. (a) A transmon qubit coupled to a microwave cavity is utilized as a nonlinear medium to detect the presence or absence of single microwave photons in a semi-infinite transmission line. When there is no photon in the transmission line, the transmon, prepared in its ground state, cannot be excited to upper energy levels and thus it is transparent to the cavity field; with the presence of the single photon, the cavity field will experience a change due to the interaction with the transmon. (b) The energy level structure of the transmon.

photon is an itinerant photon pulse, enabling detection of relatively wide-band microwave photons.

4.1.1 Model and master equation

The scheme for single microwave photon detection using a single transmon is shown in Fig. 4.1. A transmon is embedded at one end of a waveguide, in which the signal microwave propagates. The signal field is nearly resonant with the lowest transmon transition, $|0\rangle \leftrightarrow |1\rangle$. The transmon is also coupled to a coherently-driven microwave resonator, which is dispersively coupled with the second transmon transition. The cavity is driven by an external coherent probe field, which ultimately yields information about the photon population in the signal field. This *unit* (consisting of the transmon in a cavity) can be cascaded using circulators to achieve higher detection efficiency Sathyamoorthy et al. (2014).

We first analyse a single unit, and later consider cascading several. In a rotating frame the

Hamiltonian describing a single transmon-cavity unit is

$$\hat{H}_s = \delta_1\hat{\sigma}_{11} + (\delta_1+\delta_2)\hat{\sigma}_{22} - ig_{12}(\hat{a}\hat{\sigma}_{21} - \hat{a}^\dagger\hat{\sigma}_{12}) - iE(\hat{a}-\hat{a}^\dagger) \tag{4.1}$$

where $\hat{a}$ is the cavity annihilation operator, g is the coupling strength between the cavity field and the transmon $|1\rangle \leftrightarrow |2\rangle$ transition, E is the driving amplitude, and the detunings are $\delta_1 = \omega_{10} - \omega_s$, $\delta_2 = \omega_{21} - \omega_{cav}$. The interaction between the cavity and the $0 \rightarrow 1$ transition is neglected here, since the cavity is very far detuned from the $0 \rightarrow 1$ transition.

To model the itinerant signal field, we invoke a fictitious source-cavity initially in a Fock state. This field leaks out, producing an itinerant Fock state, which ultimately interacts with the transmon in the real cavity driven by the probe field. The probe field reflected from the real cavity is measured by a homodyne detector. The resulting conditional system dynamics are described by the cascaded, stochastic master equation Carmichael (1993a); Gardiner (1993a); Gardiner and Zoller (2004); Wiseman and Milburn (2010):

$$d\rho = dt\,\mathcal{L}\rho + \sqrt{\eta}dW(t)\,\mathcal{H}[e^{-i\phi}\sqrt{\kappa}\hat{a}]\rho, \tag{4.2}$$

where

$$\begin{aligned}\mathcal{L}\rho &= -i[\hat{H}_s,\rho] + \mathcal{D}[\sqrt{\gamma}_c\hat{c}] + \mathcal{D}[\sqrt{\gamma}_{01}\hat{\sigma}_{01}]\rho \\ &+ \mathcal{D}[\sqrt{\gamma}_{12}\hat{\sigma}_{12}]\rho + \mathcal{D}[\sqrt{\kappa}\hat{a}]\rho + \sqrt{\gamma_c\gamma_{01}}([\hat{c}\rho,\hat{\sigma}_{10}] + [\hat{\sigma}_{01},\rho\hat{c}^\dagger]),\end{aligned} \tag{4.3}$$

and the corresponding homodyne photocurrent is

$$I(t) = \sqrt{\eta\kappa}\left\langle e^{-i\phi}\hat{a} + e^{i\phi}\hat{a}^\dagger\right\rangle + dW(t)/dt \tag{4.4}$$

where dW is a Weiner process satisfying $E[dW] = 0$, $E[dW^2] = dt$, η is the efficiency of homodyne detection, $\hat{c}$ is the annihilation operator of the source-cavity mode, γ_c is the decay rate of the source-cavity (which determines the linewidth of the itinerant photon), the phase angle ϕ is set by the local oscillator phase.

4.1.2 Analysis and simulation results

Prior to arrival of the signal pulse, the cavity is driven by the probe field to its steady state, and the transmon is initially in its ground state. The itinerant signal photon pulse arrives at the transmon at time t_0. Since the signal pulse decays over a finite time, the cavity field is transiently displaced from its steady state. This transient displacement is reflected in the homodyne photocurrent, which thus contains information about the number of photons in the signal pulse. There are several methods to extract this information Gambetta et al. (2007), the simplest of which is a linear filter applied to the homodyne current:

$$S = \int_{t_0}^{T} I(t)h(t)dt, \tag{4.5}$$

for some filter kernel h. The optimal linear filter takes $h(t) = \bar{I}_1(t)$, where $\bar{I}_1$ is the expected homodyne current when there is a single signal photon. We have also implemented more sophisticated non-linear filters, using hypothesis testing Gambetta et al. (2007); Tsang (2012), which yields a small improvement, at a substantial computational cost.

As one measure of performance, we define a signal-to-noise ratio

$$\mathrm{SNR} = \frac{(\bar{S}_1 - \bar{S}_0)}{\sqrt{\mathrm{Var}(S_1) + \mathrm{Var}(S_0)}}, \tag{4.6}$$

where S_n is the filter output conditioned on a signal pulse containing $n = 0$ or 1 photons. Due to the nonlinear interaction between the probe field and the transmon, S_1 is not a Gaussian variable, making SNR difficult to interpret. Thus, we also report the distinguishability F, defined as the probability of correctly inferring from the homodyne current the correct number of signal photons

$$F = \big(P(S < S_{\mathrm{th}}|n = 0) + P(S > S_{\mathrm{th}}|n = 1)\big)/2, \tag{4.7}$$

where S_{th} is a threshold value for S which optimally discriminates between small and large probe displacement. We have also assumed that $n = 0, 1$ are equally likely.

To quantify the performance of a single unit as a photon detector, we perform a Monte-Carlo

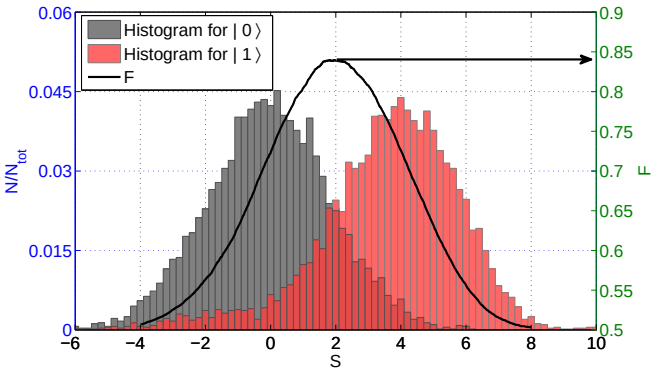

Figure 4.2 – The histograms of filtered Homodyne signal for the presence/absence of the signal photon and the corresponding distinguishability. The black curve plots the distinguishability versus threshold values. The signal photon pulse is an exponentially-decayed pulse from a source cavity and the linear filter function is presented is Eq. (4.5). The parameters are: $\gamma_{01} = 1$, $\gamma_{12} = 0.1$, $g = 2.45$, $\delta_1 = -0.8$, $\delta_2 = -18$, $\gamma_c = 0.1$, $E = 0.032$, $\kappa = 0.037$, $\phi = \pi/2$, $t_0 = 0$ and $T = 80$.

study, generating many trajectories with either $n = 0$ or $n = 1$, and computing S for each. Here we assume $\eta = 1$, which requires quantum limited amplifiers. This assumption sets an upper bound on the performance of this scheme, and we briefly discuss amplifier noise later. Fig. 4.2 shows histograms of S for $n = 0$ (grey) and $n = 1$ (red), for system parameters chosen to maximise F. The peaks of the histograms are reasonably distinguished. The black trace shows F as a function of $S_{\rm th}$. We find $\mathrm{SNR}_1 = 1.2$, and $F_1 = 84\%$, where the subscript denotes a single cavity-transmon unit. This is a substantial improvement over Fan et al. (2013). For comparison, the fidelity using the more sophisticated hypothesis testing filter gives slight improvement $F_1^{\rm HT} = 84.6\%$, which will be discussed in details in the next section.

We note that the optimal choice $\gamma_{12} = 0.1\gamma_{01}$ used in Fig. 4.2 requires that the microwave density-of-states (DOS) in the transmission line be engineered to suppress emission at ω_{12}. Without DOS engineering, $\gamma_{12} = 2\gamma_{01}$ Gambetta et al. (2007), and we find that the fidelity is reduced to $F_1 = 81\%$.

The lifetime for the unit cavity is chosen to optimise single-photon induced transmon excitation. Accordingly, the signal pulse must be a relatively long, matching the cavity life time. With a long pulse and a good cavity, during the interaction time of the signal photon

with the system, the intra-cavity field changes dramatically (see Fig. 1c). In comparison, for situation without a unit cavity, the change in the probe is determined by the transmon coherence $\langle\hat{\sigma}_{12}\rangle < \langle\hat{\sigma}_{11}\rangle$, which decays quickly in that case. The cavity allows the probe field to interact for a long time with the signal-induced coherence in the transmon, resulting in the larger integrated homodyne signal over the measurement time.

The probe amplitude used in Fig. 2 was chosen to optimise the performance of the single-photon detector. Increasing the probe amplitude beyond this level leads to strong saturation effects in the transmon, consistent with the breakdown of an effective cross-Kerr description as discussed in Fan et al. (2013).

The improvement can be explained from the time evolution of key system variables, as seen in Fig. 4.3. To more efficiently make use of the single-photon induced transmon excitation, a good cavity with a long life time is chosen. Accordingly, the input photon pulse should be a relatively long pulse, in order to match the long cavity life time. Here the steady state of the cavity have been displaced out. With a long pulse and a good cavity, during the time of the photon staying in the system, the intra-cavity photon number has a dramatic increase compared to the excitation of $|1\rangle$. While in the transmission line case, the change in the probe is the atomic polarization $\langle\hat{\sigma}_{12}\rangle$, which is in principle smaller than $\langle\hat{\sigma}_{11}\rangle$. After the main part of the photon leaves the system, the transmon excitation will drop to zero quickly due to the relaxation of the transmon. However, at this moment, the intra-cavity field still maintains quite high photon number and then decay to the steady state slowing. This results in a much larger integrated homodyne signal over a measurement time.

4.1.3 Results in the phase space

We have given the analysis based on the statistics from the stochastic simulations above, now we would like to show the cavity state change induced by the signal photon using the quasi-probability functions in the phase space Lee (1995). There are a number of phase space distribution functions such as the Wigner distribution function Wigner (1932), the Husimi Q distribution function Husimi (1940) and the P representation Glauber (1963b); Sudarshan (1963). Here we choose the Wigner distribution function Wigner (1932) to analyze

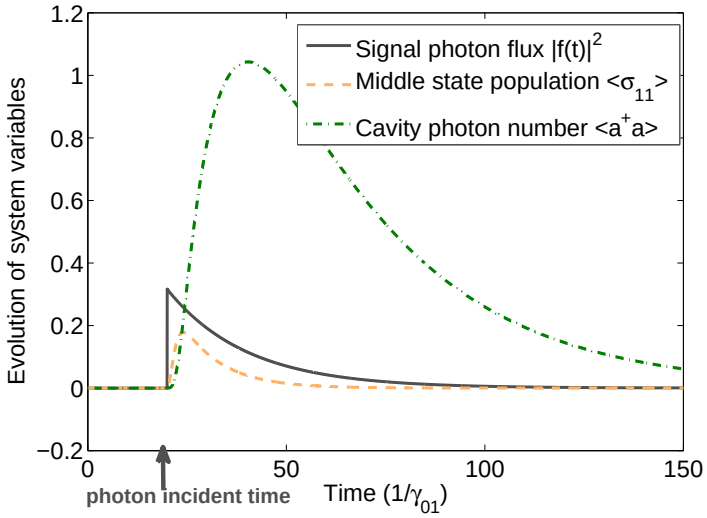

Figure 4.3 – Responses from the transmon and the cavity field to the presence of the target photon pulse. The parameters are the same as those in Fig. 4.2.

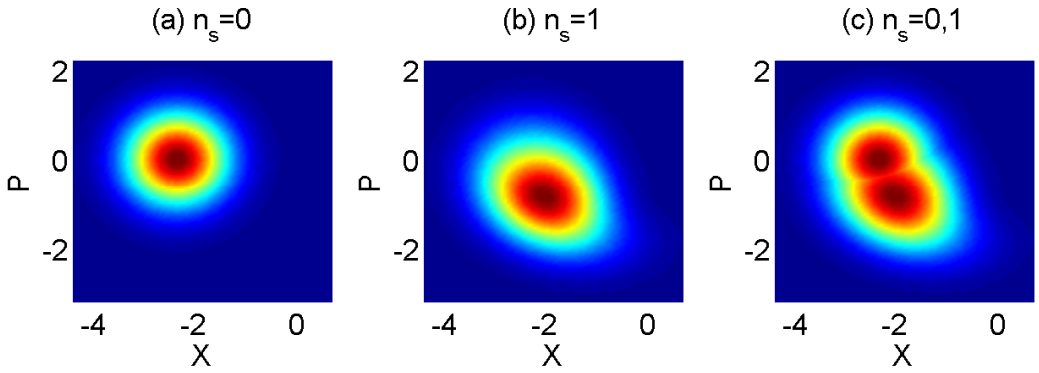

Figure 4.4 – The Wigner function of the cavity field for the case of (a) no signal photon and (b) one signal photon. (c) is the sum of (a) and (b). The parameters are the same as Figure 4.2.

the system properties. The Wigner function over the position and momentum quadratures is given by

$$W(X,P,t) = \frac{1}{\pi}\int dX' e^{-2iX'P} \langle X+X'|\, \rho_c(t) |X-X'\rangle \tag{4.8}$$

with $\rho_c(t) = Tr_{S,A}\rho(t)$ is the reduced density matrix for the cavity mode by tracing out the signal and “atomic" modes. To express the total influence of the signal photon on the cavity field during the interaction in the phase space, we integrate the Wigner function over the

measurement time T_m as

$$W(X, P, T_m) = \int_0^{T_m} W(X, P, t)dt \tag{4.9}$$

Figure 4.4 shows the integrated Wigner function $W(X, P, T_m)$ of the cavity field for the absence (a) and presence (b) of the signal photon at optimal parameter setting in the X-P plane. From (a) to (b), it is clear that there is a shift of the cavity field state along the phase quadrature of the phase space. Figure 4.4(c) is the sum of Figure 4.4 (a) and (b) for contrast. The central parts of the two Wigner distributions are distinguishable with only small fractions overlapped, which is quite consistent with the homodyne signal distributions from the stochastic simulation (Figure 4.2).

4.2 Single microwave photon detection using two cascaded transmons

The peak distinguishability of 84% for a single transmon is potentially useful in some applications. To increase it further, we follow Sathyamoorthy et al. (2014) and cascade multiple transmons using circulators to engineer a unidirectional waveguide. The computational cost of simulating a chain of transmons grows exponentially with the number of transmons, N_{tr}, however it was shown in Sathyamoorthy et al. (2014) that the SNR grows as $\sqrt{N_{\mathrm{tr}}}$, as might be expected for independent, repeated, noisy measurements of the same system. For our purposes, we consider cascading two transmons, A and B. Since our detection process is non-absorbing, and circulators suppress back-scattering, the single microwave photon will deterministically interact with A and then B in order, resulting in dynamical shifts for both cavity modes. We suppose that each cavity is addressed by a separate probe field, leading to two homodyne currents. Again, we expect this to improve the SNR by $\sim \sqrt{2}$.

For computational efficiency in our Monte-Carlo simulations, we unravel the master equation to produce a stochastic Schrodinger equation Moodley and Petruccione (2009); Wiseman and Milburn (2010), including four stochastic processes – three quantum diffusion

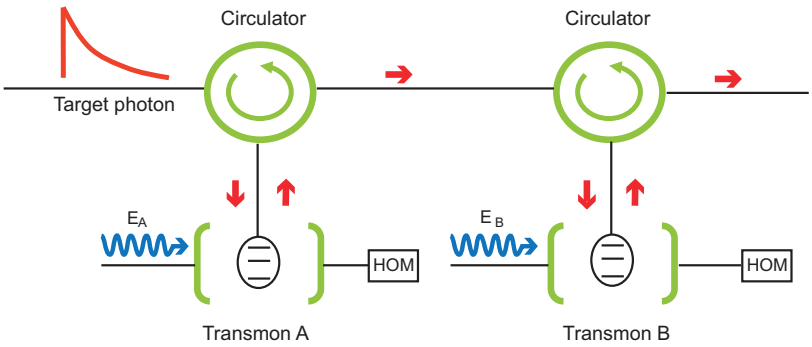

Figure 4.5 – Improved scheme for microwave photon detection with cascaded two transmons. The two transmons A and B sit in two separate cavities with their own probe fields and homodyne detection setups. The single-photon pulse firstly passes transmon A and then transmon B, connected by two circulators.

processes, one per cavity and an additional process to account for cross-relaxation of the transmon into the waveguide, and one quantum-jump process for the signal photon pulse. Note that the jump process is solely to generate the homodyne currents (which are determined by the quantum diffusion processes) and we do not subsequently use the jump records. In the absence of a signal photon, the evolution of the unnormalized system wave function $|\tilde{\psi}\rangle$ is governed by

$$\begin{aligned} d|\tilde{\psi}(t)\rangle &= dt[-i(\hat{H}_s+\hat{H}_{cas})-\frac{1}{2}(\sum_{j=A,B}\kappa_j\hat{a}_j^\dagger\hat{a}_j+\hat{J}^\dagger\hat{J} \\ &+ \hat{J}_2^\dagger\hat{J}_2)+\sum_{i=A,B}(e^{-i\phi_j}\sqrt{\kappa_j}\hat{a}_j)I^{(j)}+\hat{J}_2I_2]|\tilde{\psi}_c(t)\rangle, \end{aligned} \tag{4.10}$$

where

$$\begin{aligned} \hat{H}_s &= \sum_{j=A,B}(\delta_{j1}\hat{\sigma}_{11}^j+(\delta_{j1}+\delta_{j2})\hat{\sigma}_{22}^j-ig_j(\hat{a}_j\hat{\sigma}_{21}^j-\hat{a}_j^\dagger\hat{\sigma}_{12}^j)-iE_j(\hat{a}_j-\hat{a}_j^\dagger)) \\ \hat{H}_{cas} &= -\frac{i}{2}(\sum_{j=A,B}(\gamma_c\gamma_{01}^j)^{1/2}\hat{c}\hat{\sigma}_{10}^j+(\gamma_{01}^A\gamma_{01}^B)^{1/2}\hat{\sigma}_{01}^A\hat{\sigma}_{10}^B+(\gamma_{12}^A\gamma_{12}^B)^{1/2}\hat{\sigma}_{12}^A\hat{\sigma}_{21}^B)+h.c. \end{aligned} \tag{4.11}$$

where we have defined $\hat{J}=\sqrt{\gamma_c}\hat{c}^\dagger\hat{c}+\sum_{j=A,B}\sqrt{\gamma_{01}^j}\,\hat{\sigma}_{01}^j$ and $\hat{J}_2=\sum_{j=A,B}\sqrt{\gamma_{12}^j}\,\hat{\sigma}_{12}^j$. Upon a

jump event in the signal field, the system state evolves discontinuously

$$|\tilde{\psi}(t+dt)\rangle = \hat{J}|\tilde{\psi}(t)\rangle. \tag{4.12}$$

$I^{(j)}(j = A, B)$ are the homodyne signals for the outputs of two probe cavities and I_2 is the fictitious measurement signal for the emission from transmons to the transmission line:

$$\begin{aligned} I^{(j)} &= \sqrt{\kappa_j}\left\langle e^{-i\phi_j}\hat{a}_j + e^{i\phi_j}\hat{a}_j\right\rangle + dW_j/dt \\ I_2 &= \left\langle \hat{J}_2 + \hat{J}_2^\dagger \right\rangle + dW_2/dt \end{aligned} \tag{4.13}$$

When there is a detection of the control photon, the system state will experience a collapse as

$$|\bar{\psi}\rangle = \hat{J}|\bar{\psi}\rangle \tag{4.14}$$

For both "no detection" and "detection" cases, the wave function has to be normalized as $|\psi\rangle = |\bar{\psi}\rangle/\sqrt{\langle\bar{\psi}|\,|\bar{\psi}\rangle}$.

We simulate 8000 trajectories using the same parameter values as before (assuming identical transmon-cavity units), for each choice of n, to obtain a distribution of homodyne currents, $I^{(A)}$ and $I^{(B)}$, which we integrate according to Eq. 4.5 to produce $S^{(A)}$ and $S^{(B)}$. Fig. 4.6(a) shows a scatter plot of the two homodyne signal pairs $(S_n^{(A)}, S_n^{(B)})$ for $n = 0$ (black) and $n = 1$ (red). To distinguish between these two distributions we project onto the sum $S^{(AB)} = (S^{(A)} + S^{(B)})/2$, shown in Fig. 4.6(b), and we calculate $\mathrm{SNR}_2 = 1.7 \approx \sqrt{2}\,\mathrm{SNR}_1$, as expected. Likewise, we define the distinguishability as in Eq. 4.7, replacing S with $S^{(AB)}$. At the optimal S_{th}, we find $F = 90\%$. We note that if the distributions were in fact Gaussian, then this improvement in SNR would give a distinguishability of 91.5%, slightly higher than what we achieve.

Achieving the performance above requires quantum limited amplification, so that $\eta = 1$. Josephson parametric amplifiers provide one avenue to this limit, and are rapidly improving, recently achieving $\eta \approx 0.5$ Abdo et al. (2014); Mallet et al. (2011); Teufel et al. (2009). This

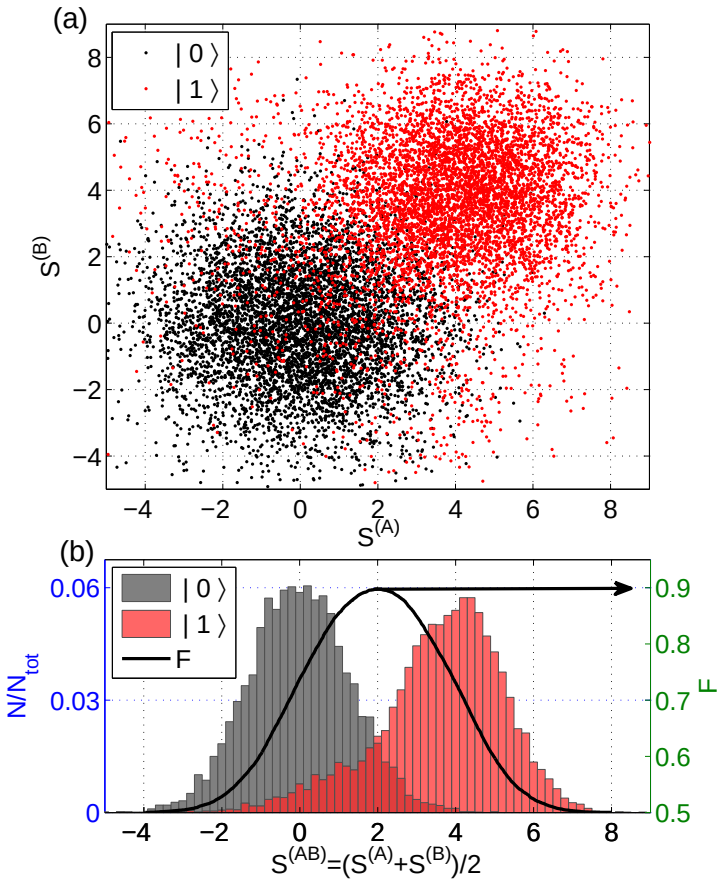

Figure 4.6 – (a) The scatter plot of the filtered Homodyne signals from two probe cavities with the presence/absence of the signal photon. (b) The histogram of the sum Homodyne signal S_{AB} and the corresponding distinguishability in the two cascaded transmons case. The parameters are: $\gamma_{01}^A = \gamma_{01}^B = 1$, $\gamma_{12}^A = \gamma_{12}^B = 0.1$, $g_A = g_B = 2.45$, $\delta_{1A} = \delta_{1B} = -0.8$, $\delta_{2A} = \delta_{2B} = -18$, $\gamma_c = 0.1$, $E_A = E_B = 0.032$, $\kappa_A = \kappa_B = 0.037$, $\phi_A = \phi_B = \pi/2$, $t_0 = 0$ and $T = 80$.

compares very favorably to HEMT amplifiers for which $\eta \approx 1\%$ Mallet et al. (2011); Teufel et al. (2009). From Eqs. 4.2 and 4.4, we see that if $\eta < 1$, the signal is reduced by a factor of $\sqrt{\eta}$ and the total noise is also slightly reduced. Thus we estimate that for current state-of-the-art with $\eta = 0.5$, $\mathrm{SNR}_1 \approx 0.94$ which implies $F \approx 75.5\%$. Anticipating $\eta = 0.8$ may be achievable in the near future, in which case we estimate $\mathrm{SNR}_1 = 1.15$ and $F \approx 80\%$.

4.3 Quantum hypothesis testing

The single-photon detection problem in our model discussed above is actually a quantum binary decision problem, i.e., to determine the presence/absence of a single photon. This issue can be treated using the quantum hypothesis testing Helstrom (1967, 1968, 1969); Tsang (2012); Van Trees (2004). Quantum hypothesis testing gives a estimation of the state of a quantum system among a finite number set of possible states with minimum error probabilities. Recently it has been applied to qubit state readout Gambetta et al. (2007).

To explain the basic idea of quantum hypothesis testing, we take a binary-state system as an example. To make a decision about such a binary-state system, two hypotheses are involved: a null hypothesis $\mathcal{H}_0$ and an alternative hypothesis $\mathcal{H}_1$, which is the event of interest. In our case, $\mathcal{H}_0$ and $\mathcal{H}_1$ correspond to two distinct initial conditions specified by possible photon numbers in the signal.

Based on a homodyne measurement record $I(t)$, we make two hypotheses: there is no photon or there is one photon in the signal. The system state conditioned on no signal photon can be described by the unnormalized stochastic master equation:

$$d\rho^0 = dt(\mathcal{L}^0\rho^0 + I(t)(e^{-i\phi}\hat{a}\rho^0 + e^{i\phi}\rho^0\hat{a}^\dagger)) \tag{4.15}$$

where

$$\mathcal{L}^0\rho = -i[\hat{H}_s, \rho] + \mathcal{D}[\sqrt{\gamma}_{01}\hat{\sigma}_{01}]\rho + \mathcal{D}[\sqrt{\gamma}_{12}\hat{\sigma}_{12}]\rho + \mathcal{D}[\sqrt{\kappa}\hat{a}]\rho, \tag{4.16}$$

and the probability of no photon based on the measurement record $I(t)$ is

$$p(0|i) \sim \mathrm{Tr}(\rho^0) \tag{4.17}$$

where $i = 0$ or 1, depending on which state the record $I(t)$ corresponding to.

The system state conditioned on one signal photon can be described by the unnormalized

stochastic master equation:

$$d\rho^1 = dt(\mathcal{L}^1\rho^1 + I(t)(e^{-i\phi}\hat{a}\rho^1 + e^{i\phi}\rho^1\hat{a}^\dagger)) \tag{4.18}$$

where

$$\begin{aligned}\mathcal{L}^1\rho^1 &= -i[\hat{H}_s,\rho] + \mathcal{D}[\sqrt{\gamma}_c\hat{c}] + \mathcal{D}[\sqrt{\gamma}_{01}\hat{\sigma}_{01}]\rho \\ &+ \mathcal{D}[\sqrt{\gamma}_{12}\hat{\sigma}_{12}]\rho + \mathcal{D}[\sqrt{\kappa}\hat{a}]\rho + \sqrt{\gamma_c\gamma_{01}}([\hat{c}\rho,\hat{\sigma}_{10}] + [\hat{\sigma}_{01},\rho\hat{c}^\dagger]),\end{aligned} \tag{4.19}$$

The probability of having a single photon based on the measurement record $I(t)$ is

$$p(1|i) \sim \mathrm{Tr}(\rho^1) \tag{4.20}$$

A quantity used for comparing probabilities of the two hypotheses called the likelihood ratio is defined as

$$\Lambda = \frac{\mathrm{Tr}(\rho^1)}{\mathrm{Tr}(\rho^0)} \tag{4.21}$$

which is a comparison of the probabilities of the two hypotheses. Practically, we can set a threshold value for the likehood ratio, Λ_{th}, and for each trajectory we compare Λ with this threshold and decide which state the signal mode is, i.e., for j_{th} trajectory, if $\Lambda > \Lambda_{th}$, conditioned on have i photon (i=0,1), $P_j(0|i) = 0$ amd $P_j(1|i) = 1$. The distinguishability F or the correct probability P_c between no signal photon and one signal photon is defined as

$$\begin{aligned}F = P_c &= 1 - P_e \\ &= 1 - \frac{1}{2}(\sum_j^n P_j(0|1)/n + \sum_j^n P_j(1|0)/n) \\ &= \frac{1}{2}(\sum_j^n P_j(0|0) + \sum_j^n P_j(1|1))/n\end{aligned} \tag{4.22}$$

where we have chose the priori for both no photon and one photon hypotheses as $\frac{1}{2}$ and n is the total number of trajectories.

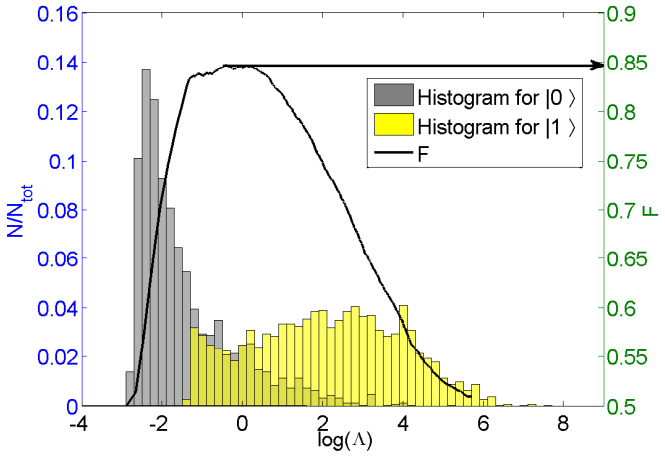

Figure 4.7 – The histogram of the likehood ratio Λ for zero and one photon states and the distinguishability. The priori probabilities $P_0 = P_1 = \frac{1}{2}$ for both no photon and one photon hypotheses.

Figure 4.7 show the histograms of $\log\Lambda_{\rm i}$, for the cases $i = 0$ and $i = 1$. Unlike the histogram of the filtered homodyne signals, the histograms for the likelihood values are not Gaussian distributions due to the nonlinear filtering process. There is a slight improvement in the distinguishability compared to the linear filter situation (F=84.6%). However, to evaluate the distinguishability using quantum hypothesis test, one needs to solve nonlinear master equations, which is much more time and resources consuming than stochastic unraveling using system wave functions. Therefore, the small improvement is not worth the effort.

4.4 Measurement induced decoherence and pulse distortion

In our proposed detector, there is in fact some distortion of the signal pulse envelope, as the transmon-cavity unit coherently interacts with the signal field, closely analogous to the pulse envelope distortion found in Sathyamoorthy et al. (2014). This is shown in Fig. 4.8(a). Here, we have allowed the detuning δ_2 to vary, in order to vary the distinguishability from almost undistinguishable $F = 0.5$ to the best achievable $F = 0.9$. We see that the pulse envelope is maximally distorted when F is largest, which follows since this is the condition under which the measurement back-action in maximized. For photon counting considered in this

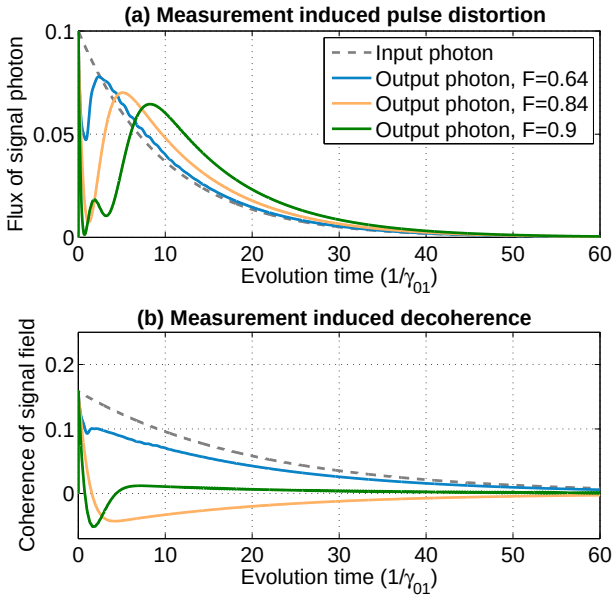

Figure 4.8 – (a) Pulse envelope distortion. (b) Measurement induced decoherence of the signal microwave photon state. The grey dash curves denote the input signal field and the solid curves denote the output signal field at different distinguishability. The blue ($\delta_2 = -6$) and orange ($\delta_2 = -18$) curves represent the output signal field after interacting with one transmon and the green ($\delta_{2A} = \delta_{2B} = -18$) curves represent the output signal field after interacting with two transmons. The other parameters are: $\gamma_{01}^A = \gamma_{01}^B = 1$, $\gamma_{12}^A = \gamma_{12}^B = 0.1$, $g_A = g_B = 2.45$, $\delta_{1A} = \delta_{1B} = -0.8$, $\gamma_c = 0.1$, $E_A = E_B = 0.032$ and $\kappa_A = \kappa_B = 0.037$.

work, the deterministic pulse distortion is not a significant issue. However it may become so if the transmon were to be used to induce gates between photon-encoded states (e.g. in an interferometer), since the pulse-shape would encode some amount of 'which-path' information leading to a reduction in coherence between different paths Shapiro (2006). It may be possible to circumvent this problem, albeit at the cost of significant complexity Chudzicki et al. (2013).

Next, we turn to measurement induced decoherence effect. To study this, we consider what happens to a signal field that is prepared in a superposition of Fock states. In this case, QND measurement of the photon number should cause decoherence between the components in the superposition, leaving populations unchanged Brune et al. (1996); Slichter et al. (2012). Suppose $\hat{r}$ is an operator acting on the signal field. In a QND number measurement, $[\hat{r}^\dagger \hat{r}, \hat{H}_s] = 0$, while $[\hat{r}, \hat{H}_s] \neq 0$ so that the coherence between Fock subspaces $\langle \hat{r} \rangle$ decays during the interaction.

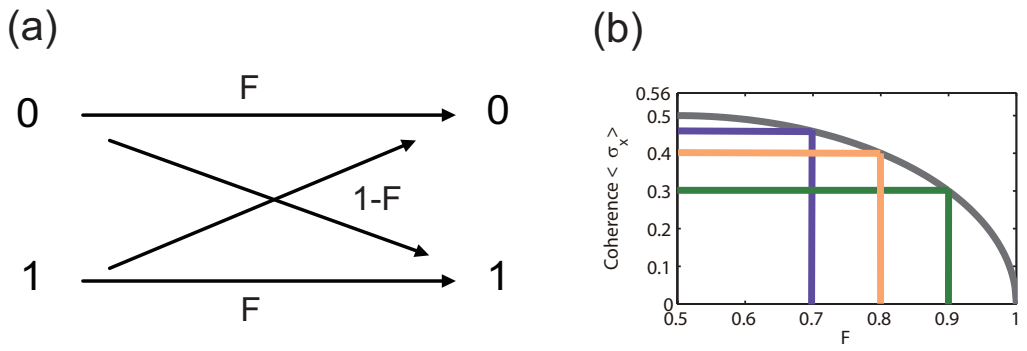

Figure 4.9 – (a) Discrimination of states $|0\rangle$ and $|1\rangle$ with distinguishability F. (b) The illustration of the relation between the system coherence and the distinguishability.

To explain the decoherence effect clearly, we first consider a toy model using a POVM to study the relation between the measurement efficiency and the decoherence effect. Suppose that we perform measurements on a binary system with states labels as $|0\rangle$ and $|1\rangle$. Two positive operators associated with measurements of two states $|0\rangle$ and $|1\rangle$ are defined as:

$$\begin{aligned} \hat{k}_0 &= \sqrt{F}|0\rangle\langle 0| + \sqrt{1-F}|1\rangle\langle 1| \\ \hat{k}_1 &= \sqrt{1-F}|0\rangle\langle 0| + \sqrt{F}|1\rangle\langle 1| \end{aligned} \tag{4.23}$$

where F is the efficiency of measuring two states and the operators $\hat{k}_0$ and $\hat{k}_1$ satisfy the completeness condition $\hat{k}_0^\dagger\hat{k}_0 + \hat{k}_1^\dagger\hat{k}_1 = 1$. Assuming that the initial state is $|\psi_{in}\rangle = c_0|0\rangle + c_1|1\rangle$, the density matrix for the output state is

$$\rho_{out} = \hat{k}_0|\psi_{in}\rangle\langle\psi_{in}|\hat{k}_0^\dagger + \hat{k}_1|\psi_{in}\rangle\langle\psi_{in}|\hat{k}_1^\dagger, \tag{4.24}$$

and the off-diagonal coherence remaining after the measurements is

$$\langle\hat{\sigma}_x\rangle = \mathrm{Tr}((|0\rangle\langle 1| + |1\rangle\langle 0|)\rho_{\mathrm{out}}) = \sqrt{\mathrm{F}(1-\mathrm{F})}(\mathrm{c}_0^*\mathrm{c}_1 + \mathrm{c}_0\mathrm{c}_1^*) \tag{4.25}$$

For perfect measurements, $F = 1$ and $\langle\hat{\sigma}_x\rangle = 0$, which indicates that the system coherence vanishes; for worst measurements or completely indistinguishable states, $F = 0.5$ and $\langle\hat{\sigma}_x\rangle = 0.5$, which indicates that the system coherence remains the initial value. The dependence of the coherence remaining in the system after measurements on the mea-

surement efficiency F is plotted in Figure 4.9(b). In the regime that the states are not well distinguishable or the measurement is not successful, the coherence decreases slowing as F increases. As the measurement of the system states approaches unit efficiency, the coherence tends to rapidly decreases as F increases.

To demonstrate this effect via our detection model, we take a superposition state $(|0\rangle + |1\rangle)/\sqrt{2}$ as the initial state of the fictitious source-cavity and see how $\langle\hat{r}\rangle$ evolves during the measurement process. Fig. 4.8(b) shows the time evolution of $\langle\hat{r}\rangle$, for different values of distinguishability. This confirms that when the system is tuned to maximise the distinguishability, coherence is most rapidly suppressed.

4.5 Two-photon process

The saturation effects come from the single photon transition. By going to few photon transitions, maybe saturation effects can be reduced. To study this situation, a different configuration is considered: the interaction between the cavity field and the transmon 1-2 transition is a two-photon process. The remaining part of the system is the same as the previous sections. In this configuration, once the transmon is excited from its ground state to the middle state by the signal photon, two photons in the cavity can be absorbed and released by the the transmon 1-2 transition in one cycle, therefore we expect that one signal photon induces double phase shifts on the cavity field.

The Hamiltonian for a phenomenological model which we invoke as a starting point is ($\hbar = 1$)

$$\hat{H} = g(\hat{a}^{\dagger 2}\hat{\sigma}_{12} + \hat{a}^2\hat{\sigma}_{21}) \tag{4.26}$$

Compared to a one-photon process described by the Jaynes-Cumming Hamiltonian $H = g(\hat{a}^\dagger\hat{\sigma}_{12} + \hat{a}\hat{\sigma}_{21})$, the chance for a two-photon process to occur is much lower and therefore two-photon coupling coefficient is quite small in current lab conditions. The corresponding

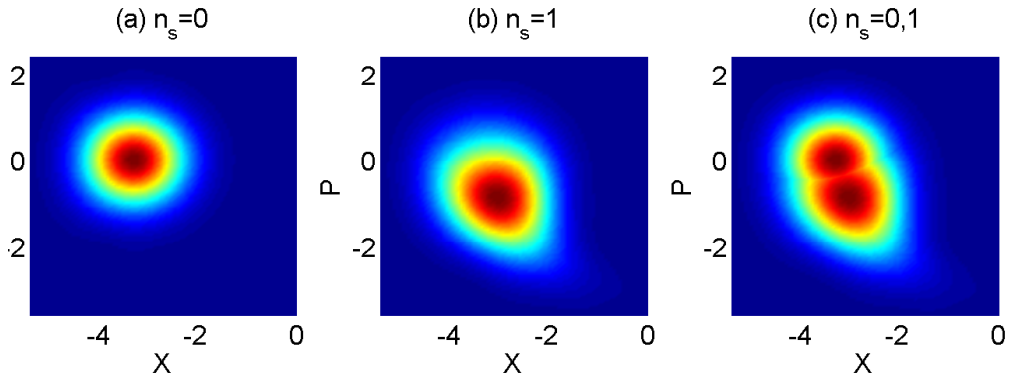

Figure 4.10 – The Wigner function of the cavity field for the case of (a) no signal photon and (b) one signal photon in a two-photon process. (c) is the sum of (a) and (b). The parameters are:$\gamma = 1$, $\gamma_c = 0.1$, $\kappa = 0.038$, $g = 0.8$, $\delta_2 = -15$, $\delta_1 = -0.521$ and $E = 0.0452$.

motion equations for the cavity field operators are

$$\begin{aligned} \dot{a} &= -i2g\hat{a}^\dagger\hat{\sigma}_{12} - \kappa/2\hat{a} + \sqrt{\kappa}\hat{a}_{in} \\ \dot{a}^\dagger &= i2g\hat{a}\hat{\sigma}_{21} - \kappa/2\hat{a}^\dagger + \sqrt{\kappa}\hat{a}_{in}^\dagger \end{aligned} \tag{4.27}$$

In the bad-cavity limit, $\kappa \gg g, \langle\hat{a}\rangle$,

$$\hat{a} = \frac{2}{\kappa}(-i2g(\frac{2}{\kappa}(2ig\hat{a}\hat{\sigma}_{21} + \sqrt{\kappa}\hat{a}_{in}^\dagger))\hat{\sigma}_{12} + \sqrt{\kappa}\hat{a}_{in}) \tag{4.28}$$

The first-order term of $\hat{a}$ is

$$\hat{a}^{(1)} = \frac{-8ig}{\kappa\sqrt{\kappa}}\hat{a}_{in}^\dagger\hat{\sigma}_{12} + \frac{2}{\sqrt{\kappa}}\hat{a}_{in} \approx \frac{-8ig\alpha_{in}^*}{\kappa\sqrt{\kappa}}\hat{\sigma}_{12} + \frac{2}{\sqrt{\kappa}}\hat{a}_{in} \tag{4.29}$$

Substituting the first-order solution Eq. (4.29) into the system Hamiltonian Eq. (5.27) and keep the leading order, we have

$$\hat{H}_{\text{eff}} \approx \sqrt{\gamma_{\text{eff}}}(\alpha_{in}\hat{\sigma}_{12} + \alpha_{in}\hat{\sigma}_{21}) \tag{4.30}$$

	Signal ($S_1 - S_0$)	Variance 1 (V_1)	Variance 0 (V_0)	SNR
1	16.1	100.2	80	1.20
2	17.3	146.9	80	1.13

Table 4.1 – The data comparison between the one-photon transition case (1) and the two-photon transition case (2). V_i (i=0,1) denote the variances for zero/one signal photon states.

where we have assumed the input field is real and $\sqrt{\gamma_{eff}} = \frac{4g\alpha_{in}}{\kappa}$. The input-output relation is

$$\hat{a}_o^{(1)} = \sqrt{\kappa}\hat{a}^{(1)} - \hat{a}_{in} \approx -2i\sqrt{\gamma_{\rm eff}}\hat{\sigma}_{12} + \hat{a}_{in} \tag{4.31}$$

By comparison with the results in the one-photon process case, $\hat{H} = \sqrt{\gamma}(\alpha^*\hat{\sigma}_{12} + \alpha\hat{\sigma}_{21})$ and $\hat{a}_o = -i\sqrt{\gamma}\hat{\sigma}_{12} + \hat{a}_{in}$, it is obvious that there is a factor of 2 enhancement in Eq. 4.31. We can extend this analysis to a N-photon process using the same procedure and it is easy to obtain the N-photon process effective Hamiltonian $\hat{H}_{\rm eff}^{(N)} = \sqrt{\gamma_{\rm eff}}(\alpha^*\hat{\sigma}_{12} + h.c.)$ and the output field $\hat{a}_o^{(N)} = -iN\sqrt{\gamma_{\rm eff}}\hat{\sigma}_{12} + \hat{a}_{in}$ with $\gamma_{\rm eff} = (g2^N\alpha^{N-1}/\sqrt{\kappa}^N)^2$.

However, the analysis above requires the bad cavity limit, which conflicts with the interpretation of the improvement of SNR by a good cavity. We have optimized parameters of the system with the two-photon process using the quantum master equation

$$\begin{aligned} \frac{d\rho}{dt} &= -i[\hat{H}_s, \rho] + \mathcal{D}[\sqrt{\gamma}_c\hat{c}] + \mathcal{D}[\sqrt{\gamma}_{01}\hat{\sigma}_{01}]\rho \\ &+ \mathcal{D}[\sqrt{\gamma}_{12}\hat{\sigma}_{12}]\rho + \mathcal{D}[\sqrt{\kappa}\hat{a}]\rho + \sqrt{\gamma_c\gamma_{01}}([\hat{c}\rho, \hat{\sigma}_{10}] + [\hat{\sigma}_{01}, \rho\hat{c}^\dagger]), \end{aligned} \tag{4.32}$$

where

$$\hat{H}_s = (\Delta_2 + \Delta_1)\hat{\sigma}_{22} + \Delta_1\hat{\sigma}_{11} - ig(\hat{a}^2\hat{\sigma}_{21} - \hat{a}^{\dagger 2}\hat{\sigma}_{12}) - iE(\hat{a} - \hat{a}^\dagger) \tag{4.33}$$

where $\Delta_2 = \omega_{21} - 2\omega_c$ and $\Delta_1 = \omega_{10} - \omega_s$. The best SNR in this configuration is about 1.12 and for simplicity here we will not perform the numerous stochastic simulations, instead, we present the Wigner distribution of the cavity field after interaction with zero/one signal photon, see Figure 4.10. It is a little less distinguishable between zero and one photon states and the noise distribution of the one-photon input case is larger and it is more deformed relative to a gaussian distribution, compared to its counterpart in Figure 4.4. Table 4.1 gives the direct comparison between the results between the one-photon process and the two-photon process. It is seen that the slight reduction in SNR of the two-photon process is not due to the small phase shift or small signal. Actually, the phase shift is a little larger but higher nonlinearity of the two-photon process makes the noise much larger.

Thus, there is no improvement in SNR from a one-photon process to a two-photon process. Also, generally a two-photon process has less probability to happen, i.e., a lower coupling rate. Therefore, we conclude that a two-photon probe transition is not optimal for the single photon detection in our model, though in other applications its high nonlinearity may help.

4.6 Conclusion

In summary, we have demonstrated a proposal for counting itinerant microwave photons in a non-absorbing manner, which exploits the large cross-Kerr nonlinearity of a single transmon in a microwave waveguide Hoi et al. (2013). By synthesising results from Fan et al. (2013); Sathyamoorthy et al. (2014), and adding a local cavity to each transmon, we find that we can cascade multiple such devices to produce effective photon counters. With just two, we achieve a distinguishability of 90%, which may be useful in certain microwave experiments. We anticipate that 3 or 4 units could achieve fidelities up to 95%.

Additionally, during the investigation of the photon detection scheme, we observe the inevitable measurement induced backaction, even in the QND type of measurement. We quantitatively study the measurement induced pulse distortion and decoherence and the results confirm that the higher the measurement efficiency, the larger the measurement induced backaction (more serious pulse distortion and more rapid decoherence).

Chapter 5

Bifurcations in a coupled-resonator and optomechanical system

In this chapter I will talk about a subject different from preceding chapters: a system consisting of two coupled ring resonators with one resonator mechanically oscillating. The stability and dynamical phases of the system is studied using a linearized analysis. It is observed that the system variables exhibit bistability and limit cycle dynamics and the optomechanical nonlinearity has a dramatic influence on the coupled-resonator induced transparency effect. Moreover, the system is shown to have good sensitivity for detection of weak impulsive forces.

5.1 Coupled-resonator induced transparency (CRIT)

In a Λ-type three-level atomic system, the transparency of light coupled to one transition of the atomic system is induced with the presence of a strong control field coupled to the other transition due to the destructive interference. This effect is referred as Electromagnetically induced transparency (EIT) Harris (2008), depicted in the left panel of Fig. 5.1. This is a well-known quantum effect in radiation-matter systems. As an introduction, I will talk about a classical optical anology of EIT–the coupled-resonator induced transparency (CRIT) Smith et al. (2004), a phenomenon of transparency of a light when it passes two closely located identical ring optical resonators. The CRIT effect was first put forward in Smith et al. (2004) and then experimentally observed in Naweed et al. (2005); Xu et al. (2006a). Below I will show how the coupled-resonator induced transparency happens.

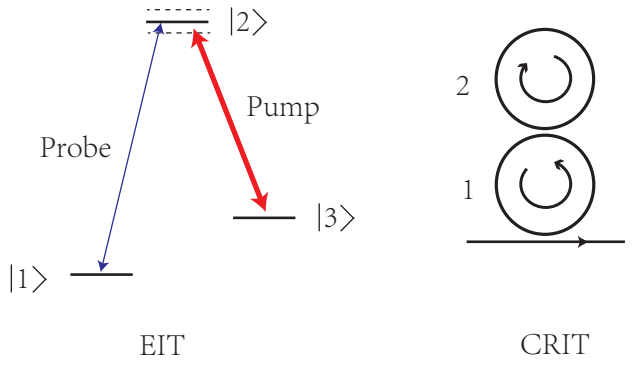

Figure 5.1 – Left is a typical Λ-type three-level system for the EIT effect; Right is a coupled-resonator optical waveguide system for the CRIT effect.

Here I consider a simple model: a system consisting of two identical coupled ring resonators, one of which is evanescently coupled to a waveguide, as shown in the right panel of Fig. 5.1. The equations of motion for resonator modes are given by:

$$\frac{d\hat{a}}{dt} = (i\omega_0 - \kappa_1 - \kappa_2)\,\hat{a} - ig\hat{b} + \sqrt{\kappa_1}\hat{a}_{in} \tag{5.1}$$

$$\frac{d\hat{b}}{dt} = (i\omega_0 - \kappa_2)\,\hat{b} - ig\hat{a} \tag{5.2}$$

where ω_0 is the frequency of ring resonators, κ_1 is the decay rate of the first resonator mode to the waveguide, κ_2 is the loss rate of the resonators and g is the coupling between two resonators. I denote $\hat{a}_{in}$, $\hat{a}$ and $\hat{b}$ as the input mode, first resonator mode and second resonator mode.

Using the input-output relation $\hat{a}_{out} = \hat{a}_{in} - \sqrt{\kappa_1}\hat{a}$, the transmission rate of the waveguide for monochromatic incident light of frequency ω is

$$T = \left|\frac{\langle\hat{a}_{out}\rangle}{\langle\hat{a}_{in}\rangle}\right|^2 \tag{5.3}$$

$$= \left|1 - \frac{\kappa_1}{\left(i\Delta + \frac{g^2}{(i\Delta+\kappa_2)} + \kappa_1 + \kappa_2\right)}\right|^2 \tag{5.4}$$

Fig. 5.2 shows the transmission rate of light through the waveguide as a function of the

detuning $\Delta = \omega_0 - \omega$. Around the resonance, the transmission is nearly perfect, which is similar to the result in the EIT effect.

The CRIT effect has a variety of applications, such as slowing and stopping light Totsuka et al. (2007); Xu et al. (2006b) and signal routing Mancinelli et al. (2011). When it works in highly nonlinear regime, the system shows bistability Lu et al. (2008), which is suggested as an optical switch Maes et al. (2005)

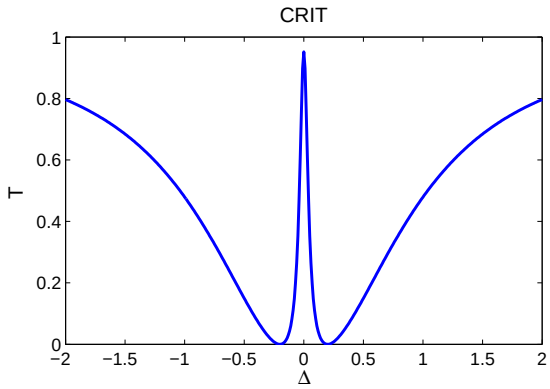

Figure 5.2 – The probe transmission rate versus the detuning in the CRIT system. The parameters are $\kappa_1 = 1$, $\kappa_1 = 0.001$ and $g = 0.2$.

5.2 Cavity optomechanics

Cavity optomechanics is concerned with the interplay between electromagnetic radiations and mechanical motions. Radiation fields can be coupled to mechanical motion through radiation pressures. This phenomenon has its roots in the context of gravitational wave detection Blair (2005); Braginskii and Manukin. The effects on motions of massive objects by radiation pressures were first experimentally demonstrated at the beginning of the 20th century Lebedew (1901); Nxcnons and Huu (1901). In the past few decades, optomechanical systems have been playing crucial roles in manipulating photonic and phononic fields in the frontier research of ultrasensitive detection, quantum optics and quantum information. So far, a variety of novel optomechanical systems have been developed, such as microtoroids Schliesser et al. (2006), optomechanical crystals Eichenfield et al. (2009), membranes Thompson et al. (2008), micromirrors Gigan et al. (2006) and microspheres Li et al. (2011).

5.2.1 Hamiltonian of optomechanical interaction

Typically, there are two kinds of opto-mechanical couplings. The first is dispersive coupling, which results from the mechanical motion modulating the resonance frequency of the optical cavity. The other is dissipative coupling, in which case the position of the mechanical resonator modulates the cavity damping rate Elste et al. (2009).

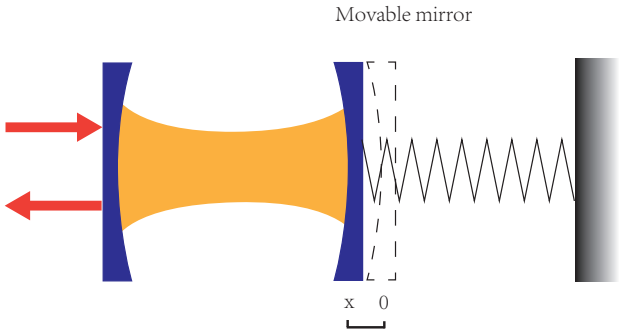

Figure 5.3 – Schematic diagram for the optomechanical system. The position of the movable mirror varying the frequency of the optical cavity leads to opto-mechanical coupling.

Most work in cavity optomechanics (both theoretically and experimentally) focuses on dispersive coupling, which will be introduced below. A basic optomechanical system is a Fabry-Perot cavity with a movable mirror (Fig. 5.3) and the system Hamiltonian is given by

$$\hat{H} = \hbar\omega_c(x)\,\hat{a}^\dagger\hat{a} + \hbar\omega_m\hat{b}^\dagger\hat{b} \tag{5.5}$$

Here the frequency of optical cavity $\omega(x)$ is mechanical position dependent. $\hat{a}(\hat{a}^\dagger)$ and $\hat{b}(\hat{b}^\dagger)$, respectively, denote the annihilation (creation) operators for the optical mode and the mechanical mode. For small displacement with respect to the original position (shown in figure 1), the frequency of cavity can be expanded as

$$\begin{aligned}\omega_c(x) &= \frac{\omega_c}{1+x/L} \\ &= \omega_c - x\frac{\omega_c}{L} + \ldots\end{aligned} \tag{5.6}$$

where ω_c is the resonance frequency of the cavity with a length L. If we keep the leading

term of the cavity frequency, Eq. (5.6) becomes

$$\omega_c(x) = \omega_c - x\frac{\omega_c}{L} \tag{5.7}$$

where $x = x_{ZPF}\left(\hat{b}^\dagger + \hat{b}\right)$ is the displacement of the end mirror with the zero-point fluctuation amplitude $x_{ZPF} = \sqrt{\hbar/2m\omega_m}$. Then the Hamiltonian 5.5 can be rewritten in an optomechanical coupling form:

$$H = \hbar\omega_c\hat{a}^\dagger\hat{a} + \hbar\omega_m\hat{b}^\dagger\hat{b} - \hbar g_0\hat{a}^\dagger\hat{a}\left(\hat{b}^\dagger + \hat{b}\right) \tag{5.8}$$

where $g_0 = x_{ZPF}\omega_c/L$ is the single photon optomechanical coupling strength. The interaction between the optical field and the mechanical mode $H_{in} = -\hbar g_0\hat{a}^\dagger\hat{a}\left(\hat{b}^\dagger + \hat{b}\right)$ is cubic in terms of system operators, providing the basis for rich nonlinear dynamics of optomechanical systems.

5.2.2 Equations of motion for optomechanical system

We assume the optical mode of the system is driven by a laser $\hat{a}_{in}$ with frequency ω_L. With inclusion of thermal fluctuations of mechanical resonator $\hat{F}$ of the mechanical mode, the equations of motion for the system operators are given by

$$\dot{\hat{a}} = (i\Delta - \kappa/2)\hat{a} + ig_0\hat{a}(\hat{b}^\dagger + \hat{b}) + \sqrt{\kappa}\hat{a}_{in} \tag{5.9}$$

$$\dot{\hat{b}} = (i\omega_m - \gamma/2)\,\hat{b} + ig_0\hat{a}^\dagger\hat{a} + \sqrt{\gamma}\hat{F} \tag{5.10}$$

where $\Delta = \omega_L - \omega_c$ is the detuning between the frequency of cavity and laser field, κ is the cavity decay rate and γ is the mechanical damping. For a thermal system, F satisfies the two-time correlation functions:

$$\left\langle \hat{F}(t)\,\hat{F}^\dagger(t')\right\rangle = (n_{th}+1)\,\delta(t-t') \tag{5.11}$$

$$\left\langle \hat{F}(t)\,\hat{F}\left(t'\right)\right\rangle = \left\langle \hat{F}^\dagger(t)\,\hat{F}^\dagger(t')\right\rangle = 0 \tag{5.12}$$

where the mean excitation number of the environment n_{th} is given by

$$n_{th}^{-1} = e^{\hbar\omega_m/k_B T_0} - 1 \tag{5.13}$$

where T_0 is the environmental temperature and k_B is Boltzmann constant.

5.3 Bifurcations in optomechanical systems

Equations 5.9 and 5.10 are nonlinear in the field amplitudes, very rich nonlinear phenomena have been reported in opto-mechanical systems with different input intensities or detunings with respect to the cavity resonance, such as bistability Aldana et al. (2013); Ghobadi et al. (2011); Jiang et al. (2013), instability Ludwig et al. (2008); Qian et al. (2012), multistability Dong et al. (2011); Marquardt et al. (2006), self-sustained oscillations Metzger et al. (2008); Zaitsev et al. (2011) and chaos Carmon et al. (2007); Marino and Marin (2013). The system considered in this chapter exhibits bistability and self-sustained oscillations, therefore in the following I will review these two nonlinear effects.

5.3.1 Fixed points, stability and linear analysis

Before talk about bifurcations, I would like to give a brief review on fixed points, stability and linear analysis of a nonlinear system.

For a dynamical system

$$\dot{\vec{x}} = f(\vec{x}), \tag{5.14}$$

if $\vec{x}^*$ is a fixed point, it is independent on the time, that is, $\dot{\vec{x}}^* = 0$. Therefore a fixed point is a solution of the equation $f(\vec{x}) = 0$. If a perturbation from a fixed point damps in time, we call it a stable fixed point; if a perturbation grows in time, we call it an unstable fixed point.

Linear stability analysis is a useful tool to quantitatively study the stability of fixed points in a nonlinear system. It is based on the first-order perturbation equations, with high-order

perturbations ignored. Following Strogatz (2001), a two-dimensional nonlinear system is taken as an example to show the procedure of the linear stability analysis. The equations of motion of the system are assumed to have the general form as

$$\dot{x} = f(x, y) \tag{5.15}$$

$$\dot{y} = g(x, y) \tag{5.16}$$

The fixed point of the system (x^*, y^*) can be solved by setting the time derivatives to zeros. The fluctuations around the fixed point or the steady state solution is denoted by

$$u = x - x^* \tag{5.17}$$

$$v = y - y^* \tag{5.18}$$

The equations of motion for the fluctuations (u, v) are

$$\begin{aligned} \dot{u} &= \dot{x} = f(x^* + u, y^* + v) \\ &= f(x^*, y^*) + u\frac{\partial f}{\partial x} + v\frac{\partial f}{\partial y} + O(u^2, v^2, uv) \\ &= u\frac{\partial f}{\partial x} + v\frac{\partial f}{\partial y} + O(u^2, v^2, uv) \\ \dot{v} &= u\frac{\partial g}{\partial x} + v\frac{\partial g}{\partial y} + O(u^2, v^2, uv) \end{aligned} \tag{5.19}$$

For small fluctuations, we ignore the quadratic terms $O(u^2, v^2, uv)$ and then can write the equations as

$$\begin{pmatrix} \dot{u} \\ \dot{v} \end{pmatrix} \approx J(x^*, y^*) \begin{pmatrix} u \\ v \end{pmatrix} \tag{5.20}$$

where $J(x^*, y^*) = \begin{pmatrix} \frac{\partial f}{\partial x} & \frac{\partial f}{\partial y} \\ \frac{\partial g}{\partial x} & \frac{\partial g}{\partial y} \end{pmatrix}$ is the Jacobian matrix. The corresponding characteristic equation is

$$|J(x^*, y^*) - \lambda| = \lambda^n + b_1\lambda^{n-1} + ... + b_n = 0 \tag{5.21}$$

The condition for a stable point (x_0, y_0) is that real parts of all roots of the characteristic equation 5.21 are negative, i.e., $\mathrm{Re}\lambda_\mathrm{j} < 0$, $(j = 1, 2, ...)$. The condition of having a limit cycle is that a pair of complex eigenvalues of the Jacobian matrix, i.e, $\lambda = \mu \pm i\omega$, crosses the imaginary axis or the $\mu = 0$ line, the eigenvalues become purely imaginary and the system loses or gains its stability. Here ω is the oscillation frequency of the periodic solution or the limit cycle.

The sign of $\mathrm{Re}\lambda_\mathrm{j}$ may be difficult to be determined directly. There are a number of criteria can help and the one I am going to discuss here is the Routh-Hurwitz theorem. It states that the characteristic equation 5.21 has all real roots if $\Delta_j > 0$ $(j = 1, 2, ..., n)$, where

$$\Delta_j = \begin{vmatrix} b_1 & 1 & 0 & 0 & ... & 0 \\ b_3 & b_2 & b_1 & 1 & ... & 0 \\ ... & & & & & \\ b_{2j-1} & b_{2j-2} & ... & & & b_j \end{vmatrix} \tag{5.22}$$

This theorem has a useful corollary to justify periodic solutions or limit cycle dynamics: the characteristic equation 5.21 has a pair of purely imaginary roots and the all the other roots negative if and only if $b_j > 0$ $(j = 1, 2..., n)$, $\Delta_n - 1 = 0$ and $\Delta_j > 0$ $(j = n - 3, n - 5, ...)$.

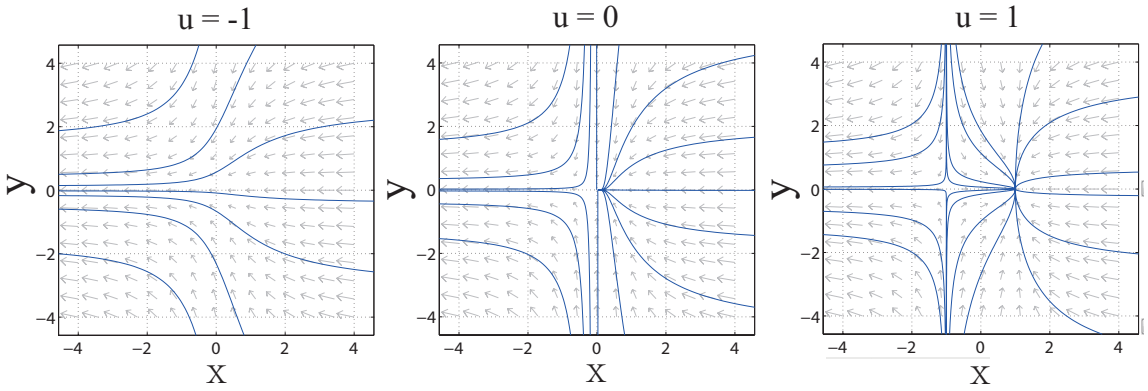

Figure 5.4 – The phase portrait of a saddle-node bifurcation based on Eqns. 5.23 and 5.24 as the parameter u increases. The phase portraits are generated using the PPlane (a Matlab toolbox).

5.3.2 Saddle-node and Hopf bifurcations

Mathematically, a bifurcation takes place when the equilibrium of a nonlinear system undergoes qualitative changes in its solution structure with one or more system parameter(s) varying, such as changes in the number or the stability of fixed points or limit cycles. Bifurcation is a signature of high nonlinearity of a system. There are various bifurcations and the two involved in this thesis the saddle-note bifurcation and the Hopf bifurcation will be introduced below.

In a saddle-note bifurcation the fixed points are created or destroyed as one parameter is varied. For instance, in the proposed model in next section, the number of fixed points changes from one to three when the input field amplitude is varied. A prototypical mathematical model of a saddle-node bifurcation in two dimensions is given by

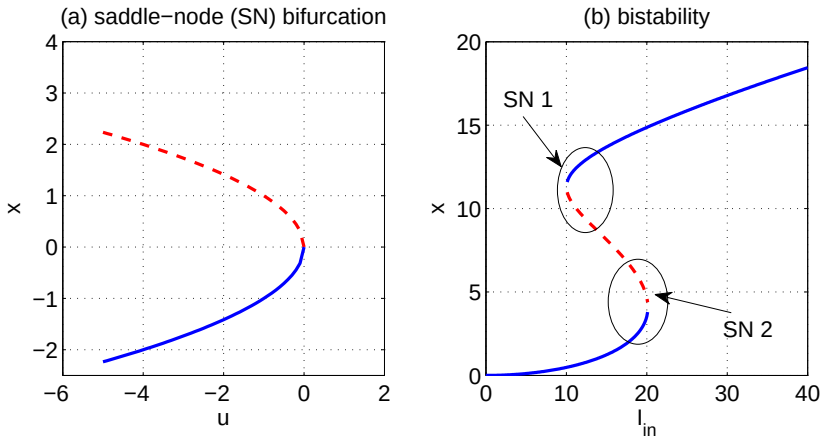

Figure 5.5 – (a) The phase diagram of a saddle-node bifurcation; (b) An example of a bistability "S" curve, which consists of two saddle-node bifurcations. "SN 1" and "SN 2" denotes two saddle-note bifurcations. Blue solid curves denote stable branches, while red dash curves denote unstable branches.

$$\dot{x} = u - x^2 \tag{5.23}$$

$$\dot{y} = -y \tag{5.24}$$

The phase portraits of the system for three different values of parameter u ($u = -1$, $u = 0$ and $u = 1$)are plotted in Fig. 5.4. At $u = -1$, there is no fixed point in the system and as u increases across the imaginary axis and becomes positive, firstly one fixed point appear

at the origin and then two fixed points appears at $(\pm\sqrt{u}, 0)$, in which $(\sqrt{u}, 0)$ is a stable node and $(-\sqrt{u}, 0)$ is a saddle. A typical bistability “S" curve or the hysteresis of a system is generated by two saddle-node bifurcations, as illustrated in Fig. 5.5.

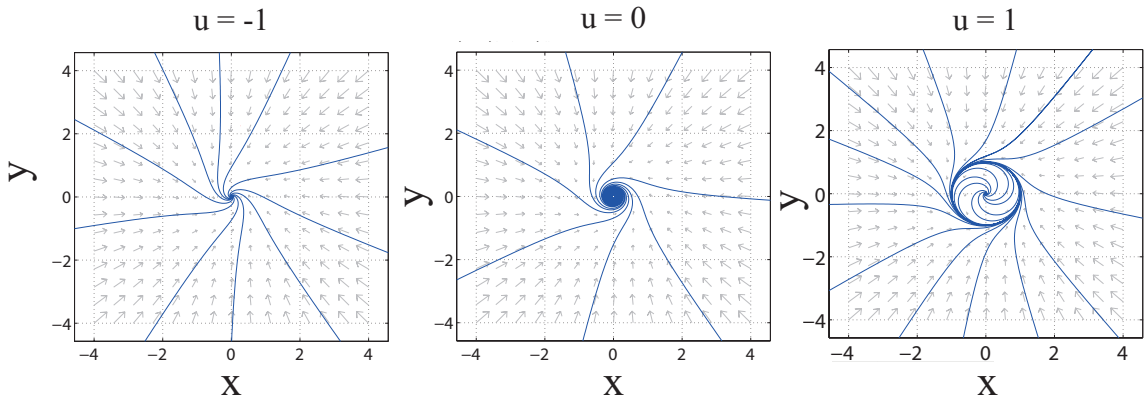

Figure 5.6 – The phase portrait of a supercritical Hopf bifurcation based on Eqns. 5.25 and 5.26 as the parameter u increases. The phase portraits are generated using PPlane (Matlabtoolbox).

A Hopf bifurcation occurs when a conjugated complex pair of roots crosses the boundary of the stability axis (or the imaginary axis). A prototypical model of Hopf bifurcation is

$$\dot{x} = a(-y + x(u - (x^2 + y^2))) \tag{5.25}$$

$$\dot{y} = a(x + y(u - (x^2 + y^2))) \tag{5.26}$$

For $a = +1$ the Hopf bifurcation is supercritical and for $a = -1$ the Hopf bifurcation is subcritical. When u varies from a negative value to a positive value, the limit cycle is changed from a stable spiral to an unstable spiral and a stable limit cycle with the radius of $\sqrt{u}$, which can be seen from phase portraits plotted in Fig. 5.6. Different from the saddle-node or other stationary bifurcations, systems with Hopf bifurcations exhibit periodicity, resulting in self-sustained oscillations of system variables or limit cycle dynamics. An interesting feature is that the oscillation frequency is irrelevant to the driving frequency. For instance, periodic behaviors are able to occur with a constant driving field in the regime of Hopf bifurcations. In an opto-mechanical system, limit cycle dynamics usually happens at blue detuning. The classic dynamics of limit cycles have been observed experimentally in Anetsberger et al. (2009); Carmon et al. (2005); Metzger et al. (2008); Zaitsev et al. (2011) and studied theoretically Khurgin et al. (2012); Marquardt et al. (2006); Zaitsev et al. (2012) and quantum

limit cycles have been investigated in Ludwig et al. (2008); Qian et al. (2012).

5.4 Nonlinear dynamics in a hybrid coupled-resonator and optomechanical system

The CRIT effect Smith et al. (2004) describes a phenomenon of the transparency of light when it passes two closely located identical ring optical resonators. This transparency comes from the interference between two pathways of the light, the Fano effect in ring resonator system.

Now I consider the situation where one of the ring resonators in a coupled-resonator optical waveguide (CROW) system is mechanically vibrating and thus the coupled optical modes and mechanical vibration mode form a joint CROW and optomechanical system. We expect that the nonlinearity induced by the vibration of the mechanical resonator causes interesting changes of the original CRIT effect and some other nonlinear behaviors in the joint CROW and optomechanical system.

5.4.1 Model

The system under consideration is shown in Figure 5.7: one ring resonator a is evanescently coupled to another ring resonator b and a waveguide on its right and left sides, respectively. The resonator b vibrates freely while the resonator a is static. The input light is sent to the system through the waveguide. The system Hamiltonian consists of three parts ($\hbar = 1$):

$$\hat{H}_{\rm sys} = \hat{H}_0 + \hat{H}_{\rm int} + \hat{H}_{\rm dri} \tag{5.27}$$

The free Hamiltonian includes the mechanical vibration mode, optical modes in ring resonators:

$$\hat{H}_0 = \frac{1}{2}\omega_m \left(\hat{x}^2 + \hat{p}^2\right) + \omega_a \hat{a}^\dagger \hat{a} + \omega_b \hat{b}^\dagger \hat{b} \tag{5.28}$$

where $\hat{x}$ and $\hat{p}$ are dimensionless position and momentum operators which satisfy $[\hat{x}, \hat{p}] = i$. ω_m is the mechanical resonance frequency and $\hat{a}^\dagger\,(\hat{a})$ and $\hat{b}^\dagger(\hat{b})$ are creation(annihilation) operators of ring resonator mode with frequency ω_a and optical whispering gallery mode with frequency ω_b, respectively. The interaction Hamiltonian is given by

$$\hat{H}_{\rm int} = -g_1 \hat{b}^\dagger \hat{b} \hat{x} + g_2 \left(\hat{b}\hat{a}^\dagger + \hat{a}\hat{b}^\dagger \right), \tag{5.29}$$

The first term is the interaction between the optical resonator mode b and mechanical mode with coupling strength g_1 and the second term is the coupling between the two optical resonators with the coupling constant g_2. The Hamiltonian for the driving term is

$$\hat{H}_{\rm dri} = i\sqrt{\kappa_{ex}} \left(S_{in} e^{-i\omega_{in} t} \hat{a}^\dagger - S_{in}^* e^{i\omega_{in} t} \hat{a} \right) \tag{5.30}$$

where S_{in} is the amplitude of the driving laser with frequency ω_{in} and κ_{ex} is the coupling between the waveguide and the optical resonator a.

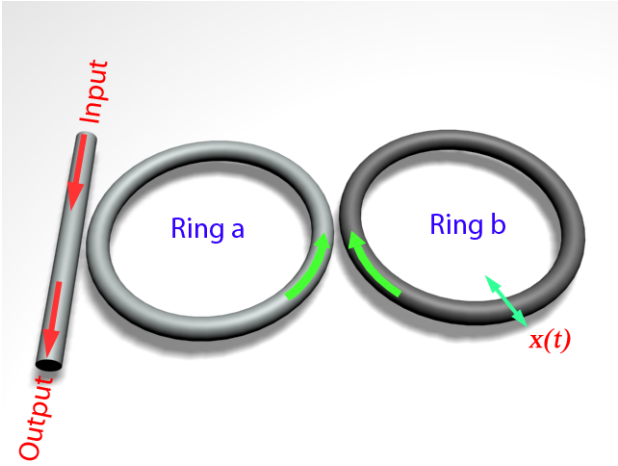

Figure 5.7 – Schematic diagram for the coupled-resonator waveguide system with optomechanical coupling.

In the frame rotating at ω_{in}, we obtain the motion equations for the expectation values of

the system operators:

$$\frac{d\left\langle \hat{a}\right\rangle }{dt} = -\left(i\Delta+\kappa_1+\frac{\kappa_{ex}}{2}\right)\left\langle \hat{a}\right\rangle - ig_2\left\langle \hat{b}\right\rangle + \sqrt{\kappa_{ex}}S_{in} \tag{5.31}$$

$$\frac{d\left\langle \hat{b}\right\rangle }{dt} = -\left(i\left(\Delta+\delta\right)+\kappa_2\right)\left\langle \hat{b}\right\rangle + ig_1\left\langle \hat{x}\right\rangle \left\langle \hat{b}\right\rangle - ig_2\left\langle \hat{a}\right\rangle \tag{5.32}$$

$$\frac{d\left\langle \hat{p}\right\rangle }{dt} = -\gamma_m\left\langle \hat{p}\right\rangle - \omega_m\left\langle \hat{x}\right\rangle + g_1\left\langle \hat{b}^{\dagger}\hat{b}\right\rangle + \xi_m\left(t\right) \tag{5.33}$$

$$\frac{d\left\langle \hat{x}\right\rangle }{dt} = \omega_m\left\langle \hat{p}\right\rangle . \tag{5.34}$$

where $\Delta=\omega_a-\omega_{in}$ is the detuning between optical resonator and laser field, $\delta=\omega_b-\omega_a$ is the frequency difference between two optical resonators. Here we phenomenologically introduce the damping rates κ_1 and κ_2 of the two ring resonator modes. The mechanical mode is affected by a viscous force with the damping rate γ_m and by a Brownian stochastic force with noise $\xi_m\left(t\right)$, which obeys the correlation $\left\langle \xi_m\left(t\right)\xi_m\left(t'\right)\right\rangle = 2m\gamma_m k_B T_0/(\hbar\omega_m)\delta\left(t-t'\right)$ with Bolzman constant k_B and environmental temperature T_0.

5.4.2 Stability analysis

When the system is strongly driven, it can be characterized by the semiclassical steady-state solution with large amplitudes for both mechanical and cavity modes. In the following, we denote y_s as the steady state mean value of the operator $\hat{y}$. The steady-state solutions can be obtained by setting the time derivatives to zero and factorizing the expectation values. Here we present the steady-state value equation for the equilibrium position:

$$\left|Ag_1\right|^2 x_s^3 + ig_1\left(BA^*-AB^*\right)x_s^2 + \left|B\right|^2 x_s - \frac{g_1 g_2^2\kappa_{ex}I_{in}}{\omega_m} = 0, \tag{5.35}$$

where parameters $A=i\Delta+(\kappa_1+\kappa_{ex}/2)$, $B=A\left(i\left(\Delta+\delta\right)+\kappa_2\right)+g_2^2$ and the incident light intensity $I_{in}=\left|S_{in}\right|^2$. Eq. (5.35) is a cubic equation for equilibrium position x_s, therefore there are at most three real roots.

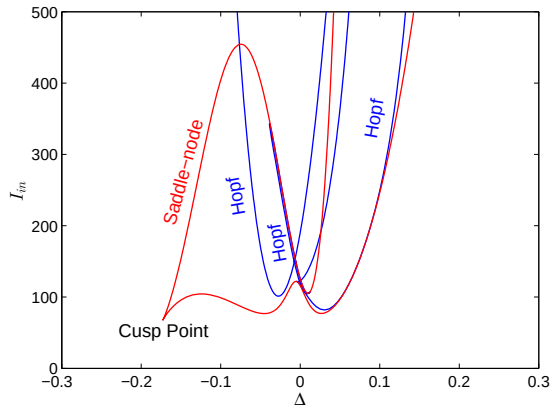

Figure 5.8 – The bifurcation diagram in the (Δ, I_{in}) plane. The parameters are $g_2 = 0.04$, $k_1 = 0.0001$, $k_2 = 0.02$, $k_{ex} = 0.04$, $\omega_m = 1$, $\delta = 0.2$, $g_1 = 0.01$ and $\gamma_m = 0.001$.

The steady state optical mode in the ring resonator a is also found to be

$$a_s = \frac{\sqrt{\kappa_{ex}}}{\left(i\Delta + \kappa_1 + \kappa_{ex}/2 + \frac{g_2^2}{i(\Delta+\delta-g_1 x_s)+\kappa_2}\right)} S_{in}, \tag{5.36}$$

According to the input-output relation $S_{out} = S_{in} - \sqrt{\kappa_{ex}} a_s$, the output light is written as

$$S_{out} = S_{in}\left(1 - \frac{\kappa_{ex}}{\left(i\Delta + \kappa_1 + \kappa_{ex}/2 + \frac{g_1^2}{i(\Delta+\delta-g_1 x_s)+\kappa_2}\right)}\right) \tag{5.37}$$

Hence the transmission rate of light is expressed as

$$\begin{aligned} T &= \left|\frac{S_{out}}{S_{in}}\right|^2 \\ &= |1 - C|^2 \end{aligned} \tag{5.38}$$

where

$$C = \frac{\kappa_{ex}}{i\Delta + \kappa_1 + \kappa_{ex}/2 + \frac{g_2^2}{i(\Delta+\delta-g_1 x_s)+\kappa_2}}. \tag{5.39}$$

Then, we turn to study the dynamics of the quantum fluctuations around the steady state by expanding the operators around its stable-state value as $\hat{y} = \hat{y}_s + \delta\hat{y}$, and introducing the field quadrature $\delta X_c = \left(\delta\hat{c} + \delta\hat{c}^\dagger\right)/\sqrt{2}$ and $\delta Y_c = \left(\delta\hat{c} - \delta\hat{c}^\dagger\right)/\left(\sqrt{2}i\right)$ $(\hat{c} = \hat{a}, \hat{b}, S_{in})$. The

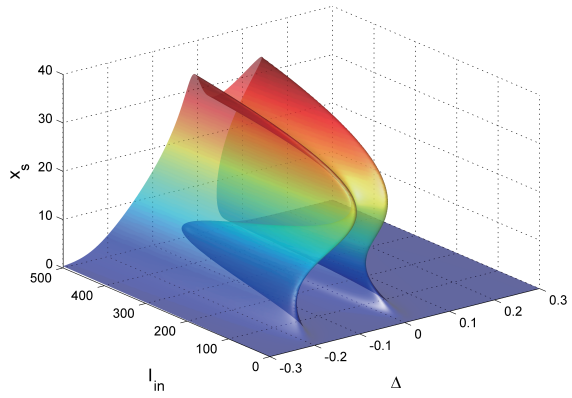

Figure 5.9 – Equilibrium surface of position of resonator in three dimensions. The parameters are the same as in Figure 5.8

linearized motion equations are then written as

$$\dot{y}(t) = Jy(t) + \xi(t) \tag{5.40}$$

where $y(t) = [\delta X_a, \delta Y_a, \delta X_b, \delta Y_b, \delta p, \delta x]^T$, the noise term $\xi(t) = \left[\sqrt{\kappa_{ex}} X_{in}, \sqrt{\kappa_{ex}} Y_{in}, 0, 0, 0, \xi_m\right]^T$, and the Jacobian matrix is given by

$$J = \begin{pmatrix} -\kappa & \Delta & 0 & g_2 & 0 & 0 \\ -\Delta & -\kappa & -g_2 & 0 & 0 & 0 \\ 0 & g_2 & -\kappa_2 & \Delta_{eff} & 0 & -g_1 Y_b \\ -g_2 & 0 & -\Delta_{eff} & -\kappa_2 & 0 & g_1 X_b \\ 0 & 0 & g_1 X_b & g_1 Y_b & -\gamma_m & -\omega_m \\ 0 & 0 & 0 & 0 & \omega_m & 0 \end{pmatrix}, \tag{5.41}$$

where $\kappa = \kappa_1 + \kappa_{ex}/2$, $\Delta_{eff} = \Delta + \delta - g_1 x_s$, $X_b = (b_s + b_s^*)/\sqrt{2}$, and $Y_b = (b_s - b_s^*)/\left(\sqrt{2}i\right)$. The steady-state solution is stable if all the eigenvalues of the Jacobian matrix have negative real parts. It can be verified with the help of the Routh-Hurwitz criterion Jeffrey and Zwillinger (2007) to determine the stable and unstable region on the parameters space.

Figure 5.8 provides the bifurcation diagram in the parameters space (Δ, I_{in}). The whole plane is divided into several stable and unstable regions, which are determined by the Hopf bifurcation and the saddle node bifurcation. Figure 5.9 presents the 3D equilibrium surface

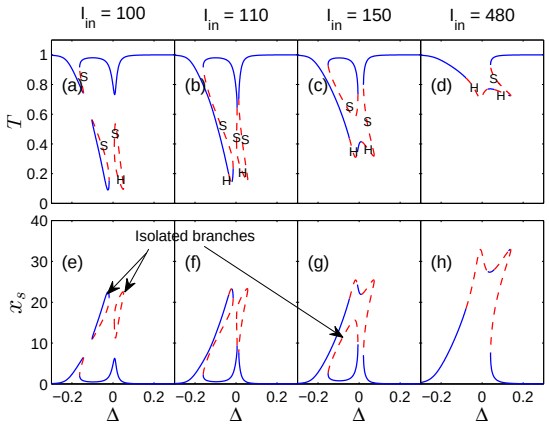

Figure 5.10 – Top panel are the transmission rates of the light with different input intensities and the bottom panel are the corresponding mechanical steady-state positions, cross sections of the folded surface in Fig. 5.9. The parameters are the same as in the Figure 2. S denotes the saddle-node bifurcation and H denotes the Hopf bifurcation.

of mechanical resonator position against the input intensity I_{in} and the detuning Δ. Unlike the usual steady-state surface in a cusp catastrophe model, Figure 5.9 demonstrates a complicated state surface, which results from the complicated nonlinear function of I_{in} and Δ in Eq. (5.35).

5.4.3 Bistability in the transparency window of CRIT

To examine the stability properties of the system, the cross sections of the folded surface with different input intensities are shown in the figure 5.10. When $I_{in} = 100$, there are three unstable regions. Except for a bistable branch on the main continuous curve, two isolated branches (isolas) are above the lower main branch. When the initial equilibrium position of mechanical resonator is on the isolated branches and the detuning is continuously swept in an increasing or decreasing manner, the equilibrium position will jump to the lower main branch, but not vice versa. This unique feature is a non-hysteretic multi-stability, which may be used as unidirectional switch. For a larger input intensity, $I_{in} = 110$, one isola merges with the bistable branch and another one becomes a mushroom structure (Figure 5.10(f)). When further increasing the input intensity, the top parts of the normal bistable and the mushroom-like branches merge, which allow two-way switching, and another isola forms under the main branch (Figure 5.10(g)). The size of isola becomes smaller and

smaller, and finally vanishes. In terms of the transmission rate, from the Figure 5.10(a-d) we see that there are also isolas structure on the transmission curves, similar to the case of equilibrium position of the mechanical mode. This means we can observe and study the isolas structure in our system via photoelectric detector.

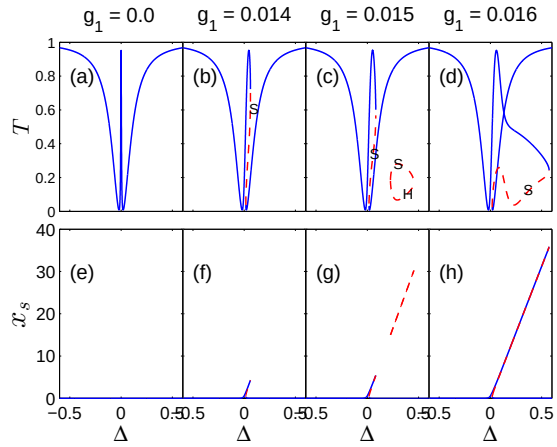

Figure 5.11 – Top panel is the transmission rate T as a function of detuning Δ and bottom panel is the corresponding equilibrium mechanical position. The parameters are $\delta = 0$, $\omega_m = 1$, $g_2 = 0.02$, $\kappa_1 = 0.06$, $\kappa_2 = 0.0001$, $\kappa_{ex} = 0.1$, $I_{in} = 1$ and $\gamma_m = 0.001$

Next the effect of nonlinearity induced by the mechanical resonator on the coupled resonator induced transparency is discussed. Different from previous situation, here we set the frequencies of two ring resonator identical. Figure 5.11(a) shows the transmission versus the detuning with different optomechanical coupling strengths. Obviously, when the optomechanical coupling strength vanishes, there is a symmetric narrow transparency window in the middle of transmission spectrum (blue curve in Figure 5.11(a)), which is the CRIT effect. As the coupling g_1 increases, the transparency window bends towards right side and the transmission becomes bistable (red curve). With further increasing g_1, the transparency window becomes severely distorted and even intersects with itself. More interesting, for certain g_1, the distorted transparency window breaks into a mother branch and a isolated branch. In fact, we find that the nonlinearity has more influence on the transparency window region but less on the other region.

5.4.4 Weak impulsive force detection based on CRIT

Figure 5.11 in the last section has shown that the CRIT transparency window is narrow and mechanical motion dependent. Bistability also be observed in the transparency window with strong optomechanical coupling. Motivated by this, here we propose to detect a weak force acting on the mechanical motion by measuring the transmission of the light. Weak force detection using opto-mechanical systems have been studied in Gavartin et al. (2012); Moser et al. (2013); Pontin et al. (2014).

Assuming that an external force f acts on the vibrating ring resonator, the Hamiltonian of the system becomes

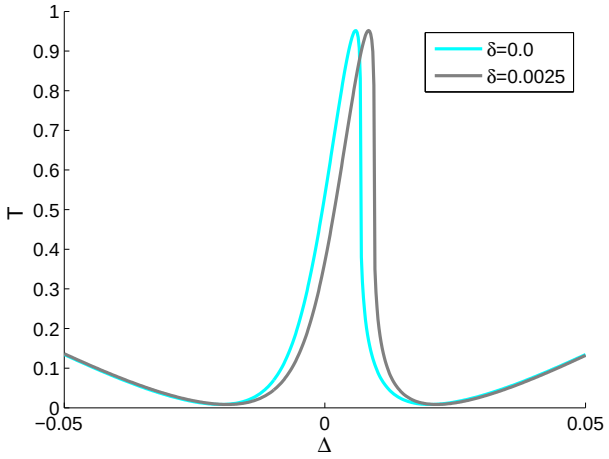

Figure 5.12 – The transparency window at different detuning δ. The parameters are $\omega_m = 1$, $\Delta = 0$, $g_1 = 0.005$, $g_2 = 0.02$, $\kappa_1 = 0.06$, $\kappa_2 = 0.0001$, $\kappa_{ex} = 0.1$, $I_{in} = 1$ and $\gamma_m = 0.001$

$$\begin{aligned} \hat{H}_0 &= \frac{1}{2}\omega_m\left(\hat{x}^2+\hat{p}^2\right)+\omega_a\hat{a}^\dagger\hat{a}+\omega_b\hat{b}^\dagger\hat{b} \\ &\quad -g_1\hat{b}^\dagger\hat{b}\hat{x}+g_2\left(\hat{b}\hat{a}^\dagger+\hat{a}\hat{b}^\dagger\right)+f\hat{x} \end{aligned} \tag{5.42}$$

The last term describes the coupling between the external force and mechanical vibration mode.

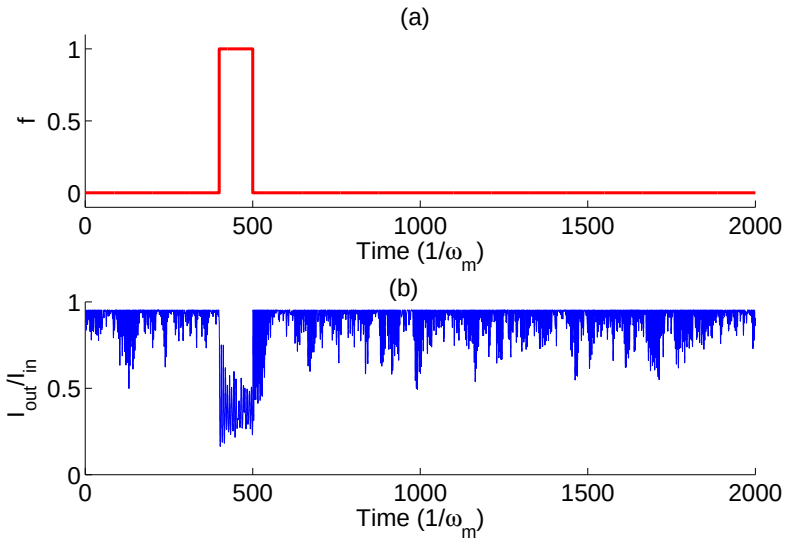

Figure 5.13 – (a) The incident impulsive force $f = f_0(400\omega_m^{-1} < t < 500\omega_m^{-1})$; (b) One trajectory of the time evolution of the output field intensity with the impulsive force acting on the system. The parameters are $f_0 = 1$, $k_B T_0 = 10\hbar\omega_m$, $\delta = 0.006$, $\Delta = 0$, $\omega_m = 1$, $g_1 = 0.005$, $g_2 = 0.02$, $\kappa_1 = 0.06$, $\kappa_2 = 0.0001$, $\kappa_{ex} = 0.1$, $I_{in} = 1$ and $\gamma_m = 0.1$

Defining $\hat{x'} = \hat{x} + \frac{f}{\omega_m}$, the Hamiltonian (5.42) becomes

$$\begin{aligned} \hat{H} &= \frac{1}{2}\omega_m\left(\hat{x'}^2 + \hat{p}^2\right) + \Delta\hat{a}^\dagger\hat{a} + (\Delta + \delta_{\text{eff}})\,\hat{b}^\dagger\hat{b} \\ &\quad -g_1\hat{b}^\dagger\hat{b}\hat{x'} + g_2\left(\hat{b}\hat{a}^\dagger + \hat{a}\hat{b}^\dagger\right), \end{aligned} \tag{5.43}$$

where $\delta_{\text{eff}} = \delta + \frac{g_1 f}{\omega_m}$. One can see that Hamiltonian (5.43) and (5.27) have the same mathematical structure. By comparison, applying an external force is equivalent to adding an additional frequency shift on the optical field b, or adding a change in δ. As shown in Figure 5.12, a slight change in δ will lead to a significant shift in the CRIT window and therefore the transmitted field intensity will have a detectable change. Suppose that a weak impulsive force $f(t)$ acts on the mechanical mode, then the force induced difference in the transmitted field can be well distinguished as shown in Figure 5.13. The relation between the transmitted field intensity and the force strength is presented in Figure 5.14 and there is a quite large quasi-linear regime in the relation.

As defined in Mancini and Tombesi (2003), the minimal detectable force can be obtained

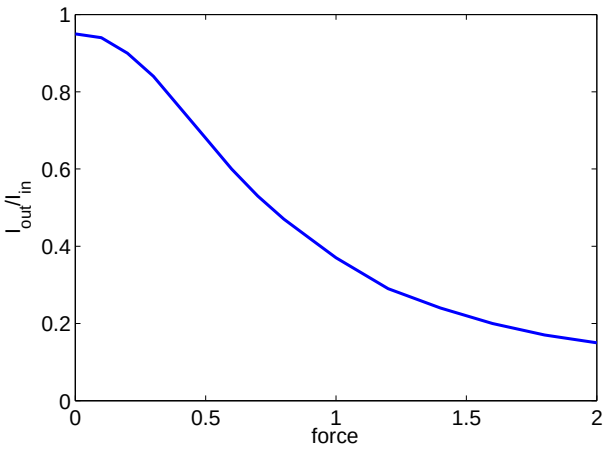

Figure 5.14 – The normalized output field intensity as a function of incident force. The parameters are $\delta = 0.006$, $\Delta = 0$, $\omega_m = 1$, $g_1 = 0.005$, $g_2 = 0.02$, $\kappa_1 = 0.06$, $\kappa_2 = 0.0001$, $\kappa_{ex} = 0.1$, $I_{in} = 1$ and $\gamma_m = 0.1$

from the relation

$$\mathrm{SNR} = \frac{\mathcal{S}f}{\sqrt{\mathcal{N}}} \leq 1 \tag{5.44}$$

and the minimal detectable force

$$f_{\min} = \frac{\sqrt{\mathcal{N}}}{\mathcal{S}} \tag{5.45}$$

Using Eq. 5.45, the minimal detectable force can be estimated based on Fig. 5.13 at a fixed temperature and a fixed measurement time. Here we use a set of typical parameters to estimate the sensitivity of impulsive force detection: $\omega_m \sim 10$ MHz, $m \sim 1$ pg, $\gamma_m \sim 1$ kHz, the environment temperature $T_0 \sim 10$ mK, and the measurement time $T_m \sim 200\omega_m^{-1}$. Under these conditions, the minimal force can be detected is around 10^{-14} N·Hz$^{-1/2}$.

5.4.5 Limit cycles and periodic outputs

This section shows the limit cycle dynamics of the system and it is found that limit cycles are insensitive to thermal noise. As mentioned before, limit cycles often appear in systems with Hopf bifurcations. Recall the bifurcation diagram (Fig. 5.9), both saddle-node bifurcation and Hopf bifurcation exist in the regime of I_{in} above 100 and thus we explore limit cycle

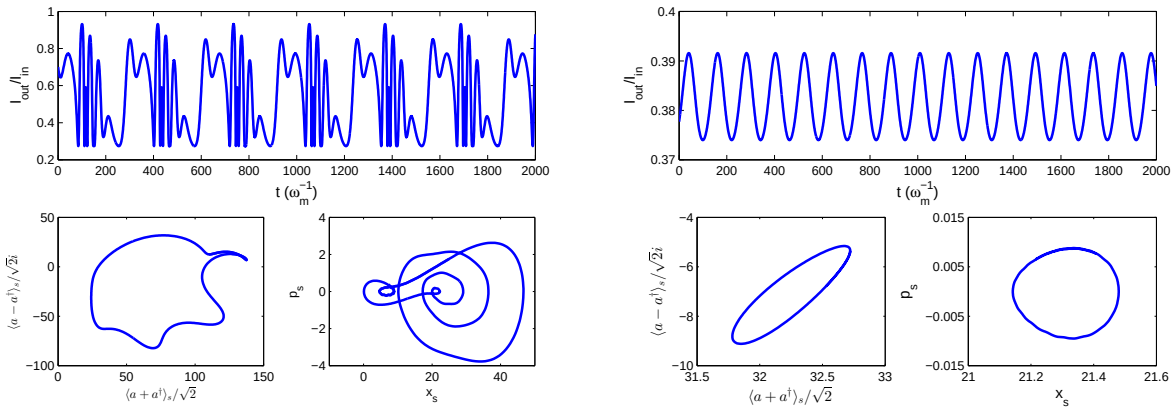

Figure 5.15 – The output of the optical field with input intensities (left) $I_{in} = 130$ and (right) $I_{in} = 138$. $X_a = \langle \hat{a} + \hat{a}^\dagger \rangle$ and $Y_a = -i \langle \hat{a} - \hat{a}^\dagger \rangle$. The parameters are: $g_2 = 0.04$, $k_1 = 0.0001$, $k_2 = 0.02$, $k_{ex} = 0.04$, $\omega_m = 1$, $\Delta = 0.01$, $\delta = 0.2$, $g_1 = 0.01$ and $\gamma_m = 0.1$.

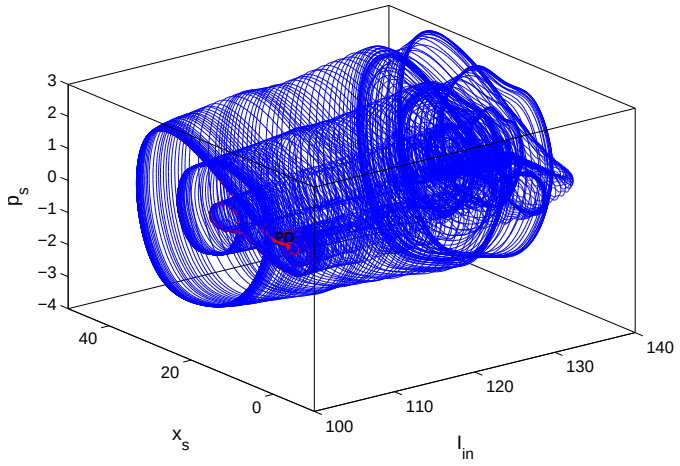

Figure 5.16 – The limit cycle of the mechanical mode in three-dimensional space. The parameters are: $g_2 = 0.04$, $k_1 = 0.0001$, $k_2 = 0.02$, $k_{ex} = 0.04$, $\omega_m = 1$, $\Delta = 0.01$, $\delta = 0.2$, $g_1 = 0.01$ and $\gamma_m = 0.1$.

dynamics in this strong driving regime.

Figure 5.15 presents the limit cycle dynamics or the self-sustained oscillations of the normalized output optical field intensity I_{out}/I_{in} and the corresponding trajectories of one resonator field and the steady-state mechanical motion at two different driving field intensity. At $I_{in} = 130$, the output field intensity oscillates with one fast and one slow frequencies, i.e., within one slow oscillation period the variable has a few cycles of fast oscillation, and the trajectories in the phase space have relatively complicated structure; while at $I_{in} = 138$

the oscillations of the output field intensity is a standard sine curve and the corresponding trajectories in the phase space are ellipses. To see the dependence of limit cycles on the input field intensity I_{in}, the limit cycle is plotted in three dimensions (the $x-p-I_{in}$ space) in Figure 5.16. Thermal noises are inevitable in a finite-temperature opto-mechanical system.

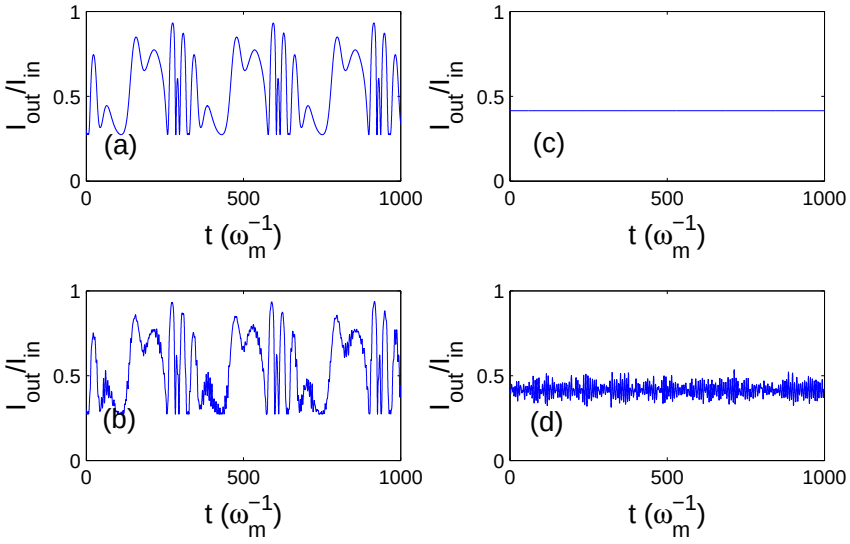

Figure 5.17 – The influence of the mechanical thermal noise on the output intensity of the field. (a) and (c) the time evolution of normalized output field intensity in the absence of the thermal noise for the limit cycle and the normal fixed point, respectively. (b) and (d) respond to the counterparts of (a) and (b) with the thermal noise $k_BT = 300\hbar\omega_m$. $g_2 = 0.04$, $k_1 = 0.0001$, $k_2 = 0.02$, $k_{ex} = 0.04$, $\omega_m = 1$, $\delta = 0.2$, $g_1 = 0.01$, $\gamma_m = 0.05$ and $I_{in} = 130$ for (a)(b) and $I_{in} = 150$ for (c)(d).

Now we study the effect of thermal noises on the limit cycle dynamics. Figure 5.17 compares the output fields with mechanical Brownian noise between a limit cycle (a-b) and a fixed point (c-d). The tuning from a limit cycle to a fixed point is realized simply by increasing I_{in} from 130 to 150. It is clear that for the same amount of thermal noises the output state of the limit cycle is much less noisy than that of the fixed point, The noise suppression of limit cycles have been discussed in Kenig et al. (2012); Simpson et al. (2014). This property suggested this system can be used as an extra stable oscillation generator.

5.5 Conclusion

In conclusion, we investigated a system consisting of two coupled ring resonators with one of resonators freely oscillating. This system combines the coupled-resonator induced transparency effect and the optomechanical nonlinearity. It is observed that the light transmission and the equilibrium position of the mechanical resonator exhibit bistability in different regimes. Isolas and limit cycles emerge in the system. The isolas or the isolated-branch solutions allow the one-way switch of system outputs and the limit cycles show its insensitivity to thermal noise of the mechanics. More importantly, the transparency window of the CRIT effect is dramatically affected by the opto-mechanical nonlinearity and it is shown that the system is a good platform of detecting weak impulsive forces based on the bistable narrow transparency window.

Chapter 6

Conclusions and outlook

6.1 Conclusions

The results of this thesis include two main topics: single microwave photon detection using transmons and bifurcations of a coupled-resonator and optomechanical system. The first topic was covered in Chapters 3-4 and the second topic was discussed in Chapter 5.

Quantum superconducting devices provide strong interaction between “atoms" and fields, which enable single superconducting “atoms" to show nonlinear optics phenomena, such as EIT Dutton et al. (2006) and cross-Kerr effect Hoi et al. (2013). In Hoi et al. (2013) 20 degree cross-Kerr phase shift of a microwave field was observed in a single transmon system. This work motivated our first attempt towards a single microwave photon detector–using a transmon provided cross-Kerr nonlinearity to detect the photon number in a traveling microwave field through homodyne measurements of another field. We used continuous quantum trajectories to simulate the homodyne detection with inclusion of “atomic" spontaneous emissions and the shot noise. The measurement results turned out to be negative, however, an important limitation in photon counting based on cross-Kerr mechanism was explored, that is, the saturation of “atomic" transitions limits the SNR of the cross-Kerr-type photon detection. This was shown by consistent results from stochastic simulations and analytical solutions.

To overcome to the limitation in the first work, a subsequent scheme was presented with largely enhanced SNR. The enhancement comes from the adopt of a probe cavity, which improves the SNR from 0.5 to 1.2, compared to the first work. Furthermore, by cascading more transmon-cavity units, the detection efficiency could be further improved. With only

two transmons, the SNR is increased to about 1.7 and the correct probability to distinguish a single photon from the vacuum reaches 90$\%$. In this scheme photons are not absorbed in the detection process so that they can be repeatedly measured or used for further applications. In addition, we also showed that as the photon measurement efficiency gets higher, the signal photon pulse becomes more distorted and the system coherence reduces more rapidly.

Another work contributed to this thesis is about bifurcations in a CRIT system with optomechanical coupling. The system dynamics were analyzed in the semi-classical picture. The presence of the coupling between two resonators and the optomechanical coupling lead to saddle-node bifurcation and Hopf bifurcation occurring in the system and consequently bistabilities and limit cycles of system variables were observed. Moreover, the transparency window of the CRIT is sensitive to the optomechanical nonlinearity and detunings, based on which the system was shown to be able to serve as a good weak impulsive force sensor.

6.2 Further work

Finally, I would like to discuss about future directions relevant to the context of the thesis and some potential extension work based on the preceding investigations.

- Photon-number-resolving detector at microwave frequencies.

  The work presented in this thesis on single-photon counting was focused on the discrimination between $n = 0$ and $n = 1$, that is, the detector tells whether there is a photon coming or not. Sometimes, to know whether a pulse contains one or more photons is necessary, for instance, for the situation of faint coherent fields as single photon sources, the probability of having two-photon state might not be negligible and in this situation a photon-number-resolving detector would be needed.

- Bifurcation detector.

  Bifurcations have been applied to qubit readout and one example is the single-shot readout of superconducting qubit states using bifurcation provided by a Josephson

parametric amplifier Mallet et al. (2009). Inspired by this, here we want to use bifurcations to detect a single microwave photon. The system is the same as the transmon-cavity detection system discussed in Chapter 4 expect for exchanged positions of probe and signal tones. The cavity is coherently driven and its central frequency is resonant with 0-1 transition of the transmon. We assume that the driving is so strong that the system enters the bistability regime. Around the critical point, the system is very sensitive even to small perturbations. Therefore, when the system is tuned to the vicinity of the critical point of the system bistability, the presence of a single photon with its frequency resonate with the transmon 1-2 transition would cause the switch from one stable branch to the other and hence a significant change of the system output would be detected.

- Improving single microwave photon detection using time-dependent coefficients.

  A recent work Pierre et al. (2014) shows that it is possible to tune the coupling between a superconducting resonator and a transmission line via controlling the flux in a SQUID loop. Motivated by this work, I suggest replace the constant cavity decay rate κ by a time-dependent cavity decay rate $\kappa(t)$ in the detection scheme presented in Chapter 4, which could be realized by adding the SQUID to one boundary of the probe cavity and applying a time-dependent flux. By dynamically tuning $\kappa(t)$, I expect the efficiency of the single microwave photon detection will be improved.

- Compensation of pulse distortions due to the measurement.

  In Chapter 4, we have explore a fundamental principle of quantum measurement: the higher the measurement efficiency, the greater is the decoherence and pulse distortions. These effects do not change photon number measurement results but pulse distortions might cause mismatching between the reference pulse and the measured signal pulse, which will lead to a reduced visibility in an interferometer. Therefore, it is important to compensate measurement induced pulse distortion effect. One potential solution is to use an inverse process of the previous nonlinear interaction used in the measurement.

- Using limit cycle dynamics for detecting weak external disturbances and limit cycles in the quantum regime.

In Chapter 5, we have shown that limit cycle dynamics are insensitive to thermal noises and the switch between limit cycles and a stable fixed point can be realized by simply tuning the input field power and other parameters. Based on these, limit cycle dynamics might be useful for detecting the presence of an external perturbation, such as a weak force or a weak magnetic field. Besides, it is interesting to study limit cycles in quantum regimes, in particular, to study the effect of quantum noises on limit cycles.

- CRIT with two vibrating resonators.

  In the proposed scheme in Chapter 5, one resonator in the original CRIT set-up is mechanically vibrating and the system has six dimensions. If both resonators of the CRIT system vibrate, the system will have eight dimensions, which may results in higher-order nonlinearities and a more interesting bifurcation diagram.

References

Baleegh Abdo, Katrina Sliwa, S. Shankar, Michael Hatridge, Luigi Frunzio, Robert Schoelkopf, and Michel Devoret. Josephson directional amplifier for quantum measurement of superconducting circuits. *Phys. Rev. Lett.*, 112:167701, Apr 2014. doi: 10.1103/PhysRevLett.112.167701. 77

Marius A Albota and Franco NC Wong. Efficient single-photon counting at 1.55 μm by means of frequency upconversion. *Optics letters*, 29(13):1449–1451, 2004. 5

Samuel Aldana, Christoph Bruder, and Andreas Nunnenkamp. Equivalence between an optomechanical system and a kerr medium. *Physical Review A*, 88(4):043826, 2013. 93

Georg Anetsberger, Olivier Arcizet, Quirin P Unterreithmeier, Rémi Rivière, Albert Schliesser, Eva Maria Weig, Jörg Peter Kotthaus, and Tobias J Kippenberg. Near-field cavity optomechanics with nanomechanical oscillators. *Nature Physics*, 5(12):909–914, 2009. 97

Markus Ansmann, H Wang, Radoslaw C Bialczak, Max Hofheinz, Erik Lucero, M Neeley, AD O'Connell, D Sank, M Weides, J Wenner, et al. Violation of bell's inequality in josephson phase qubits. *Nature*, 461(7263):504–506, 2009. 8

Alain Aspect, Philippe Grangier, and Gérard Roger. Experimental tests of realistic local theories via bell's theorem. *Physical review letters*, 47(7):460, 1981. 5

Ben Q Baragiola, Robert L Cook, Agata M Brańczyk, and Joshua Combes. N-photon wave packets interacting with an arbitrary quantum system. *Physical Review A*, 86(1):013811, 2012. ..... 35, 39, 54, 135

Alexios Beveratos, Rosa Brouri, Thierry Gacoin, André Villing, Jean-Philippe Poizat, and Philippe Grangier. Single photon quantum cryptography. *Physical review letters*, 89(18): 187901, 2002a. 4

Alexios Beveratos, Rosa Brouri, Thierry Gacoin, André Villing, Jean-Philippe Poizat, and Philippe Grangier. Single photon quantum cryptography. *Physical review letters*, 89(18): 187901, 2002b. 5

Lev S Bishop, JM Chow, Jens Koch, AA Houck, MH Devoret, E Thuneberg, SM Girvin, and RJ Schoelkopf. Nonlinear response of the vacuum rabi resonance. *Nature Physics*, 5(2): 105–109, 2009. 15

David G Blair. *The detection of gravitational waves*. Cambridge university press, 2005. 90

Alexandre Blais, Ren-Shou Huang, Andreas Wallraff, SM Girvin, and R Jun Schoelkopf. Cavity quantum electrodynamics for superconducting electrical circuits: An architecture for quantum computation. *Physical Review A*, 69(6):062320, 2004. 8

Mark F Bocko and Roberto Onofrio. On the measurement of a weak classical force coupled to a harmonic oscillator: experimental progress. *Reviews of Modern Physics*, 68(3):755, 1996. 34

Vincent Bouchiat, D Vion, P Joyez, D Esteve, and MH Devoret. Quantum coherence with a single cooper pair. *Physica Scripta*, 1998(T76):165, 1998. 14

Robert W Boyd. *Nonlinear optics*. Academic press, 2003. . . . . 42, 43

D Bozyigit, C Lang, L Steffen, JM Fink, C Eichler, M Baur, R Bianchetti, PJ Leek, S Filipp, MP Da Silva, et al. Antibunching of microwave-frequency photons observed in correlation measurements using linear detectors. *Nature Physics*, 7(2):154–158, 2011. 6

Vladimir Borisovich Braginskii and Anatoliĭ Manukin. Measurement of weak forces in physics experiments. 90

Vladimir B Braginsky and Braginskiĭ. *Quantum measurement*. 34

Vladimir B Braginsky and F Ya Khalili. Quantum nondemolition measurements: the route from toys to tools. *Reviews of Modern Physics*, 68(1):1, 1996. 34

Heinz-Peter Breuer and Francesco Petruccione. *The theory of open quantum systems*. Oxford university press, 2002. 20

M. Brune, E. Hagley, J. Dreyer, X. Maitre, A. Maali, C. Wunderlich, J. M. Raimond, and S. Haroche. *Phys. Rev. Lett.*, 77:4887–4890, Dec 1996. doi: $10.1103/\mathrm{PhysRevLett.77.4887}$. 82

H. J. Carmichael. Quantum trajectory theory for cascaded open systems. *Phys. Rev. Lett.*, 70:2273–2276, Apr 1993a. 70

HJ Carmichael. Quantum trajectory theory for cascaded open systems. *Physical review letters*, 70(15):2273–2276, 1993b. 36, 37

Tal Carmon, Hossein Rokhsari, Lan Yang, Tobias J Kippenberg, and Kerry J Vahala. Temporal behavior of radiation-pressure-induced vibrations of an optical microcavity phonon mode. *Physical Review Letters*, 94(22):223902, 2005. 97

Tal Carmon, MC Cross, and Kerry J Vahala. Chaotic quivering of micron-scaled on-chip resonators excited by centrifugal optical pressure. *Physical review letters*, 98(16):167203, 2007. 93

Wen-Hao Chang, Wen-Yen Chen, Hsiang-Szu Chang, Tung-Po Hsieh, Jen-Inn Chyi, and Tzu-Min Hsu. Efficient single-photon sources based on low-density quantum dots in photonic-crystal nanocavities. *Physical review letters*, 96(11):117401, 2006. 5

Y.-F. Chen, D. Hover, S. Sendelbach, L. Maurer, S. T. Merkel, E. J. Pritchett, F. K. Wilhelm, and R. McDermott. Microwave photon counter based on josephson junctions. *Phys. Rev. Lett.*, 107:217401, Nov 2011. doi: $10.1103/\mathrm{PhysRevLett.107.217401}$. 6, 68

Yong-Fan Chen, Chang-Yi Wang, Shih-Hao Wang, and Ite A. Yu. Low-light-level cross-phase-modulation based on stored light pulses. *Phys. Rev. Lett.*, 96:043603, Feb 2006. doi: $10.1103/\mathrm{PhysRevLett.96.043603}$. 51

L Childress, AS Sørensen, and MD Lukin. Mesoscopic cavity quantum electrodynamics with quantum dots. *Physical Review A*, 69(4):042302, 2004. 8

Christopher Chudzicki, Isaac L Chuang, and Jeffrey H Shapiro. Deterministic and cascadable conditional phase gate for photonic qubits. *Physical Review A*, 87(4):042325, 2013. 50, 82

John Clarke and Alex I Braginski. The squid handbook. 2004. 10

John Clarke and Frank K Wilhelm. Superconducting quantum bits. *Nature*, 453(7198): 1031–1042, 2008. 10

Claude Cohen-Tannoudji and Serge Reynaud. Dressed-atom description of resonance fluorescence and absorption spectra of a multi-level atom in an intense laser beam. *Journal of Physics B: Atomic and Molecular Physics*, 10(3):345, 1977. 65

Audrey Cottet. Implementation of a quantum bit in a superconducting circuit. *PhD thesisUniversité Paris VI*, 2002. 14

ZJ Deng, Q Xie, CW Wu, and WL Yang. Storage of arbitrary two-charge-qubit states in a single rb 87 cold-atom ensemble. *Physical Review A*, 82(3):034306, 2010. 8

MH Devoret, Steven Girvin, and Robert Schoelkopf. Circuit-qed: How strong can the coupling between a josephson junction atom and a transmission line resonator be? *Annalen der Physik*, 16(10-11):767–779, 2007. 50

Michel H Devoret. Quantum fluctuations in electrical circuits. *Les Houches, Session LXIII*, 1995. ..... 7, 8

Ying Dong, Jinwu Ye, and Han Pu. Multistability in an optomechanical system with a two-component bose-einstein condensate. *Physical Review A*, 83(3):031608, 2011. 93

PD Drummond and DF Walls. Quantum theory of optical bistability. i. nonlinear polarisability model. *Journal of Physics A: Mathematical and General*, 13(2):725, 1980. 43

PD Drummond and DF Walls. Quantum theory of optical bistability. ii. atomic fluorescence in a high-q cavity. *Physical Review A*, 23(5):2563, 1981. 43

Zachary Dutton, KVRM Murali, William D Oliver, and TP Orlando. Electromagnetically induced transparency in superconducting quantum circuits: effects of decoherence, tunneling, and multilevel crosstalk. *Physical Review B*, 73(10):104516, 2006. 111

Matt Eichenfield, Jasper Chan, Ryan M Camacho, Kerry J Vahala, and Oskar Painter. Optomechanical crystals. *Nature*, 462(7269):78–82, 2009. 90

Albert Einstein. The photoelectric effect. *Ann. Phys*, 17:132, 1905. 4

MD Eisaman, J Fan, A Migdall, and SV Polyakov. Invited review article: Single-photon sources and detectors. *Review of scientific instruments*, 82(7):071101, 2011. 5

Florian Elste, SM Girvin, and AA Clerk. Quantum noise interference and backaction cooling in cavity nanomechanics. *Physical review letters*, 102(20):207209, 2009. 91

Bixuan Fan, Zhenglu Duan, Lu Zhou, Chunhua Yuan, ZY Ou, and Weiping Zhang. Generation of a single-photon source via a four-wave mixing process in a cavity. *Physical Review A*, 80(6):063809, 2009. 5

Bixuan Fan, Anton F Kockum, Joshua Combes, Göran Johansson, Io-chun Hoi, CM Wilson, Per Delsing, GJ Milburn, and Thomas M Stace. Breakdown of the cross-kerr scheme for photon counting. *Physical review letters*, 110(5):053601, 2013. ..... 41, 68, 72, 73, 87

Arkady Fedorov, Lars Steffen, Matthias Baur, MP Da Silva, and Andreas Wallraff. Implementation of a toffoli gate with superconducting circuits. *Nature*, 481(7380):170–172, 2011. 15

Feynman. *Lectures on Physics*. Addison Wesley Publishing Company Incorporated, 1965. 8

JM Fink, M Göppl, M Baur, R Bianchetti, PJ Leek, Alexandre Blais, and Andreas Wallraff. Climbing the jaynes–cummings ladder and observing its nonlinearity in a cavity qed system. *Nature*, 454(7202):315–318, 2008. 19

Stuart J Freedman and John F Clauser. Experimental test of local hidden-variable theories. *Physical Review Letters*, 28(14):938, 1972. 4

Jonathan R Friedman, Vijay Patel, Wei Chen, SK Tolpygo, and James E Lukens. Quantum superposition of distinct macroscopic states. *nature*, 406(6791):43–46, 2000. 14

Jay Gambetta, W. A. Braff, A. Wallraff, S. M. Girvin, and R. J. Schoelkopf. Protocols for optimal readout of qubits using a continuous quantum nondemolition measurement. *Phys. Rev. A*, 76:012325, Jul 2007. doi: 10.1103/PhysRevA.76.012325. . . 27, 71, 72, 79

C. W. Gardiner. Driving a quantum system with the output field from another driven quantum system. *Phys. Rev. Lett.*, 70:2269–2272, Apr 1993a. 70

Crispin Gardiner and Peter Zoller. *Quantum noise: a handbook of Markovian and non-Markovian quantum stochastic methods with applications to quantum optics*, volume 56. Springer, 2004. . . . . 21, 35, 36, 53, 70

CW Gardiner. Driving a quantum system with the output field from another driven quantum system. *Physical review letters*, 70(15):2269–2272, 1993b. 36

Emanuel Gavartin, Pierre Verlot, and Tobias J Kippenberg. A hybrid on-chip optomechanical transducer for ultrasensitive force measurements. *Nature nanotechnology*, 7(8):509–514, 2012. 105

Julio Gea-Banacloche. Impossibility of large phase shifts via the giant kerr effect with single-photon wave packets. *Physical Review A*, 81(4):043823, 2010. 50

Roohollah Ghobadi, AR Bahrampour, and C Simon. Quantum optomechanics in the bistable regime. *Physical Review A*, 84(3):033846, 2011. 93

Schwab Gigan, HR Böhm, M Paternostro, F Blaser, G Langer, JB Hertzberg, KC Schwab, D Bäuerle, M Aspelmeyer, and A Zeilinger. Self-cooling of a micromirror by radiation pressure. *Nature*, 444(7115):67–70, 2006. 90

Roy J. Glauber. The quantum theory of optical coherence. *Phys. Rev.*, 130:2529–2539, Jun 1963a. doi: 10.1103/PhysRev.130.2529. . . . . 5, 67

Roy J Glauber. Coherent and incoherent states of the radiation field. *Physical Review*, 131 (6):2766, 1963b. 73

Sebastien Gleyzes, Stefan Kuhr, Christine Guerlin, Julien Bernu, Samuel Deleglise, Ulrich Busk Hoff, Michel Brune, Jean-Michel Raimond, and Serge Haroche. Quantum jumps of light recording the birth and death of a photon in a cavity. *Nature*, 446(7133): 297–300, 2007. 68

M Göppl, A Fragner, M Baur, R Bianchetti, S Filipp, JM Fink, PJ Leek, G Puebla, L Steffen, and Andreas Wallraff. Coplanar waveguide resonators for circuit quantum electrodynamics. *Journal of Applied Physics*, 104(11):113904, 2008. 14

John E Gough, Matthew R James, Hendra I Nurdin, and Joshua Combes. Quantum filtering for systems driven by fields in single-photon states or superposition of coherent states. *Physical Review A*, 86(4):43819, 2012. 39

Luke C. G. Govia, Emily J. Pritchett, Seth T. Merkel, Deanna Pineau, and Frank K. Wilhelm. Theory of josephson photomultipliers: Optimal working conditions and back action. *Phys. Rev. A*, 86:032311, Sep 2012. doi: $10.1103/\mathrm{PhysRevA}.86.032311$. 68

Philippe Grangier, Juan Ariel Levenson, and Jean-Philippe Poizat. Quantum non-demolition measurements in optics. *Nature*, 396(6711):537–542, 1998. 51

Christine Guerlin, Julien Bernu, Samuel Deleglise, Clement Sayrin, Sebastien Gleyzes, Stefan Kuhr, Michel Brune, Jean-Michel Raimond, and Serge Haroche. Progressive field-state collapse and quantum non-demolition photon counting. *Nature*, 448(7156):889–893, 2007. 6

Stephen E Harris. Electromagnetically induced transparency. *Physics Today*, 50(7):36–42, 2008. 88

Ferdinand Helmer, Matteo Mariantoni, Enrique Solano, and Florian Marquardt. Quantum nondemolition photon detection in circuit qed and the quantum zeno effect. *Phys. Rev. A*, 79:052115, May 2009. doi: $10.1103/\mathrm{PhysRevA}.79.052115$. 5, 67

Carl W Helstrom. Detection theory and quantum mechanics. *Information and Control*, 10 (3):254–291, 1967. 79

Carl W Helstrom. Detection theory and quantum mechanics (ii). *Information and Control*, 13(2):156–171, 1968. 79

Carl W Helstrom. Quantum detection and estimation theory. *Journal of Statistical Physics*, 1(2):231–252, 1969. 79

Markus Hijlkema, Bernhard Weber, Holger P Specht, Simon C Webster, Axel Kuhn, and Gerhard Rempe. A single-photon server with just one atom. *Nature Physics*, 3(4):253–255, 2007. 5

FT Hioe. Dynamic symmetries in quantum electronics. *Physical Review A*, 28:879–886, 1983. 136

Io-Chun Hoi, Anton F Kockum, Tauno Palomaki, Thomas M Stace, Bixuan Fan, Lars Tornberg, Sankar R Sathyamoorthy, Göran Johansson, Per Delsing, and CM Wilson. Giant cross–kerr effect for propagating microwaves induced by an artificial atom. *Physical review letters*, 111(5):053601, 2013. ..... 15, 35, 44, 45, 47, 50, 51, 68, 87, 111

AA Houck, DI Schuster, JM Gambetta, JA Schreier, BR Johnson, JM Chow, L Frunzio, J Majer, MH Devoret, SM Girvin, et al. Generating single microwave photons in a circuit. *Nature*, 449(7160):328–331, 2007. 6

Yong Hu, Guo-Qin Ge, Shi Chen, Xiao-Fei Yang, and You-Ling Chen. Cross-kerr-effect induced by coupled josephson qubits in circuit quantum electrodynamics. *Phys. Rev. A*, 84:012329, Jul 2011. doi: $10.1103/\mathrm{PhysRevA}.84.012329$. 51

Kôdi Husimi. Some formal properties of the density matrix. In *Proc. Phys. Math. Soc. Jpn*, volume 22, page 123, 1940. 73

N Imoto, HA Haus, and Y Yamamoto. Quantum nondemolition measurement of the photon number via the optical kerr effect. *Physical Review A*, 32(4):2287, 1985. 44

WAYNEM ITANO, JC Bergquist, and DJ Wineland. Laser spectroscopy of trappped atomic ions. *Science*, 237(4815):612, 1987. 23

Alan Jeffrey and Daniel Zwillinger. *Table of integrals, series, and products*. Academic Press, 2007. 102

Cheng Jiang, Hongxiang Liu, Yuanshun Cui, Xiaowei Li, Guibin Chen, and Xuemin Shuai. Controllable optical bistability based on photons and phonons in a two-mode optomechanical system. *Physical Review A*, 88(5):055801, 2013. 93

Guang-Sheng Jin, Yuan Lin, and Biao Wu. Generating multiphoton greenberger-horne-zeilinger states with weak cross-kerr nonlinearity. *Physical Review A*, 75(5):54302, 2007. 44

BR Johnson, MD Reed, AA Houck, DI Schuster, Lev S Bishop, E Ginossar, JM Gambetta, L DiCarlo, L Frunzio, SM Girvin, et al. Quantum non-demolition detection of single microwave photons in a circuit. *Nature Physics*, 6(9):663–667, 2010. . . . . 6, 68

Brian David Josephson. Possible new effects in superconductive tunnelling. *Physics Letters*, 1(7):251–253, 1962. 10

Hoonsoo Kang and Yifu Zhu. Observation of large kerr nonlinearity at low light intensities. *Phys. Rev. Lett.*, 91:093601, Aug 2003. doi: $10.1103/\mathrm{PhysRevLett.91.093601}$. 51

Matthias Keller, Birgit Lange, Kazuhiro Hayasaka, Wolfgang Lange, and Herbert Walther. Continuous generation of single photons with controlled waveform in an ion-trap cavity system. *Nature*, 431(7012):1075–1078, 2004. 5

Eyal Kenig, MC Cross, Ron Lifshitz, RB Karabalin, LG Villanueva, MH Matheny, and ML Roukes. Passive phase noise cancellation scheme. *Physical review letters*, 108 (26):264102, 2012. 109

JB Khurgin, MW Pruessner, TH Stievater, and WS Rabinovich. Laser-rate-equation description of optomechanical oscillators. *Physical review letters*, 108(22):223904, 2012. 97

Emanuel Knill, Raymond Laflamme, and Gerald J Milburn. A scheme for efficient quantum computation with linear optics. *nature*, 409(6816):46–52, 2001. ..... 4, 5

Jens Koch, M Yu Terri, Jay Gambetta, Andrew A Houck, DI Schuster, J Majer, Alexandre Blais, Michel H Devoret, Steven M Girvin, and Robert J Schoelkopf. Charge-insensitive qubit design derived from the cooper pair box. *Physical Review A*, 76(4):042319, 2007a. 14, 16, 17

Jens Koch, Terri M. Yu, Jay Gambetta, A. A. Houck, D. I. Schuster, J. Majer, Alexandre Blais, M. H. Devoret, S. M. Girvin, and R. J. Schoelkopf. Charge-insensitive qubit design derived from the cooper pair box. *Phys. Rev. A*, 76:042319, Oct 2007b. doi: $10.1103/\mathrm{PhysRevA.76.042319}$. 68

S Komiyama, O Astafiev, V Antonov, T Kutsuwa, and H Hirai. A single-photon detector in the far-infrared range. *Nature*, 403(6768):405–407, 2000. 5

Yuimaru Kubo, Cecile Grezes, Andreas Dewes, T Umeda, Junichi Isoya, H Sumiya, N Morishita, H Abe, S Onoda, T Ohshima, et al. Hybrid quantum circuit with a superconducting qubit coupled to a spin ensemble. *Physical review letters*, 107(22):220501, 2011. 8

Paul G Kwiat and Raymond Y Chiao. Observation of a nonclassical berryąŕs phase for the photon. *Physical review letters*, 66(5):588, 1991. 5

A Lacaita, F Zappa, S Cova, and P Lovati. Single-photon detection beyond 1 μm: performance of commercially available ingaas/Inp detectors. *Applied Optics*, 35(16):2986–2996, 1996. 5

Melvin Lax. Formal theory of quantum fluctuations from a driven state. *Physical Review*, 129(5):2342, 1963. ..... 54, 139

Peter Lebedew. Untersuchungen über die druckkräfte des lichtes. *Annalen der Physik*, 311 (11):433–458, 1901. 90

Hai-Woong Lee. Theory and application of the quantum phase-space distribution functions. *Physics Reports*, 259(3):147–211, 1995. 73

Gilbert N Lewis. The conservation of photons. *Nature*, 118:874–875, 1926. 4

Tongcang Li, Simon Kheifets, and Mark G Raizen. Millikelvin cooling of an optically trapped microsphere in vacuum. *Nature Physics*, 7(7):527–530, 2011. 90

Qing Lin and Jian Li. Quantum control gates with weak cross-kerr nonlinearity. *Physical Review A*, 79(2):022301, 2009. 44

Ying Lu, Lijuan Xu, Meiling Shu, Peng Wang, and Jianquan Yao. Proposal to produce coupled resonator-induced transparency and bistability using microresonator enhanced mach–zehnder interferometer. *Photonics Technology Letters, IEEE*, 20(7):529–531, 2008. 90

Max Ludwig, Björn Kubala, and Florian Marquardt. The optomechanical instability in the quantum regime. *New Journal of Physics*, 10(9):095013, 2008. ..... 93, 98

Björn Maes, Peter Bienstman, and Roel Baets. Switching in coupled nonlinear photonic-crystal resonators. *JOSA B*, 22(8):1778–1784, 2005. 90

Theodore H Maiman. Stimulated optical radiation in ruby. 187:493–494, 1960. 42

F. Mallet, M. A. Castellanos-Beltran, H. S. Ku, S. Glancy, E. Knill, K. D. Irwin, G. C. Hilton, L. R. Vale, and K. W. Lehnert. Quantum state tomography of an itinerant squeezed microwave field. *Phys. Rev. Lett.*, 106:220502, Jun 2011. doi: $10.1103/\mathrm{PhysRevLett.106.220502}$. 77, 78

François Mallet, Florian R Ong, Agustin Palacios-Laloy, Francois Nguyen, Patrice Bertet, Denis Vion, and Daniel Esteve. Single-shot qubit readout in circuit quantum electrodynamics. *Nature Physics*, 5(11):791–795, 2009. 113

M Mancinelli, R Guider, P Bettotti, M Masi, M Rao Vanacharla, and L Pavesi. Coupled-resonator-induced-transparency concept for wavelength routing applications. *Optics express*, 19(13):12227–12240, 2011. 90

Stefano Mancini and Paolo Tombesi. High-sensitivity force measurement using entangled probes. *EPL (Europhysics Letters)*, 61(1):8, 2003. 106

LECG Mandel, EC Gr Sudarshan, and E Wolf. Theory of photoelectric detection of light fluctuations. *Proceedings of the Physical Society*, 84(3):435, 1964. . . . . 5, 67

Vladimir E Manucharyan, Jens Koch, Leonid I Glazman, and Michel H Devoret. Fluxonium: Single cooper-pair circuit free of charge offsets. *Science*, 326(5949):113–116, 2009. 14

Francesco Marino and Francesco Marin. Coexisting attractors and chaotic canard explosions in a slow-fast optomechanical system. *Physical Review E*, 87(5):052906, 2013. . . 93

Florian Marquardt, JGE Harris, and SM Girvin. Dynamical multistability induced by radiation pressure in high-finesse micromechanical optical cavities. *Physical review letters*, 96(10): 103901, 2006. . . . . 93, 97

John M Martinis, S Nam, J Aumentado, and C Urbina. Rabi oscillations in a large josephson-junction qubit. *Physical Review Letters*, 89(11):117901, 2002. 14

Nobuyuki Matsuda, Ryosuke Shimizu, Yasuyoshi Mitsumori, Hideo Kosaka, and Keiichi Edamatsu. Observation of optical-fibre kerr nonlinearity at the single-photon level. *Nature photonics*, 3(2):95–98, 2009. 44

J McKeever, A Boca, AD Boozer, R Miller, JR Buck, A Kuzmich, and HJ Kimble. Deterministic generation of single photons from one atom trapped in a cavity. *Science*, 303(5666): 1992–1994, 2004. 5

Constanze Metzger, Max Ludwig, Clemens Neuenhahn, Alexander Ortlieb, Ivan Favero, Khaled Karrai, and Florian Marquardt. Self-induced oscillations in an optomechanical system driven by bolometric backaction. *Physical review letters*, 101(13):133903, 2008. 93, 97

GJ Milburn. Quantum optical fredkin gate. *Physical Review Letters*, 62(18):2124, 1989. 44

GJ Milburn. Classical and quantum conditional statistical dynamics. *Quantum and Semiclassical Optics: Journal of the European Optical Society Part B*, 8(1):269, 1996. 22

Takashi Mimura. The early history of the high electron mobility transistor (hemt). *IEEE Transactions on microwave theory and techniques*, 50(3):780–782, 2002. 6

Mervlyn Moodley and Francesco Petruccione. Stochastic wave-function unraveling of the generalized lindblad master equation. *Phys. Rev. A*, 79:042103, Apr 2009. doi: $10.1103/\mathrm{PhysRevA.79.042103}$. 75

J Moser, J Güttinger, A Eichler, MJ Esplandiu, DE Liu, MI Dykman, and A Bachtold. Ultrasensitive force detection with a nanotube mechanical resonator. *Nature nanotechnology*, 8(7):493–496, 2013. 105

W. J. Munro, Kae Nemoto, R. G. Beausoleil, and T. P. Spiller. High-efficiency quantum-nondemolition single-photon-number-resolving detector. *Phys. Rev. A*, 71:033819, Mar 2005a. doi: $10.1103/\mathrm{PhysRevA.71.033819}$. 5, 35, 43, 44, 67

William J Munro, Kae Nemoto, and Timothy P Spiller. Weak nonlinearities: a new route to optical quantum computation. *New Journal of Physics*, 7(1):137, 2005b. 44, 66

Yu Nakamura, Yu A Pashkin, and JS Tsai. Coherent control of macroscopic quantum states in a single-cooper-pair box. *Nature*, 398(6730):786–788, 1999. 14

Ahmer Naweed, G Farca, SI Shopova, and AT Rosenberger. Induced transparency and absorption in coupled whispering-gallery microresonators. *Physical Review A*, 71(4): 043804, 2005. 88

Kae Nemoto and William J Munro. Nearly deterministic linear optical controlled-not gate. *Physical review letters*, 93(25):250502, 2004. 66

Michael A Nielsen and Isaac L Chuang. *Quantum computation and quantum information*. Cambridge university press, 2010. . . . . 20, 21

Thomas Niemczyk, F Deppe, H Huebl, EP Menzel, F Hocke, MJ Schwarz, JJ Garcia-Ripoll, D Zueco, T Hümmer, E Solano, et al. Circuit quantum electrodynamics in the ultrastrong-coupling regime. *Nature Physics*, 6(10):772–776, 2010. 8

EF Nxcnons and GF Huu. A preliminary communication on the pressure of heat and light radiation. 1901. 90

B. Peaudecerf, T. Rybarczyk, S. Gerlich, S. Gleyzes, J. M. Raimond, S. Haroche, I. Dotsenko, and M. Brune. Adaptive quantum nondemolition measurement of a photon number. *Phys. Rev. Lett.*, 112:080401, Feb 2014. doi: 10.1103/PhysRevLett.112.080401. 6, 68

David T Pegg, Lee S Phillips, and Stephen M Barnett. Optical state truncation by projection synthesis. *Physical review letters*, 81:1604–1606, 1998. 5

B. Peropadre, G. Romero, G. Johansson, C. M. Wilson, E. Solano, and J. J. García-Ripoll. Approaching perfect microwave photodetection in circuit qed. *Phys. Rev. A*, 84:063834, Dec 2011. doi: 10.1103/PhysRevA.84.063834. ..... 6, 68

C. Perrella, P. S. Light, J. D. Anstie, F. Benabid, T. M. Stace, A. G. White, and A. N. Luiten. High-efficiency cross-phase modulation in a gas-filled waveguide. *Phys. Rev. A*, 88:013819, Jul 2013. doi: 10.1103/PhysRevA.88.013819. 45

Mathieu Pierre, Ida-Maria Svensson, Sankar Raman Sathyamoorthy, Göran Johansson, and Per Delsing. Storage and on-demand release of microwaves using superconducting resonators with tunable coupling. *Applied Physics Letters*, 104(23):232604, 2014. . 113

Max Planck. On the theory of the energy distribution law of the normal spectrum. *Verh. Dtsch. Phys. Ges.*, 2:237, 1900. 4

JH Plantenberg, PC De Groot, CJPM Harmans, and JE Mooij. Demonstration of controlled-not quantum gates on a pair of superconducting quantum bits. *Nature*, 447(7146):836–839, 2007. 8

A Pontin, M Bonaldi, A Borrielli, FS Cataliotti, F Marino, GA Prodi, E Serra, and F Marin. Detection of weak stochastic forces in a parametrically stabilized micro-optomechanical system. *Physical Review A*, 89(2):023848, 2014. 105

A. Poudel, R. McDermott, and M. G. Vavilov. Quantum efficiency of a microwave photon detector based on a current-biased josephson junction. *Phys. Rev. B*, 86:174506, Nov 2012. doi: $10.1103/\mathrm{PhysRevB.86.174506}$. 68

Jiang Qian, AA Clerk, K Hammerer, and Florian Marquardt. Quantum signatures of the optomechanical instability. *Physical review letters*, 109(25):253601, 2012. ..... 93, 98

Andreas Reiserer, Stephan Ritter, and Gerhard Rempe. Nondestructive detection of an optical photon. *Science*, 342(6164):1349–1351, 2013. ..... 5, 67

Chad Rigetti, Jay M Gambetta, Stefano Poletto, BLT Plourde, Jerry M Chow, AD Córcoles, John A Smolin, Seth T Merkel, JR Rozen, George A Keefe, et al. Superconducting qubit in a waveguide cavity with a coherence time approaching 0.1 ms. *Physical Review B*, 86 (10):100506, 2012. ..... 8, 15

G. Romero, J. J. García-Ripoll, and E. Solano. Microwave photon detector in circuit qed. *Phys. Rev. Lett.*, 102:173602, Apr 2009a. doi: $10.1103/\mathrm{PhysRevLett.102.173602}$. . 6, 68

Guillermo Romero, Juan José García-Ripoll, and Enrique Solano. Photodetection of propagating quantum microwaves in circuit qed. *Physica Scripta*, 2009(T137):014004, 2009b. 6, 68

Kristine M Rosfjord, Joel KW Yang, Eric A Dauler, Andrew J Kerman, Vikas Anant, Boris M Voronov, Gregory N Gol'Tsman, and Karl K Berggren. Nanowire single-photon detector with an integrated optical cavity and anti-reflection coating. *Optics Express*, 14(2):527–534, 2006. 5

Sankar R. Sathyamoorthy, L. Tornberg, Anton F. Kockum, Ben Q. Baragiola, Joshua Combes, C. M. Wilson, Thomas M. Stace, and G. Johansson. Quantum nondemolition detection of a propagating microwave photon. *Phys. Rev. Lett.*, 112:093601, Mar 2014. doi: $10.1103/\mathrm{PhysRevLett.112.093601}$. 6, 68, 69, 75, 81, 87

A Schliesser, P DelaŕHaye, N Nooshi, KJ Vahala, and TJ Kippenberg. Radiation pressure cooling of a micromechanical oscillator using dynamical backaction. *Physical Review Letters*, 97(24):243905, 2006. 90

H Schmidt and A Imamoglu. Giant kerr nonlinearities obtained by electromagnetically induced transparency. *Optics letters*, 21(23):1936–1938, 1996. ..... 44, 64

RJ Schoelkopf and SM Girvin. Wiring up quantum systems. *Nature*, 451(7179):664–669, 2008. 8

Peter Shadbolt, Jonathan CF Mathews, Anthony Laing, and Jeremy L O'Brien. Testing foundations of quantum mechanics with photons. *Nature Physics*, 10(4):278–286, 2014. 4

Jeffrey H Shapiro. Single-photon kerr nonlinearities do not help quantum computation. *Physical Review A*, 73(6):062305, 2006. ..... 50, 82

Jeffrey H Shapiro and Mohsen Razavi. Continuous-time cross-phase modulation and quantum computation. *New Journal of Physics*, 9(1):16, 2007. 50

Jung-Tsung Shen and Shanhui Fan. Coherent single photon transport in a one-dimensional waveguide coupled with superconducting quantum bits. *Physical review letters*, 95(21): 213001, 2005. ..... 35, 60, 61

Jung-Tsung Shen and Shanhui Fan. Theory of single-photon transport in a single-mode waveguide. i. coupling to a cavity containing a two-level atom. *Phys. Rev. A*, 79:023837, Feb 2009. doi: $10.1103/\mathrm{PhysRevA.79.023837}$. 61

Ch Silberhorn, Ping Koy Lam, Oliver Weiss, F König, N Korolkova, and G Leuchs. Generation of continuous variable einstein-podolsky-rosen entanglement via the kerr nonlinearity in an optical fiber. *Physical Review Letters*, 86(19):4267, 2001. 44

Thomas B Simpson, Jia-Ming Liu, Mohammad AlMulla, Nicholas G Usechak, and Vassilios Kovanis. Limit-cycle dynamics with reduced sensitivity to perturbations. *Physical review letters*, 112(2):023901, 2014. 109

Gary F Sinclair and Natalia Korolkova. Effective cross-kerr hamiltonian for a nonresonant four-level atom. *Physical Review A*, 77(3):033843, 2008. ..... 44, 64

D. H. Slichter, R. Vijay, S. J. Weber, S. Boutin, M. Boissonneault, J. M. Gambetta, A. Blais, and I. Siddiqi. Measurement-induced qubit state mixing in circuit qed from up-converted dephasing noise. *Phys. Rev. Lett.*, 109:153601, Oct 2012. doi: $10.1103/\mathrm{PhysRevLett.}$ 109.153601. 82

Brian J Smith, P Mahou, Offir Cohen, JS Lundeen, and IA Walmsley. Photon pair generation in birefringent optical fibers. *Optics express*, 17(26):23589–23602, 2009. 5

David D Smith, Hongrok Chang, Kirk A Fuller, AT Rosenberger, and Robert W Boyd. Coupled-resonator-induced transparency. *Physical Review A*, 69(6):063804, 2004. . 88, 98

Steven H Strogatz. *Nonlinear dynamics and chaos: with applications to physics, biology and chemistry*. Perseus publishing, 2001. 94

ECG Sudarshan. Equivalence of semiclassical and quantum mechanical descriptions of statistical light beams. *Physical Review Letters*, 10(7):277–279, 1963. 73

Geoffrey Ingram Taylor. Interference fringes with feeble light. In *Proceedings of the Cambridge Philosophical Society*, volume 15, pages 114–115, 1909. 4

JD Teufel, T Donner, MA Castellanos-Beltran, JW Harlow, and KW Lehnert. Nanomechanical motion measured with an imprecision below that at the standard quantum limit. *Nature nanotechnology*, 4(12):820–823, 2009. ..... 77, 78

JD Thompson, BM Zwickl, AM Jayich, Florian Marquardt, SM Girvin, and JGE Harris. Strong dispersive coupling of a high-finesse cavity to a micromechanical membrane. *Nature*, 452(7183):72–75, 2008. 90

Michael Tinkham. *Introduction to superconductivity*. Courier Dover Publications, 2012. 10

Kouki Totsuka, Norihiko Kobayashi, and Makoto Tomita. Slow light in coupled-resonator-induced transparency. *Physical review letters*, 98(21):213904, 2007. 90

Mankei Tsang. Continuous quantum hypothesis testing. *Physical review letters*, 108(17): 170502, 2012. ..... 71, 79

Caspar H Van der Wal, ACJ Ter Haar, FK Wilhelm, RN Schouten, CJPM Harmans, TP Orlando, Seth Lloyd, and JE Mooij. Quantum superposition of macroscopic persistent-current states. *Science*, 290(5492):773–777, 2000. 14

Harry L Van Trees. *Detection, estimation, and modulation theory*. John Wiley & Sons, 2004. 79

Vivek Venkataraman, Kasturi Saha, and Alexander L Gaeta. Phase modulation at the few-photon level for weak-nonlinearity-based quantum computing. *Nature Photonics*, 7(2): 138–141, 2013. 45

J Verdú, H Zoubi, Ch Koller, J Majer, H Ritsch, and J Schmiedmayer. Strong magnetic coupling of an ultracold gas to a superconducting waveguide cavity. *Physical review letters*, 103(4):043603, 2009. 8

David Vitali, Mauro Fortunato, and Paolo Tombesi. Complete quantum teleportation with a kerr nonlinearity. *Phys. Rev. Lett.*, 85:445–448, Jul 2000. doi: $10.1103/\mathrm{PhysRevLett.85.445}$. 44

Andreas Wallraff, David I Schuster, Alexandre Blais, L Frunzio, R-S Huang, J Majer, S Kumar, Steven M Girvin, and Robert J Schoelkopf. Strong coupling of a single photon to a superconducting qubit using circuit quantum electrodynamics. *Nature*, 431(7005):162–167, 2004. ..... 8, 19

Xin-Wen Wang, Deng-Yu Zhang, Shi-Qing Tang, Li-Jun Xie, Zhi-Yong Wang, and Le-Man Kuang. Photonic two-qubit parity gate with tiny cross–kerr nonlinearity. *Phys. Rev. A*, 85: 052326, May 2012. doi: $10.1103/\mathrm{PhysRevA.85.052326}$. 44

Zeng-Bin Wang, Karl-Peter Marzlin, and Barry C Sanders. Large cross-phase modulation between slow copropagating weak pulses in rb 87. *Physical review letters*, 97(6):063901, 2006a. 44

Zeng-Bin Wang, Karl-Peter Marzlin, and Barry C Sanders. Large cross-phase modulation between slow copropagating weak pulses in rb 87. *Physical review letters*, 97(6):063901, 2006b. 44

Eugene Wigner. On the quantum correction for thermodynamic equilibrium. *Physical Review*, 40(5):749, 1932. 73

CM Wilson, Göran Johansson, A Pourkabirian, Michael Simoen, JR Johansson, Tim Duty, F Nori, and Per Delsing. Observation of the dynamical casimir effect in a superconducting circuit. *Nature*, 479(7373):376–379, 2011. 8

HM Wiseman. Quantum trajectories and quantum measurement theory. *Quantum and Semiclassical Optics: Journal of the European Optical Society Part B*, 8(1):205, 1996. . 20

HM Wiseman and GJ Milburn. Interpretation of quantum jump and diffusion processes illustrated on the bloch sphere. *Physical Review A*, 47(3):1652, 1993. 25

Howard M Wiseman and Gerard J Milburn. *Quantum measurement and control*. Cambridge University Press, 2010. . . . . 20, 21, 23, 25, 27, 28, 29, 30, 70, 75

Ze-Liang Xiang, Sahel Ashhab, JQ You, and Franco Nori. Hybrid quantum circuits: Superconducting circuits interacting with other quantum systems. *Reviews of Modern Physics*, 85(2):623, 2013. 8

Qianfan Xu, Sunil Sandhu, Michelle L Povinelli, Jagat Shakya, Shanhui Fan, and Michal Lipson. Experimental realization of an on-chip all-optical analogue to electromagnetically induced transparency. *Physical review letters*, 96(12):123901, 2006a. 88

Qianfan Xu, Jagat Shakya, and Michal Lipson. Direct measurement of tunable optical delays on chip analogue to electromagnetically induced transparency. *Optics express*, 14 (14):6463–6468, 2006b. 90

Tsuyoshi Yamamoto, Yu A Pashkin, Oleg Astafiev, Yasunobu Nakamura, and Jaw-Shen Tsai. Demonstration of conditional gate operation using superconducting charge qubits. *Nature*, 425(6961):941–944, 2003. 8

Hidehiro Yonezawa, Daisuke Nakane, Trevor A Wheatley, Kohjiro Iwasawa, Shuntaro Takeda, Hajime Arao, Kentaro Ohki, Koji Tsumura, Dominic W Berry, Timothy C Ralph, et al. Quantum-enhanced optical-phase tracking. *Science*, 337(6101):1514–1517, 2012. 59

JQ You and Franco Nori. Atomic physics and quantum optics using superconducting circuits. *Nature*, 474(7353):589–597, 2011. 8

ZL Yuan, BE Kardynal, AW Sharpe, and AJ Shields. High speed single photon detection in the near infrared. *Applied Physics Letters*, 91(4):041114, 2007. 5

B Yurke. Squeezed-state generation using a josephson parametric amplifier. *JOSA B*, 4 (10):1551–1557, 1987. ..... 6, 10

Stav Zaitsev, Ashok K Pandey, Oleg Shtempluck, and Eyal Buks. Forced and self-excited oscillations of an optomechanical cavity. *Physical Review E*, 84(4):046605, 2011. 93, 97

Stav Zaitsev, Oded Gottlieb, and Eyal Buks. Nonlinear dynamics of a microelectromechanical mirror in an optical resonance cavity. *Nonlinear Dynamics*, 69(4):1589–1610, 2012. 97

Xiaobo Zhu, Shiro Saito, Alexander Kemp, Kosuke Kakuyanagi, Shin-ichi Karimoto, Hayato Nakano, William J Munro, Yasuhiro Tokura, Mark S Everitt, Kae Nemoto, et al. Coherent coupling of a superconducting flux qubit to an electron spin ensemble in diamond. *Nature*, 478(7368):221–224, 2011. 8

Appendix A

Appendices

A.1 The analytical solution for a three-level system on resonance

Here we provide the details of the analytical solution for a three-level system. As presented in the main text, we consider a three-level transmon coupling with a coherent field at the $|b\rangle \leftrightarrow |c\rangle$ transition and a single photon at the $|a\rangle \leftrightarrow |b\rangle$ transition. The one-photon Fock state master equations Baragiola et al. (2012) are given by

$$\dot{\rho}_{0,0}(t) = -i[\hat{H}_s, \rho_{0,0}] + \mathcal{D}[\hat{L}_b]\rho_{0,0} + \mathcal{D}[\hat{L}_c]\rho_{0,0} \quad \text{(A.1)}$$

$$\dot{\rho}_{0,1}(t) = -i[\hat{H}_s, \rho_{0,1}] + \mathcal{D}[\hat{L}_b]\rho_{0,1} + \mathcal{D}[\hat{L}_c]\rho_{0,1} + f^*(t)[\hat{L}_b, \rho_{0,0}] \quad \text{(A.2)}$$

$$\dot{\rho}_{1,1}(t) = -i[\hat{H}_s, \rho_{1,1}] + \mathcal{D}[\hat{L}_b]\rho_{1,1} + \mathcal{D}[\hat{L}_c]\rho_{1,1} + f^*(t)[\hat{L}_b, \rho_{1,0}] + f(t)[\rho_{0,1}, \hat{L}_b^\dagger] \quad \text{(A.3)}$$

where the temporal profile function $f(t)$, system operators $\hat{L}_b$, $\hat{L}_c$ and system Hamiltonian H_s have been defined in the main text. Here $\rho_{m,n}$ is a matrix and the subscripts m and n denote the photon number basis.

Initially the transmon is prepared at the ground state. The lowest equation for $\rho_{0,0}(t)$ can be easily solved as $\rho_{0,0}(t) = \rho_{0,0}(0)$. Then it is substituted to the next equation for $\rho_{0,1}(t)$, which is traceless. For our system and an arbitrary input Fock state, the generalized density matrices $\rho_{m,n}$ in the Bloch-like representation can be parameterized as

$$\rho_{m,n} = \frac{1}{3}\mathrm{I}\delta(m,n) + \frac{1}{2}\bar{a}_{m,n}\bar{\lambda} \quad \text{(A.4)}$$

where I is a 3 by 3 identity matrix, vector $\bar{a}_{m,n}$ is defined as $\bar{a}_{m,n} = (a_{1mn}, a_{2mn}, a_{3mn}, a_{4mn}, a_{5mn}, a_{6mn},$

$a_{7mn}, a_{8mn})$ and $\bar{\lambda} = (\lambda_1, \lambda_2, \lambda_3, \lambda_4, \lambda_5, \lambda_6, \lambda_7, \lambda_8)$. $\bar{\lambda}$ is a tensor consisting of eight Gell-Mann matrices Hioe (1983):

$$\lambda_1 = \begin{pmatrix} 0 & 1 & 0 \\ 1 & 0 & 0 \\ 0 & 0 & 0 \end{pmatrix} \lambda_2 = \begin{pmatrix} 0 & -i & 0 \\ i & 0 & 0 \\ 0 & 0 & 0 \end{pmatrix} \lambda_3 = \begin{pmatrix} 1 & 0 & 0 \\ 0 & -1 & 0 \\ 0 & 0 & 0 \end{pmatrix} \lambda_4 = \begin{pmatrix} 0 & 0 & 1 \\ 0 & 0 & 0 \\ 1 & 0 & 0 \end{pmatrix}$$

$$\lambda_5 = \begin{pmatrix} 0 & 0 & -i \\ 0 & 0 & 0 \\ i & 0 & 0 \end{pmatrix} \lambda_6 = \begin{pmatrix} 0 & 0 & 0 \\ 0 & 0 & 1 \\ 0 & 1 & 0 \end{pmatrix} \lambda_7 = \begin{pmatrix} 0 & 0 & 0 \\ 0 & 0 & -i \\ 0 & i & 0 \end{pmatrix} \lambda_8 = \frac{1}{\sqrt{3}} \begin{pmatrix} 1 & 0 & 0 \\ 0 & 1 & 0 \\ 0 & 0 & -2 \end{pmatrix} \quad \text{(A.5)}$$

These matrices are traceless, Hermitian, and obey the relation $\mathrm{tr}(\lambda_i \lambda_j) = 2\delta_{ij}$.

Substituting $\rho_{0,1}$ in terms of $\bar{a}_{0,1}$ into the Fock master equation, we can have the coefficient equations for $a_{i01}(t)(i = 1, 2, ...8)$. With initial conditions $a_{i01}(0)(i = 1, 2...8) = 0$, we have the solutions:

$$a_{101}(t) = a_{201}(t) = a_{301}(t) = a_{801}(t) = 0 \quad \text{(A.6)}$$

$$a_{501}(t) = C_1 C_5 \exp(-\theta_1 t) + C_1 C_6 \exp(-\theta_1 t) + C_1 C_7 \exp(-\gamma_{con} t/2) \quad \text{(A.7)}$$

$$a_{601}(t) = C_1 C_2 \exp(-\theta_1 t) + C_1 C_3 \exp(-\theta_2 t) + C_1 C_4 \exp(-\gamma_{con} t/2)] \quad \text{(A.8)}$$

$$a_{401}(t) = i a_{501}(t) \quad \text{(A.9)}$$

$$a_{701}(t) = -i a_{601}(t) \quad \text{(A.10)}$$

where

$$\theta_1 = 3\gamma_b/4 + \sqrt{\gamma_b}\theta/4, \theta_2 = 3\gamma_b/4 - \sqrt{\gamma_b}\theta/4 \quad \text{(A.11)}$$

$$\theta = \sqrt{-32\beta^2 + \gamma_b} \quad \text{(A.12)}$$

$$C_1 = \frac{\sqrt{\gamma_b\gamma_{con}}}{\theta[2\gamma_b(4\beta^2 + \gamma_b) - 3\gamma_b\gamma_{con} + \gamma_{con}^2]} \quad \text{(A.13)}$$

$$C_2 = 4\sqrt{\gamma_b}(8\beta^2 - \gamma_b + \sqrt{\gamma_b}\theta) + \gamma_{con}(\sqrt{\gamma_b} - \theta) \quad \text{(A.14)}$$

$$C_3 = 4\sqrt{\gamma_b}(-8\beta^2 + \gamma_b + \sqrt{\gamma_b}\theta - \gamma_{con}(\sqrt{\gamma_b} + \theta) \quad \text{(A.15)}$$

$$C_4 = -4\gamma_b\theta + 2\gamma_{con}\theta \quad \text{(A.16)}$$

$$C_5 = 2\sqrt{2}\beta(-3\gamma_b + 2\gamma_{con} + \sqrt{\gamma_b}\theta) \quad \text{(A.17)}$$

$$C_6 = 2\sqrt{2}\beta(3\gamma_b - 2\gamma_{con} + \sqrt{\gamma_b}\theta) \quad \text{(A.18)}$$

$$C_7 = 4\sqrt{2\gamma_b}\beta\theta \quad \text{(A.19)}$$

and the density matrix $\rho_{0,1}$ at time t can be represented as

$$\rho_{0,1}(t) = \frac{1}{2}\bar{a}_{0,1}\bar{\lambda} = \begin{pmatrix} 0 & 0 & 0 \\ 0 & 0 & 0 \\ a_{401}(t) & a_{601}(t) & 0 \end{pmatrix} \quad \text{(A.20)}$$

where we used $\gamma_c = 2\gamma_b$ (for a transmon).

The top level equation $\rho_{1,1}(t)$ which represents the actual system evolution is not traceless. In the Bloch representation the equation is $\rho_{1,1} = \frac{1}{3}\mathrm{I} + \frac{1}{2}\bar{a}_{1,1}\bar{\lambda}$ with initial conditions: $a_{811}(t = 0) = -2/\sqrt{3}$ and $a_{i11}(t = 0) = 0$ for $i \neq 8$. Substituting this expression and the solution for $\rho_{0,1}$ into the master equation we have the motion equation for $\bar{a}_{1,1}$.

Only motion equations for a_{211}, a_{311} and a_{811} are coupled and non-zero. We define a vector:

$$x = (a_{211}, a_{311}, a_{811})^T \quad \text{(A.21)}$$

with initial condition

$$x(0) = (0, 0, -\frac{2}{\sqrt{3}})^T \quad \text{(A.22)}$$

$$\frac{dx}{dt} = Ax + B(t) \tag{A.23}$$

with coefficient matrices:

$$A = \begin{pmatrix} -3\gamma_b/2 & -2\sqrt{2\gamma_b}\beta & 0 \\ 2\sqrt{2\gamma_b}\beta & -5\gamma_b/2 & -\sqrt{3}\gamma_b/2 \\ 0 & \sqrt{3}\gamma_b/2 & -\gamma_b/2 \end{pmatrix}, B(t) = \begin{pmatrix} -2\sqrt{\gamma_b}\xi a_{501} \\ -\gamma_b + 2\sqrt{\gamma_b}\xi a_{601} \\ -\frac{\gamma_b}{\sqrt{3}} - 2\sqrt{3\gamma_b}\xi a_{601} \end{pmatrix} \tag{A.24}$$

By diagonalization and integration, we obtain the solutions as:

$$\begin{aligned} & x[i](t) \qquad\qquad (A.25) \\ = \; & V_{i1}exp(A^D_{11}t)[\int exp(-A^D_{11}t')[Q_{11}B_1(t') + Q_{12}B_2(t') + Q_{13}B_3(t')]dt' - \frac{2}{\sqrt{3}}Q_{13}] \\ & +V_{12}exp(A^D_{22}t)[\int exp(-A^D_{22}t')[Q_{21}B_1(t') + Q_{22}B_2(t') + Q_{23}B_3(t')]dt' - \frac{2}{\sqrt{3}}Q_{23}] \\ & +V_{13}exp(A^D_{33}t)[\int exp(-A^D_{33}t')[Q_{31}B_1(t') + Q_{32}B_2(t') + Q_{33}B_3(t')]dt' - \frac{2}{\sqrt{3}}Q_{33}] \\ = \; & V_{i1}S_1 + V_{i2}S_2 + V_{i3}S_3 - \frac{2}{\sqrt{3}}V_{i1}exp(A^D_{11}t)Q_{13} - \frac{2}{\sqrt{3}}V_{i2}exp(A^D_{22}t)Q_{23} - \frac{2}{\sqrt{3}}V_{i3}exp(A^D_{33}t)Q_{33} \end{aligned}$$

where

$$\begin{aligned} S_i &= exp(A^D_{ii}t)\int exp(-A^D_{ii}t')[Q_{i1}B_1(t') + Q_{i2}B_2(t') + Q_{i3}B_3(t')]dt' \qquad (A.26) \\ &= \frac{\gamma_b}{\lambda_i}\left(Q_{i2} + \frac{1}{\sqrt{3}}Q_{i3}\right)(1 - \exp(\lambda_i t)) \\ &\quad + \frac{2\sqrt{\gamma_b\gamma_{con}}C_1C_4}{\gamma_{con} + \lambda_i}\left(Q_{i2} - \sqrt{3}Q_{i3}\right)(\exp(-(\gamma_b + \gamma_{con})t) - \exp(\lambda_i t)) \\ &\quad - \frac{2\sqrt{\gamma_b\gamma_{con}}C_1C_2}{\Delta_1 + \lambda_i + \gamma_{con}/2}\left(Q_{i2} - \sqrt{3}Q_{i3}\right)(\exp(-(\Delta_1 + \gamma_{con}/2)t) - \exp(\lambda_i t)) \\ &\quad - \frac{2\sqrt{\gamma_b\gamma_{con}}C_1C_3}{\Delta_2 + \lambda_i + \gamma_{con}/2}\left(Q_{i2} - \sqrt{3}Q_{i3}\right)(\exp(-(\Delta_2 + \gamma_{con}/2)t) - \exp(\lambda_i t)) \end{aligned}$$

with matrices V, Q and A^D being the eigen-vector matrix, inverse eigen-vector matrix and the diagonalized matrix of the coefficient matrix A.

Then we have the system density matrix at time t:

$$\rho_{1,1}(t) = \frac{1}{3}\mathrm{I} + \frac{1}{2}\begin{pmatrix} a_{311}(t) + \frac{a_{811}(t)}{\sqrt{3}} & -ia_{211}(t) & 0 \\ ia_{211}(t) & \frac{a_{811}(t)}{\sqrt{3}} - a_{311}(t) & 0 \\ 0 & 0 & -2\frac{a_{811}(t)}{\sqrt{3}} \end{pmatrix}, \tag{A.27}$$

The transmon polarisation for the homodyne detection is

$$\langle \hat{y}(t) \rangle = \mathrm{Tr}[-\mathrm{i}(\hat{\mathrm{L}}_\mathrm{c} - \hat{\mathrm{L}}_\mathrm{c}^\dagger)\rho_{1,1}](\mathrm{t}) = \mathrm{Tr}\left[\lambda_2 \rho_{1,1}\right](\mathrm{t}) = \mathrm{a}_{211}(\mathrm{t}) \tag{A.28}$$

The noise or the variance of the detected signal, can be calculated by the quantum regression theorem Lax (1963):

$$\begin{aligned} &(\Delta S)^2 = E\left[S^2 - \bar{S}^2\right] \\ &= \int_0^T dt \int_0^T dt' u(t'-t)\mathrm{Tr}[\hat{\mathrm{y}}(\mathrm{t})\mathrm{e}^{\mathcal{L}(\mathrm{t}'-\mathrm{t})}(-\mathrm{i}\hat{\mathrm{L}}_\mathrm{c}\rho(\mathrm{t}) \\ &+ i\rho(t)\hat{L}_c^\dagger)] + u(t-t')\mathrm{Tr}[\hat{\mathrm{y}}\mathrm{e}^{(\mathrm{t}-\mathrm{t}')}(-\mathrm{i}\hat{\mathrm{L}}_\mathrm{c}\rho(\mathrm{t}') \\ &+ i\rho(t')\hat{L}_c^\dagger)] + T - \bar{S}^2 \end{aligned} \tag{A.29}$$

where $S = \int_0^T dt J_{hom}(t)$, $\bar{S} = \int_0^T dt y_{uc}(t)$ and the function $u(t) = 1(t > 0); u(t) = 0(t < 0)$. The subscripts uc means unconditional results.

A.2 Markovian white noise approximation

This part will give the derivation of the Markovian approximation in a system-reservoir interaction model. For simplicity, the system operator coupled to the reservoir is taken as a bosonic mode and it couples with the reservoir linearly. The Hamiltonian for the system in a rotating wave approximation is

$$\hat{H} = \hbar\omega_c \hat{c}^\dagger \hat{c} + \hbar \int_{-\infty}^{+\infty} \omega \hat{b}_\omega^\dagger \hat{b}_\omega d\omega + \hbar \int_{-\infty}^{+\infty} d\omega g_\omega (\hat{b}_\omega^\dagger \hat{c} + \hat{c}^\dagger \hat{b}_\omega) \tag{A.30}$$

where $\hat{c}$ is a system operator and $\hat{b}_\omega$ is the annihilation operator for the excitation in the reservoir.

The equations of motion are

$$\frac{d\hat{b}_\omega}{dt} = -i\omega\hat{b}_\omega - ig_\omega\hat{c} \tag{A.31}$$

$$\frac{d\hat{c}}{dt} = -i\omega_c\hat{c} - i\int_{-\infty}^{+\infty} d\omega g_\omega b_\omega \tag{A.32}$$

Formally integrating the motion equation for the reservoir, we have

$$\hat{b}_\omega(t) = \hat{b}_\omega(0) - ig_\omega\int_0^t dt'\hat{c}(t')e^{-i\omega(t-t')} \tag{A.33}$$

Substituting Eq. A.33 into Eq. A.32, we have

$$\begin{aligned}\frac{d\hat{c}}{dt} &= -i\omega_c\hat{c} - i\int_{-\infty}^{+\infty} d\omega g_\omega(\hat{b}_\omega(0) - ig_\omega\int_0^t dt'\hat{c}(t')e^{-i\omega(t-t')}) \\ &= -i\omega_c\hat{c} + \hat{F}(t) - \int_0^t dt'\int_{-\infty}^{+\infty} d\omega g_\omega^2\hat{c}(t')e^{-i\omega(t-t')})\end{aligned} \tag{A.34}$$

where $\hat{F}(t) = -i\int_{-\infty}^{+\infty} d\omega g_\omega\hat{b}_\omega(0)$ is defined as a noise operator, which only depends on the system initial condition.

Transforming the system operator to the slowing varying annihilation operator

$$\hat{c} \to \hat{c}e^{i\omega_c t}, \tag{A.35}$$

we have

$$\frac{d\hat{c}}{dt} = \hat{F}(t) - \int_0^t dt'\int_{-\infty}^{+\infty} d\omega g_\omega^2\hat{c}(t')e^{-i(\omega-\omega_c)(t-t')} \tag{A.36}$$

Under the Markovian white noise approximation, the coupling coefficient g_ω varies very little around the frequency ω_c and so that it can be taken as a constant g. The second term on

the right hand can be integrated as

$$\begin{aligned}\int_{-\infty}^{+\infty} g_\omega^2 d\omega e^{-i(\omega-\omega_c)(t-t')} &\approx g^2 \int_{-\infty}^{+\infty} d\omega e^{-i(\omega-\omega_c)(t-t')} \\ &= 2\pi g^2 \delta(t-t')\end{aligned} \tag{A.37}$$

and we arrive at the Langevin equation for $\hat{c}$:

$$\begin{aligned}\frac{d\hat{c}}{dt} &= \hat{F}(t) - 2\pi g^2 \hat{c} \\ &= \hat{F}(t) - \gamma \hat{c}\end{aligned} \tag{A.38}$$

Now we have the relation between the coupling coefficient and the decay rate in an open environment as $g = \sqrt{\gamma/2\pi}$. Eq. A.39 shows that the interaction with the environment causes two effects on the system operator $\hat{c}$: the quantum fluctuations $\hat{F}$ and the dissipation with the rate γ.

A.3 Displaced coherent state picture

When the intra-cavity photon number is large, i.e., $\left\langle \hat{a}^\dagger \hat{a} \right\rangle = (2E/\kappa)^2 \gg 1$, the system Hilbert space will scale as the photon number , which causes computational difficulties. In this case, one can displace the large coherent part away and consider the small quantum fluctuations part of the cavity field. Here we take our photon detection model as an example to derive the master equation in the displaced picture. The original master equation is given by

$$\begin{aligned}\dot{\rho} &= i[\rho, \hat{H}_s] + \kappa \mathcal{D}[\hat{a}]\rho + \gamma_{12}\mathcal{D}[\hat{\sigma}_{12}]\rho + \gamma_{01}\mathcal{D}[\hat{\sigma}_{01}]\rho \\ &+ \sqrt{\gamma_c \gamma_{01}}([\hat{c}\rho, \hat{\sigma}_{10}] + [\hat{\sigma}_{01}, \rho \hat{c}^\dagger])\end{aligned} \tag{A.39}$$

where

$$\hat{H}_s = \Delta_1 \hat{\sigma}_{11} + (\Delta_1 + \Delta_2)\hat{\sigma}_{22} + E(\hat{a} + \hat{a}^\dagger) + g(\hat{a}\hat{\sigma}_{21} + \hat{a}^\dagger \hat{\sigma}_{12}) \tag{A.40}$$

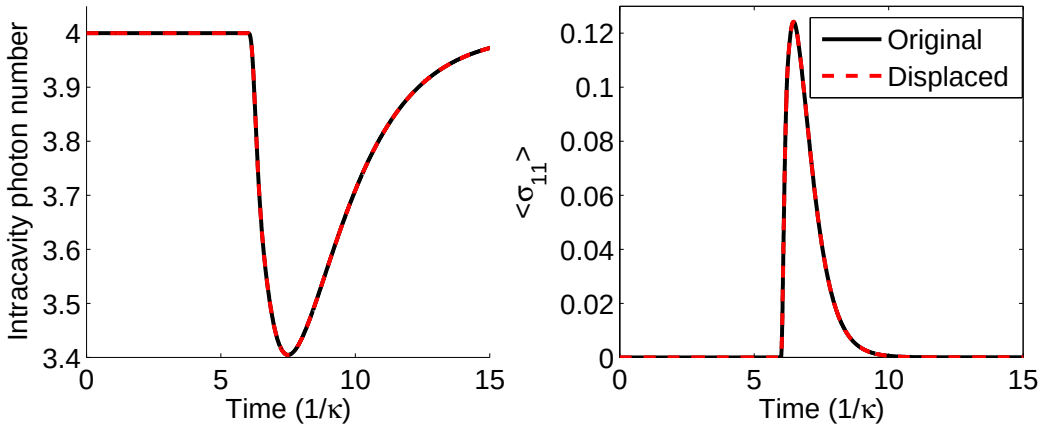

Figure A.1 – The comparison of the time evolution for the intracavity field photon number and the transmon middle state population with the original master equation and the displaced master equation. The parameters are: $g = 4$, $\kappa = 1$, $\gamma = 4$, $E = 1$, and $\gamma_c = 1.8$.

When the mean photon number of $\hat{a}$ field, say, $\langle a \rangle_{ss} = \alpha >> 1$, a displacement transformation can be made:

$$\hat{D}^\dagger(\alpha)\hat{a}\hat{D}(\alpha) = \hat{a} + \alpha \tag{A.41}$$

Under this transformation, the Lindblad decay term becomes

$$\begin{aligned}
\kappa\mathcal{D}[\hat{a}]\rho &= \kappa[(\hat{a}+\alpha)\rho(\hat{a}^\dagger+\alpha^*) - 1/2(\hat{a}^\dagger+\alpha^*)(\hat{a}+\alpha)\rho - 1/2\rho(\hat{a}^\dagger+\alpha^*)(\hat{a}+\alpha)] \\
&= \kappa[\hat{a}\rho\hat{a}^\dagger + \alpha^*\hat{a}\rho + \alpha\rho\hat{a}^\dagger + |\alpha|^2\rho - 1/2(\hat{a}^\dagger\hat{a}\rho - \alpha\hat{a}^\dagger\rho \\
&- \alpha^*\hat{a}\rho - |\alpha|^2\rho - \rho\hat{a}^\dagger\hat{a} - \alpha\rho\hat{a}^\dagger - \alpha^*\rho\hat{a} - |\alpha|^2\rho)] \\
&= \kappa\mathcal{D}[\hat{a}]\rho + 1/2\kappa[\alpha^*\hat{a} - \alpha\hat{a}^\dagger, \rho]
\end{aligned} \tag{A.42}$$

The second term can be rewritten into the effective system Hamiltonian:

$$\begin{aligned}
\hat{H}_s &= \Delta_1\hat{\sigma}_{11} + (\Delta_1+\Delta_2)\hat{\sigma}_{22} + E(\hat{a}+\hat{a}^\dagger) + g(\hat{a}\hat{\sigma}_{21} + \hat{a}^\dagger\hat{\sigma}_{12}) \\
&+ g(\alpha\hat{\sigma}_{21} + \alpha^*\hat{\sigma}_{12}) + i\kappa/2(\alpha^*\hat{a} - \alpha\hat{a}) \\
&= \Delta_1\hat{\sigma}_{11} + (\Delta_1+\Delta_2)\hat{\sigma}_{22} + g(\hat{a}\hat{\sigma}_{21} + \hat{a}^\dagger\hat{\sigma}_{12}) + g(\alpha\hat{\sigma}_{21} + \alpha^*\hat{\sigma}_{12})
\end{aligned} \tag{A.43}$$

Now we can see that after the displacement, the master equation remains its form with only the effective system Hamiltonian changed. Figure A.1 shows the simulation results with

original and displaced master equations. By comparing the time evolution of the cavity field photon number and the transmon middle state population, we can see that perfect agreement between the results by original and displaced master equations. I should mentioned that in the simulation with the original master equation, the initial state of the cavity field is the steady state $\langle \hat{a}(t) \rangle = \alpha = -i2E/\kappa$, not the vacuum.

By the displacement, the system space dimension is reduced from $|\alpha|^2$ to a space dimension for small quantum fluctuations around the steady state. This results in much less requirements of time and computation resources.